COMPUTATIONAL MODELLING OF CONCRETE
TIME-DEPENDENT MECHANICS AND ITS APPLICATION
TO LARGE-SCALE STRUCTURE ANALYSIS

by

Teng Tong

BS in Civil Engineering, Southeast University, China, 2009

MS in Civil Engineering, Southeast University, China, 2012

Submitted to the Graduate Faculty of

the Swanson School of Engineering in partial fulfillment

of the requirements for the degree of

Doctor of Philosophy

University of Pittsburgh

2016

UNIVERSITY OF PITTSBURGH

SWANSON SCHOOL OF ENGIEERING

This dissertation was presented

by

Teng Tong

It was defended on

November 17, 2016

and approved by

Kent Harries, PhD, Associate Professor, Department of Civil and Environmental Engineering

Jeen-Shang Lin, ScD, Associate Professor, Department of Civil and Environmental

Engineering

Susheng Tan, PhD, Research Assistant Professor, Department of Electrical and Computer

Engineering

Dissertation Director: Qiang Yu, PhD, Assistant Professor, Department of Civil and

Environmental Engineering

COMPUTATIONAL MODELLING OF CONCRETE TIME-DEPENDENT

MECHANICS AND ITS APPLICATION TO LARGE-SCALE STRUCTURE

ANALYSIS

Teng Tong, PhD

University of Pittsburgh, 2016

The goal of the proposed work is to systematically study the time-dependent mechanics of concrete with a focus on concrete creep and its effect on prestressed concrete bridges, which are creep-sensitive. With increasing demands for sustainable construction, a longer lifespan, i.e., over 100 years, is now generally expected for critical bridges in structural design. To ensure the safety and serviceability of prestressed concrete bridges throughout this prolonged lifespan, there is a call for deeper understanding of the concrete time-dependent mechanics and its effects on the structural performance of prestressed concrete bridges.

The primary aim of this study is to build a numerical framework to estimate the time-dependent performance of prestressed concrete bridges based on the development of concrete creep and its coupling with other physical and chemical processes. The established framework will be used to capture the correlation between the long-term asymptotes of deformation curves, early age measurements, and distinctive concrete creep models. Based on the identified correlation and in-situ measurements, a suitable creep model can be identified and calibrated for the bridge under investigation. Then the framework is extended to take into account the effect of scatter in concrete creep on the deformation asymptote. Statistical analyses based on the Latin hypercube sampling scheme are employed to investigate the effectiveness and robustness of the established correlation. For bridges carrying heavy traffic flows, the intertwined effects of

concrete static creep, cyclic creep, softening and cracking are recommended to be incorporated to enhance the predictive capacity of the proposed framework. To meet this need, a unified concrete constitutive model is formulated and then is integrated in the 3D rate-type formulation for full-scale creep structural analysis.

Finally, to remedy the inadequacy resulting from the phenomenological formulas in concrete creep modeling, a multi-scale methodology residing at the meso-scale of concrete is developed. A representative volume element (RVE) of concrete is numerically generated for the multi-scale analysis and the macros-scale time-dependent behavior of concrete is approximated by a proper computational homogenization scheme.

TABLE OF CONTENTS

LIST OF TABLES

LIST OF FIGURES

PREFACE

This thesis contains two published journal papers:

Chaper 2 presents the first journal paper: "Wender R, Tong T, Strauss A, and Yu Q. A case study on correlations of axial shortening and deflection with concrete creep asymptotes in segmentally-erected prestressed box girders. *Structure and Infrastructure Engineering*, 11(12): 1672-1687, 2015". In this work, two columns in Table 2.2, "*distribution type*" and "*standard deviation*", were proposed by co-authors Wender and Strauss. In addition, co-authors Wender and Strauss also provided the material parameters for the 45 simulations in Chapter 2.7, which were generated by Latin hypercube sampling scheme.

Chapter 3 presents the second journal paper: "Tong T, Liu Z, Zhang J, and Yu, Q. Long-term performance of prestressed concrete bridges under the intertwined effects of concrete damage, static creep and traffic-induced cyclic creep. *Engineering Structures*, 127: 510-524, 2016". In this work, the drawings and investigation report [73] of the Humen Bridge were provided by co-author Liu. In addition, the stress variations induced by different vehicles were analyzed by co-author Zhang.

The author greatly acknowledges the contributions from these co-authors.

ACKNOWLEDGEMENTS

First and foremost I wish to thank my advisor Dr. Qiang Yu. It is an honor to be one of his Ph.D. students. He has taught me, both consciously and unconsciously, since the days I began to work here. I appreciate all his contributions of time, ideas, and funding to make my Ph.D. experience productive and stimulating. Without his unending faith in my potential and his wonderful and tireless guidance, this work could not be accomplished.

I would like to thank all the committee members of my dissertation: Dr. Kent Harries, Dr. Jeen-Shang Lin and Dr. Susheng Tan. Your academic suggestions, assistances and guidance are critical for me to complete my dissertation.

The group members in Dr. Qiang Yu's team have contributed immensely to my personal and professional progress at the University of Pittsburgh. They have been a source of friendship as well as good advice and collaboration. I would like to acknowledge the group member Mr. Chunlin Pan and Ms. Weijin Wang. We have collaborated on several projects, and I deeply appreciate their enthusiasm, intensity and willingness to help.

Lastly, I would like to thank my family for all their love and encouragement. For my parents who raised me with love and supported me in all my pursuits, I would like to say that I love you.

1.0   INTRODUCTION

1.1   MOTIVATION AND BACKGROUND

Elongating the service lifetime of an infrastructure system can significantly reduce its economic and environmental footprint, and thus is an essential aspect of the progress towards a sustainable built environment. For critical structures like large-span bridges, a longer lifespan, i.e., over 100 to 120 years, is now generally expected in design. However, for segmentally-erected prestressed concrete bridges, a serious challenge to this goal is the currently low quality in long-term performance prediction, which is a result of the complex time-dependent interactions between concrete creep, shrinkage, steel relaxation, and deterioration processes, coupled with other physical [1] and mechanical [2] influences.

A recent survey [3] on segmentally-erected prestressed concrete box girders shows that among 56 prestressed box girders from around the world, over 60% of them displayed excessive deflections about 20 years after construction, although their short-term deflections were benign. Until now, there is still no unified definition for the excessive deflection. In this thesis, the excessive deflection means the magnitude of the vertical deflection apparently exceeds the expected value, which can be estimated based on the current specifications. Unexpectedly excessive deflection has a profound impact on the bridge safety and serviceability. Recently, there are numerous studies about the excessive vertical deflection of the Koror-Babeldaob (KB)

1

Bridge in Palau [4]-[7]. This was a segmentally-erected prestressed box girder with a main span of 241m. The bridge was built in 1977. After 18 years' service, the vertical deflection at the middle span reached 1.61 m, which was measured from the design camber. Finally, this bridge collapsed after a risky retrofit aimed at partially recovering its serviceability; see Figure 1.1. The immediate cause of the collapse was improper retrofit design and procedure [8] although the excessive deflection did precipitate the need to retrofit.

Figure 1.1. Collapse of K-B bridge after 18 years' service.

A further investigation [9] on these bridges leads to the conclusion that the significant underestimation of the long-term asymptote of concrete creep and its scatter in design models is one of the primary causes of the unrealistic prediction of the long-term deflections for large-span prestressed concrete bridges. Considering the excessive vertical deflection can severely affect the safety and serviceability of bridges, extensive efforts have been invested to improve the accuracy in predicting the multi-decade deflections of large-span prestressed concrete bridges [10]. More realistic concrete creep models and advanced numerical formulations have been developed

recently [11]-[15]. Built upon long-term creep tests, theoretical formulations and statistical analyses [16][17], design formulas capable of approximating the long-term asymptote of concrete static creep have been proposed and used for predicting the long-term deflections of bridges. For example, by utilizing the models B3/B4 [14][18] and the *fib* (2010) [19] models, the time-dependent deflections recorded in several large-span prestressed concrete bridges have been realistically approximated in recent full-scale numerical analyses, respectively. A common characteristic of these improved creep models is that under sustained stress the static creep of concrete does not terminate with time. Instead, the growth of static creep follows a nonzero asymptotical slope in log-time scale.

The oversimplified modelling and primitive formulation in creep analysis are identified as other sources of inaccuracy [13]. In addition to improving the concrete creep models, progresses have also been achieved in the numerical formulation for full-scale 3D creep structural analysis. Rate-type formulation, residing on rheological models and utilizing 3D solid elements, has recently been developed and successfully implemented in numerical analyses of several large-span prestressed concrete bridges [3][15][20]. Compared to the integral-type formulation using one- or two-dimensional beam elements, the 3D rate-type formulation significantly improves computational efficiency and model fidelity. More importantly, it enables coupling between the creep analysis and other memory-dependent or -independent processes. Unfortunately, the coupling between the creep analysis and the softening, cracking, and cyclic creep of concrete is weak in the recent studies [3][15][20].

Currently, concrete creep models are predominantly calibrated based on the macro-scale tests, like B3/B4 [14][18] and *fib* (2010) model [19]. In these creep models, concrete is treated as a homogenous material and how the different phases affect the macro-scale concrete creep is not

considered. Nevertheless, concrete is a heterogeneous material with multiple phases. The mechanisms of these different phases at meso-, micro-, or even nano-scales intrinsically determine the macro-scale mechanical and transport behaviors of concrete. At the meso-scale, concrete can be decomposed as mortar matrix, coarse aggregate, interface transition zone (ITZ), and air voids. Furthermore, the mortar matrix can be decomposed as fine aggregate (sand), anhydrous phase, CH, CSH and porous phase at the micro-scale [21]. Recently, Pellenq proposed the atomistic model of CSH [22] and propelled the relevant research of cementitious materials at the nano-scale. Multi-scale experiments and simulations of cementitious materials can offer more accurate insights to the mechanical, time-dependent, and transport behaviors of cementitious materials [23]-[25]. Although numerical studies of concrete properties at different scales can provide more accurate results, it is prohibitively expensive to investigate concrete at micro-scale or nano-scale, due to limited computational capacity. Fortunately, meso-scale investigation is accurate enough to obtain a fundamental understanding of mechanical and time-dependent mechanisms, which can be utilized in the macro-scale analysis [26].

1.2   DIFFERENT CONCRETE CREEP MODELS

To study creep-sensitive structures, like segmentally-erected prestressed concrete bridges presented in this thesis, it is essential to implement an efficient and realistic creep model. Concrete creep, characterized by gradual strain growth with time under a unit sustained stress applied at age t_0 (in days), is generally calculated based on a given compliance function $J(t, t_0)$, where t (in days) is the current time.

In this section, the details of various concrete creep models are discussed, including ACI (2008) [27], CEB-FIP (1990) [28], *fib* (2010) [19], and B3 [14] models. The B4 [18] model is similar to B3 model and is not presented here.

1.2.1 ACI (2008) model

In the ACI model, concrete creep is described by the so-called creep coefficient $\varphi(t, t_0)$, which is the ratio of creep strain to elastic strain:

$$J(t, t_0) = [1 + \varphi(t, t_0)]/E_{cmt0} \tag{1.1}$$

where E_{cmt0} is the modulus of the elasticity (in MPa) at t_0, which is given as:

$$E_{cmt0} = 0.043 \chi_c^{1.5} \sqrt{f_{cmt0}} \tag{1.2}$$

where χ_c is the unit weight of concrete in kg/m^3, and f_{cmt0} is the mean concrete strength (in MPa) at t_0. The creep coefficient $\varphi(t, t_0)$ has two components that determine the asymptotic value and the time development of creep and is given as:

$$\varphi(t, t_0) = \frac{(t - t_0)^\nu}{d + (t - t_0)^\nu} \varphi_u \tag{1.3}$$

where $(t - t_0)$ is the duration of loading; d and ν are empirical constants; and φ_u is the ultimate creep coefficient. For typical conditions, in the absence of specific creep data for local aggregates and conditions, the average value for the ultimate creep coefficient is $\varphi_u = 2.35$, and average values of 10 and 0.6 are recommended for d and ν, respectively.

For other conditions, the value of φ_u needs to be modified by correction factors, as follows [27]:

$$\varphi_u = 2.35\gamma_c = 2.35\gamma_{c,to}\gamma_{c,RH}\gamma_{c,vs}\gamma_{c,s}\gamma_{c,\psi}\gamma_{sh,\alpha} \tag{1.4}$$

where γ_c represents the cumulative product of the applicable correction factors. For ages at application of load greater than 7 days for moist-curved concrete or greater than 1 to 3 days for steam-cured concrete, the age of loading factor for creep $\gamma_{c,to}$ is estimated from:

$$\gamma_{c,to} = 1.25t_0^{-0.118} \text{ for moisture curing}$$

$$\gamma_{c,to} = 1.13t_0^{-0.094} \text{ for steam curing} \tag{1.5}$$

The factor $\gamma_{c,RH}$ is related to the ambient relative humidity h as:

$$\gamma_{c,RH} = 1.27 - 0.67h \text{ for } h \geq 0.40 \tag{1.6}$$

The coefficient $\gamma_{c,vs}$ accounts for the size of the member in terms of the volume (V in mm^3)-surface (S in mm^2) ratio, and is expressed as:

$$\gamma_{c,vs} = \frac{2}{3}(1 + 1.13e^{\{-0.0213(V/S)\}}) \tag{1.7}$$

The slump factor $\gamma_{c,s}$, where s is the slump (in mm) of fresh concrete, is

$$\gamma_{c,s} = 0.82 + 0.00264s \tag{1.8}$$

The fine aggregate factor $\gamma_{c,\psi}$, where ψ (expressed as percentage) is the ratio of fine aggregate to total aggregate by weight, is

$$\gamma_{c,\psi} = 0.88 + 0.024\psi \tag{1.9}$$

The air content factor $\gamma_{sh,\alpha}$, where α is the air content in percentage, is

$$\gamma_{sh,\alpha} = 0.95 + 0.008\alpha \geq 1 \tag{1.10}$$

1.2.2 CEB-FIP (1990) model

The compliance function $J(t, t_0)$ that represents the total stress-dependent strain is given as:

$$J(t,t_0) = \frac{1}{E_{cm28}}[\eta(t_0) + \varphi_{28}(t,t_0)] = \frac{1}{E_{cmt0}} + \frac{\varphi_{28}(t,t_0)}{E_{cm28}} \qquad (1.11)$$

where $\eta(t_0) = E_{cm28} / E_{cmt0}$. E_{cm28} is the mean modulus (in MPa) of elasticity of concrete at 28 days. Within the range of service stress, the 28-day creep coefficient $\varphi_{28}(t,t_0)$ is calculated as:

$$\varphi_{28}(t,t_0) = \varphi_0 \beta_c(t - t_0) \qquad (1.12)$$

in which φ_0 is the notional creep coefficient and $\beta_c(t - t_0)$ is the coefficient that describes the development of creep with time after loading. The notional creep coefficient φ_0 can be determined as:

$$\varphi_0 = \varphi_{RH}(h)\beta(f_{cm28})\beta(t_0) \qquad (1.13)$$

with

$$\varphi_{RH}(h) = [1 + \frac{1 - h/h_0}{\sqrt[3]{0.1[(V/S)/(V/S)_0]}}\alpha_1]\alpha_2 \qquad \alpha_1 = (\frac{3.5f_{cm0}}{f_{cm28}})^{0.7} \qquad \alpha_2 = (\frac{3.5f_{cm0}}{f_{cm28}})^{0.2} \qquad (1.14)$$

$$\beta(f_{cm28}) = \frac{5.3}{\sqrt{f_{cm28}/f_{cm0}}} \qquad (1.15)$$

$$\beta(t_0) = \frac{1}{0.1 + (t_0/t_1)^{0.2}} \qquad (1.16)$$

$$\varphi_0 = \varphi_{RH}(h)\beta(f_{cm28})\beta(t_0) \qquad (1.17)$$

where f_{cm28} is the mean concrete strength (in MPa) at the age of 28 days; $f_{cm0} = 10 MPa$; $h_0 = 1$; $(V/S)_0 = 50mm$; and $t_1 = 1$ day. The function $\beta_c(t - t_0)$ describes the development of creep with time after loading and is expressed as:

7

$$\beta_c(t - t_0) = [\frac{(t - t_0)/t_1}{\beta_H + (t - t_0)/t_1}]^{0.3} \tag{1.18}$$

with

$$\beta_H = 150[1 + (1.2h/h_0)^{18}](V/S)/(V/S)_0 + 250\alpha_3 < 1500\alpha_3 \quad \alpha_3 = (\frac{3.5f_{cm0}}{f_{cm28}})^{0.5} \tag{1.19}$$

1.2.3 *Fib* (2010) model

In the *fib* (2010) model, the compliance function $J(t, t_0)$ is expressed as:

$$J(t, t_0) = \frac{1}{E_{cmt0}} + \frac{\varphi(t, t_0)}{E_{cm28}} \tag{1.20}$$

The creep coefficient $\varphi(t, t_0)$ is calculated as the basic creep coefficient $\varphi_{bc}(t, t_0)$ and the

drying creep coefficient $\varphi_{dc}(t, t_0)$:

$$\varphi(t, t_0) = \varphi_{bc}(t, t_0) + \varphi_{dc}(t, t_0) \tag{1.21}$$

The basic creep coefficient $\varphi_{bc}(t, t_0)$ may be estimated from:

$$\varphi_{bc}(t, t_0) = \beta_{bc}(f_{cm28}) \cdot \beta_{bc}(t, t_0) \tag{1.22}$$

with

$$\beta_{bc}(f_{cm28}) = \frac{1.8}{(f_{cm28})^{0.7}} \tag{1.23}$$

$$\beta_{bc}(t, t_0) = In[(\frac{30}{t_0} + 0.035)^2 \cdot (t - t_0) + 1] \tag{1.24}$$

The drying creep coefficient $\varphi_{dc}(t, t_0)$ may be estimated as:

$$\varphi_{dc}(t, t_0) = \beta_{dc}(f_{cm28}) \cdot \beta(h) \cdot \beta_{dc}(t_0) \cdot \beta_{dc}(t, t_0) \tag{1.25}$$

with

8

$$\beta_{dc}(f_{cm28}) = \frac{412}{(f_{cm28})^{1.4}} \tag{1.26}$$

$$\beta(RH) = \frac{1 - \dfrac{h}{100}}{\sqrt[3]{0.1 \cdot \dfrac{(2A_c/u)}{100}}} \tag{1.27}$$

$$\beta_{dc}(t_0) = \frac{1}{0.1 + t_0^{0.2}} \tag{1.28}$$

where $(2A_c/u)$ is the notional size of member (in mm), A_c is the cross-section (in mm^2) and u is

the perimeter of the member (in mm) in contact with the atmosphere.

The development of drying creep with time is described as:

$$\beta_{dc}(t,t_0) = [\frac{(t-t_0)}{\beta_h + (t-t_0)}]^{\gamma(t_0)} \tag{1.29}$$

with

$$\gamma(t_0) = \frac{1}{2.3 + \dfrac{3.5}{\sqrt{t_0}}} \tag{1.30}$$

$$\beta_h = 1.5(2A_c/u) + 250(\frac{35}{f_{cm28}})^{0.5} \le 1500(\frac{35}{f_{cm28}})^{0.5} \tag{1.31}$$

1.2.4 B3 model

The concrete creep in the B3 model considers instantaneous deformation, basic and drying creep

as:

$$J(t,t_0) = q_1 + C_0(t,t_0) + C_d(t,t_0,t_c) \tag{1.32}$$

where q_1 is the instantaneous strain due to unit stress; $C_0(t,t_0)$ is the compliance function for the basic creep; $C_d(t,t_0,t_c)$ is the additional compliance function for the drying creep; and t_c is the age when drying begins for concrete. The instantaneous strain due to unit stress is expressed as:

$$q_1 = 0.6 / E_{cm28} \tag{1.33}$$

The basic creep $C_0(t,t_0)$ is composed of three terms: an aging viscoelastic term, a nonaging viscoelastic term and an aging flow term:

$$C_0(t,t_0) = q_2 Q(t,t_0) + q_3 \cdot \text{In}[1+(t-t_0)^{0.1}] + q_4 \text{In}(t/t_0) \tag{1.34}$$

where $q_2 Q(t,t_0)$ is the aging viscoelastic compliance term. The cement content c and the concrete mean compressive strength at 28 days f_{cm28} (in MPa) are required to calculate the parameter q_2 as:

$$q_2 = 185.4 \times 10^{-6} c^{0.5} f_{cm28}^{-0.9} \tag{1.35}$$

$Q(t,t_0)$ is an approximate binomial integral and is expressed as:

$$Q(t,t_0) = Q_f(t_0)[1+(\frac{Q_f(t_0)}{Z(t,t_0)})^{r(t_0)}]^{-1/r(t_0)}$$

$$Q_f(t_0) = [0.086(t_0)^{2/9} + 1.21(t_0)^{4/9}]^{-1} \tag{1.36}$$

$$Z(t,t_0) = (t_0)^{-0.5} \cdot \text{In}[1+(t-t_0)^{0.1}]$$

$$r(t_0) = 1.7(t_0)^{0.12} + 8$$

q_3 is the nonaging viscoelastic compliance parameter and q_4 is the aging flow compliance parameter. These parameters are functions of the concrete mean strength at 28 days f_{cm28} (in MPa), the concrete content c (in kg/m^3), the water to cement ratio w/c and aggregate to cement ratio a/c:

10

$$q_3 = 0.29(w/c)^4 q_2 \tag{1.37}$$

$$q_4 = 20.3 \times 10^{-6} (a/c)^{-0.7} \tag{1.38}$$

The compliance function for drying creep $C_d(t,t_0,t_c)$ is defined as Eq. (1.39). This equation accounts for drying before loading:

$$C_d(t,t_0,t_c) = q_5 [\exp\{-8H(t)\} - \exp\{-8H(t_0)\}]^{1/2} \tag{1.39}$$

$H(t)$ and $H(t_0)$ are spatial averages of pore relative humidity, which are expressed as:

$$H(t) = 1 - (1-h)\tanh[(\frac{t-t_c}{\tau_{sh}})^{1/2}] \tag{1.40}$$

$$H(t_0) = 1 - (1-h)\tanh[(\frac{t_0-t_c}{\tau_{sh}})^{1/2}]$$

where τ_{sh} is the shrinkage half-time. q_5 is the drying creep compliance parameter and is a function of the concrete mean strength at 28 days f_{cm28} (in MPa) and the ultimate shrinkage strain $\varepsilon_{sh\infty}$, and is given as:

$$q_5 = 0.757 f_{cm28}^{-1} |\varepsilon_{sh\infty} \times 10^6|^{-0.6} \tag{1.41}$$

1.3   RATE-TYPE FORMULATION FOR CREEP ANALYSIS

For a stress level within the service stress range, concrete creep is assumed to follow the constitutive law of ageing linear viscoelasticity [6][7][29]. The viscoelasticity means that under deformation, the material will exhibit both viscous and elastic characteristics. Thus, the principle of superposition can be applied to estimate the concrete creep under a general stress history $\sigma(t)$.

This principle means that the total creep strain due to multiple individual stress histories is the sum of multiple corresponding creep strain responses. Thus, one may write the creep law in the in the form of Volterra integral equation:

$$\varepsilon = \int_{t_0}^{t} J(t,t_0)d\sigma \qquad (1.42)$$

Unfortunately, the kernel $J(t, t_0)$ in the Volterra integral equation is not of a convolution type due to the ageing of concrete creep. Therefore, the direct application of the principle of superposition leads to a primitive integral-type formulation for creep analysis, in which all the history data must be stored and then used for the next step. Only for small-scale 1D or 2D analysis under simple loading, is this approach applicable because the computational cost is affordable. However, for the structural analyses of the long-term behaviors of large creep-sensitive structures such as prestressed box girders and large-span shells, the computational cost will be extremely high if all the history variables must be stored at each time step.

Furthermore, for large-scale structures, concrete creep will strongly interact with other physical and mechanical phenomena, e.g., concrete cracking and damage, steel relaxation, and environment variations, to name a few. These influencing phenomena are usually memory-independent, and thus not compatible with the integral-type formulation. Therefore, for large-scale creep structural analysis, it is necessary to convert the integral-type formulation to a rate-type algorithm for creep analysis.

Generally, a realistic stress-strain relation based on ageing linear viscoelasticity can be approximated at any desired accuracy by a rheological model, which is usually visualized with a system of Kelvin units, Maxwell units or their hybrids. For creep, a Kelvin chain is more convenient because a Maxwell chain requires converting the compliance function $J(t, t_0)$ to a relaxation function $R(t, t_0)$, which adds numerical cost. The Kelvin chain model consists of a

series of Kelvin units $\mu = 1, 2, 3, \cdots, N$; see Figure 1.2. Each Kelvin chain unit contains a spring coupled in parallel with a dashpot. Using a Kelvin chain model consisting of N Kelvin units of distinctive relaxation time τ_μ, the creep analysis can be converted to a quasi-elastic incremental stress-strain relation, which can be easily solved in general FEM software like ABQAUS.
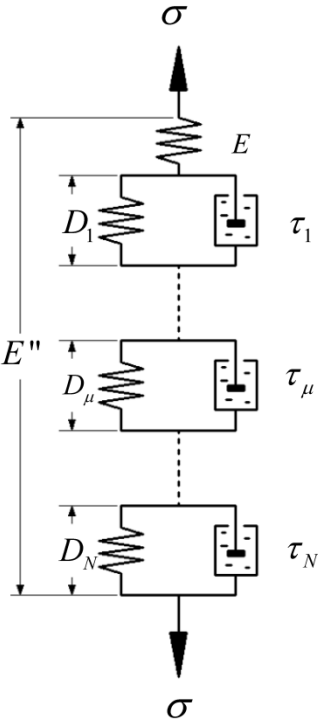
Figure 1.2. A Kelvin chain consisting of N Kelvin units.

For a rate-type formulation, the 3D quasi-elastic stress-strain incremental relation at any time step can be written as [13][29]:

$$\Delta\sigma = E'(\Delta\varepsilon - \Delta\varepsilon'') \tag{1.43}$$

where $\Delta\varepsilon''$ is the increment of inelastic strain induced by concrete creep. If concrete is damaged at this time step, the damage strain can be incorporated into the inelastic strain. E' is the effective incremental modulus that can be expressed as:

$$\frac{1}{E'} = \frac{1}{E_0} + \sum_{\mu=1}^{N} D_\mu^{-1} = \frac{1}{E_0} + \sum_{\mu=1}^{N} A_\mu(1-\lambda_\mu) \tag{1.44}$$

where E_0 is the short-term modulus; D_μ is the modulus of the μ th Kelvin unit; λ_μ is a variable related to the relaxation time τ_μ and the time increment Δt; and A_μ is the discrete spectrum of a given compliance. In the previous practice of creep analysis, A_μ is determined by numerical fitting, an approach being found to give non-unique results and to be oversensitive to the complexity of the compliance function. To overcome this problem, the continuous spectrum approach [13][30] is used in this study.

If relaxation times τ_μ have an infinitely close spacing, they will form a continuous retardation spectrum, which can be uniquely identified by utilizing Laplace transformation inversion supplemented by Widder's approximate inversion formula [31]. The analytical solution for a given compliance function gives:

$$L(\tau_u) = \frac{\lim\limits_{k\to\infty}(k\tau_u)^k C^{(k)}(k\tau_u)}{(k-1)!} \tag{1.45}$$

where $C^{(k)}$ is the k-th order derivative on time t of the creep function $C(t, t_0) = J(t, t_0) - 1/E_0$. For creep formulas used in the current practice, it suffices to use $k = 3$. Then a discretization of the continuous spectrum gives the discrete spectrum for each Kelvin unit:

$$A(\tau_u) = L(\tau_u)\text{In}10 \tag{1.46}$$

which is needed for calculating E' in Eq. (1.44) at each time step. If the time increment Δt is sufficiently short compared to the age of concrete, the ageing of the material can be neglected

within the individual time step. This means that, although $J(t, t_0)$ is different at each time step due to ageing, within a given time step, a constant compliance $J(t, t_0)$ can be used to calculate the discrete spectrum A_μ, where t_0 is the age of concrete at the middle of the current time step. By doing this, the effects of environment variations and other phenomena on the compliance function can be taken into account.

The general algorithms for the numerical solutions of the first order ordinary differential equations, including central or backward difference methods or the Runge-Kutta method, will have numerical instability problems, as these numerical algorithms are stable only if $\Delta t << \tau_1$. In order to achieve numerical stability, the exponential algorithm, which is an unconditionally stable algorithm, is utilized here. This algorithm gives:

$$\lambda_u = \tau_u (1 - e^{-\Delta t / \tau_u}) / \Delta t \tag{1.47}$$

Therefore, the increment of inelastic strain induced by concrete creep $\Delta \varepsilon''$ can be obtained for each integration point of each finite element:

$$\Delta \varepsilon'' = \sum_{u=1}^{N} (1 - e^{-\Delta t / \tau_u}) \gamma_u^{(n-1)} \tag{1.48}$$

The increment of internal variable γ_u of the μth Kelvin unit is then updated at each integration point as follows:

$$\gamma_u^{(n)} = \lambda_u \Delta \sigma D_u^{-1} + e^{-\Delta t / \tau_u} \gamma_u^{(n-1)} \tag{1.49}$$

where the history of the internal variables γ_u, stress σ and other variables for the previous time steps does not need to be stored, which will greatly save computational cost.

In addition to creep in tension and compression, creep in shear can be taken into account in the present formulation when the rate-type formulation is applied in 3D structures. This is critical for capturing the shear lag, which is important for the long-term deformation of

15

prestressed concrete girders having thin walls that cannot be captured in simplified 1D or 2D analyses [13]. Therefore, the improved rate-type formulation employed in the present study offers great advantages in approximating concrete ageing, concrete creep coupled with damage, shear lag and variations in the environmental conditions. The incremental elastic stress-strain relation in Eq.(1.43) for each time step can further be modified according to other physical and mechanical phenomena.

1.4   RESEARCH TOPICS IN THIS DISSERTATION

Utilizing the various concrete models and the improved rate-type formulation for creep analysis discussed above, this research starts with modelling asymptotic behaviors, including the vertical deflection and axial shortening, of the Colle Isarco Viaduct Bridge under the various creep models. The deformation asymptotes of this post-tensioned box girder bridge with a total length of 1,000 m are captured and discussed in Chapter 2. When predicting the long-term vertical deflection for some prestressed concrete bridges carrying heavy busy traffic flows, it is necessary to further consider the coupled effects of traffic-induced cyclic creep and concrete tensile cracking. The unified concrete model is proposed in Chapter 3 to explicitly consider the concrete damage, static creep and traffic-induced cyclic creep. In Chapter 4, the time-dependent behavior of concrete is investigated at the meso-scale. The effects of shape and spatial distribution of coarse aggregates and voids on the mechanical and time-dependent behaviors of concrete are investigated, based on the meso-scale structure of concrete. Two approaches, computational multiscale analysis and multiscale material model, are discussed to map the response of meso-scale structure to the macro-scale structure.

2.0 LONG-TERM DEFORMATION ASYMPTOTES OF POST-TENSIONED PRESTRESSED CONCRETE BRIDGES AND THEIR CORRELATIONS WITH CONCRETE CREEP

2.1 MOTIVATION AND BACKGROUND

A recent study [3] shows that among 56 prestressed concrete bridges from around the world, over 60% of them displayed excessive deflections about 20 years after construction. These excessive deflections indicate the poor predictive capabilities of current creep models resulted from inadequacies in their compliance functions, a primary source of which is the scarcity of systematic long-term creep tests data [32][33]. Available creep and shrinkage databases compiled from laboratories around the world for model calibration are dominated by short-term tests [11][34][35], which provide little information about the long-term trends of concrete creep. This obstructs the formulation, calibration, and validation of theoretically based prediction models for concrete creep. Furthermore, without sufficient experimental information, the parameters governing the long-term asymptote of concrete creep and their variations cannot be identified, even after a theoretically solid formulation is qualitatively established for the compliance function. To remedy this problem, multi-decade in-situ measurements must be used to supplement the current databases of laboratory tests [12]. This however requires information

regarding the correlation of concrete creep with the observed structural responses such as mid-span deflection or axial shortening of prestressed bridge elements.

This chapter will focus on how to identify and establish a correlation between the long-term asymptotes of deformation curves, early age measurements, and the distinctive compliance functions of different creep models. Different concrete creep models, including ACI (2008) [27], CEB-FIP (1990) [28], *fib* (2010) [19], B3 [14] and B4 [18] models, are utilized to capture deformation asymptotes of a selected prestressed concrete bridge. Based on the identified correlation and in-situ measurements, a suitable creep model can be identified and calibrated for the bridge under investigation. The governing parameters in the compliance function can be approximated according to the concrete specifications and the established correlation. Another objective of this chapter is to investigate the effect of scatter in concrete creep on the deformation asymptote. Statistical analyses based on the Latin hypercube sampling scheme [36] are employed to investigate the effectiveness and robustness of the established correlation.

In this chapter, the Colle Isarco Viaduct Bridge, located in Northern Italy having a total length of 1,000 m [37], is simulated to serve as a case study. All analyses are performed using a 3D model that was created based on the available design drawings of the Bridge. Different prestress levels will be applied to the tendons to explore their effects on the pursued correlation between long-term deformation and concrete creep. In order to isolate the fundamental interactions between the deformation evolution and time-dependent mechanics of concrete and steel, the other coupled phenomena like fatigue, damage and corrosion will not be considered, although they can be incorporated in a unified framework, which will be addressed in Chapter 3.

2.2 BRIDGE MODELING

The bridge modelled in this study is one main cantilever portion of the Colle Isarco Viaduct, located in Northern Italy (see the bridge in the red circle in Figure 2.1(a)). The bridge is a fully post-tensioned box girder bridge with a total length of 1,000 m as described in a recent investigation [37]. The main structural elements are two identical cast-in-place balanced cantilever girders, each with a total length of 167.5 m. The girders are subdivided into a main span of 91.0 m, a long cantilever of 59.0 m, and a short cantilever of 17.5 m. With a width of 11.0 m, the top slab of a symmetric cross-section is 5.0 m wider than the bottom slab. The height of the girder decreases from 10.8 m at Pier 1 to 4.5 m at Pier 2 and further to 2.85 m at the tip of the cantilevers. The cross-sections of the box girders at Piers 1 and 2 are shown in Figure 2.1(b).

(a)

59 m   Pier 1   91 m   Pier 2   17.5 m

Cross-section at Pier 1   Cross-section at Pier 2
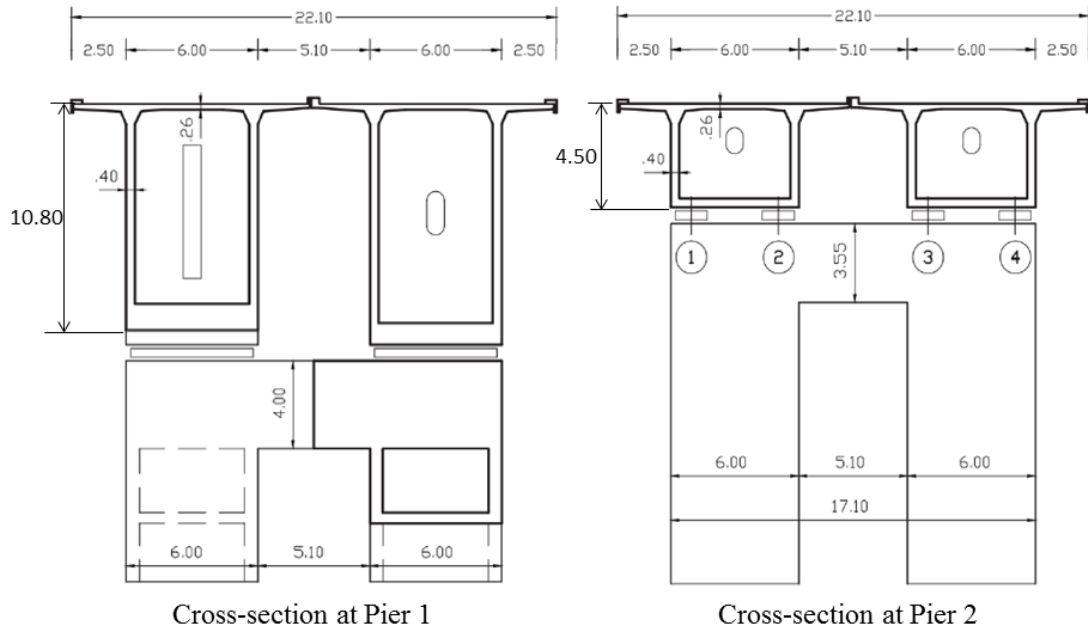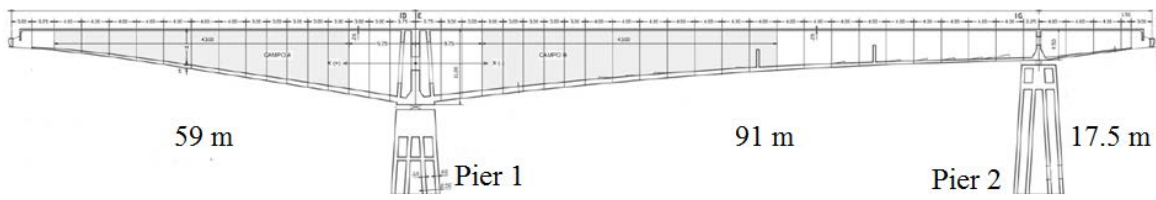
(b)
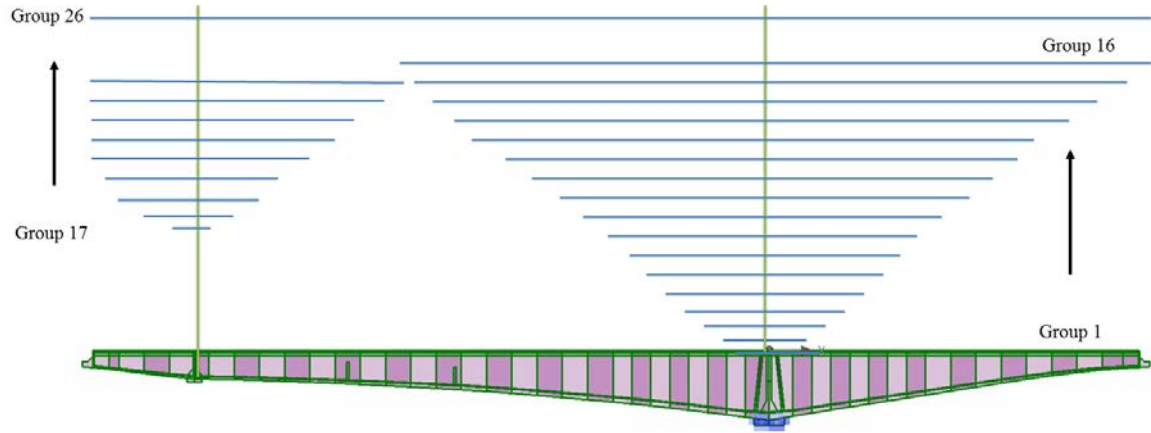
Figure 2.1. Colle Isarco Viaduct Bridge [37]: (a) Real Bridge; (b) cross-sections of box girder at Piers 1 and 2 (Unit: m); and (c) the tendon layout.

To realistically approximate the stress and strain evolutions in this bridge during its service lifetime, a 3D FEM program, capable of incorporating the requisite material constitutive laws and mimicking the complex loading history, is needed. Due to its advantages in implementing user-defined materials and modelling the segmental construction sequence, the software ABAQUS is selected. In Figure 2.2(a), the bridge model built in ABAQUS based on the information given by [37] is shown. Because of the symmetry, only half of the cross-section needs to be modelled, see Figure 2.2(a). The layout of the prestressing tendons is shown in Figure 2.2(b).
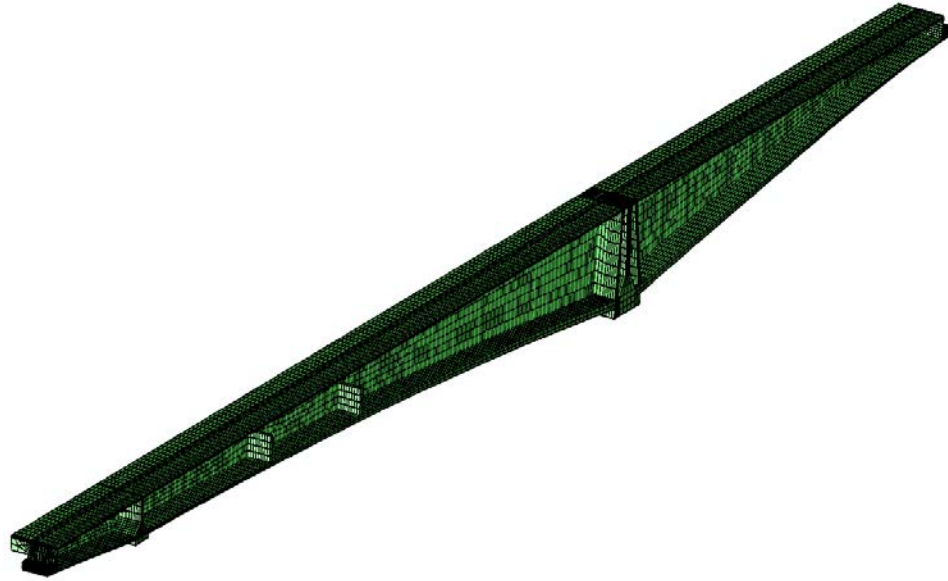
(a)
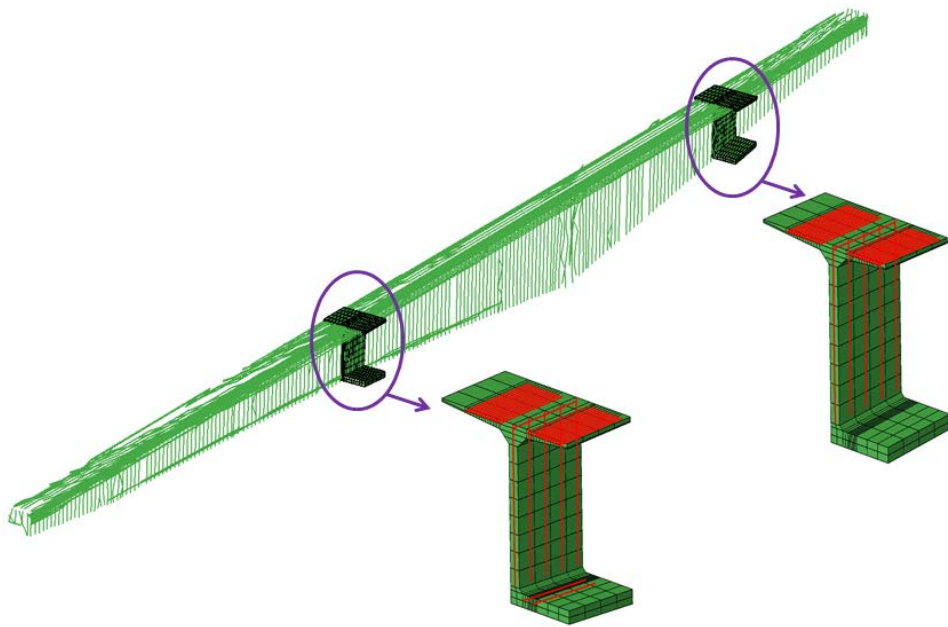
(b)

Figure 2.2. Modelling of: (a) Colle Isarco Viaduct Bridge, and (b) its prestressing tendons.

The webs, and top and bottom slabs of the box girder are modelled by two layers of elements through their thickness. Hence, the prestressing tendons can be placed at the middle of these slabs, see Figure 2.3. The red circles in Figure 2.3 show the possible locations for the longitudinal prestressing tendons at the top and bottom slabs. Concrete is modelled by 3D hexahedral isoparametric elements; while for the tendons 3D truss elements are utilized. The non prestressed reinforcing steel is not explicitly considered in the FEM model because (1) it is computationally expensive to model every bar in the FEM simulations, and (2) the overall behavior of reinforced concrete is still viscoelastic due to the low mild steel ratio (1-2%) in this bridge. However, to account for the effect of mild steel bars, the Young's modulus of concrete is adjusted according to the ratio of mild steel based on the smeared method [5][13]. In this half section bridge model, 497 prestressing tendons (Grade 1860 low-relaxation) are used to prestress the 44 segments sequentially. Among the tendons, there are 149 prestressing tendons over the main pier, which are categorized into 26 groups based on the prestressing sequence, see Figure 2.1(c) and Table 2.1. Since the tendons are mostly straight (Figure 2.2(b)), the curvature friction is negligible and only wobble friction needs to be considered. For each group of tendons, the prestress is applied 7 days after their anchoring segment is cast.
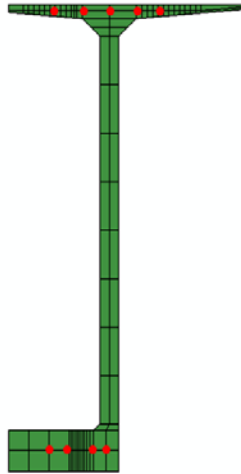
Figure 2.3. Mesh of cross-section and the location for prestressing tendons.

Table 2.1. The prestressing tendons categorized in 26 groups.

Group	Prestressing tendon	Group	Prestressing tendon	Group	Prestressing tendon
1	1	10	6	19	6
2	1	11	6	20	2
3	2	12	6	21	1
4	2	13	8	22	6
5	2	14	8	23	6
6	2	15	8	24	2
7	4	16	14	25	2
8	4	17	8	26	28
9	1	18	8		

Perfect bond is assumed between the concrete and bonded tendons in the FEM simulation. As illustrated in Figure 2.4, 3D solid elements are used for concrete and 3D truss elements are used for the tendons. In the FEM implementation, the truss element 1 stands for the

prestressing tendon and the solid elements 2 and 3 stand for the concrete. The element 1 shares the identical nodes with elements 2 and 3, highlighted by the red circles. This means the three elements will have the same nodal displacement and no sliding at the shared nodes. In this chapter, five prestress levels, namely 600, 720, 840, 960 and 1080 MPa, are applied to study the effect of prestress on the long-term deformation of the bridge. The long-term prestress level in the bridge is most likely closely to 1080 Mpa (i.e. 0.58 f_{pu}).
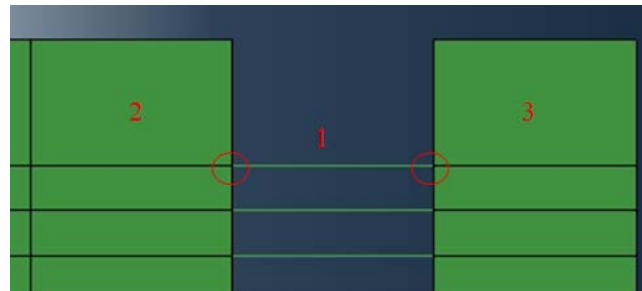
Figure 2.4. "Perfect bond" between the concrete and prestressing tendons in FEM simulation.

After meshing in ABAQUS, the bridge model contains 26,558 hexahedral elements and 11,793 truss elements; see Figure 2.2. To simulate the segmental construction procedure, which leads to a complex loading history in the tendons and concrete, the elements in the segments, for both concrete and steel, are deactivated at first and then progressively activated based on the construction sequence. Because no information is available for prestress adjustment after the construction of each segment, there will be a camber at the cantilever tip when the bridge is completed. In order to focus on only the post-construction behavior, this camber, different for each creep model, will not be considered in the deflection measurement.

2.3   LONG-TERM DEFROMATION ASYMPTOTES

In this investigation, the creep and shrinkage models of ACI (2008) [27], CEB-FIP (1990) [28], *fib* (2010) [19], B3 [14] and B4 [18] are used and the results based on these are studied. Among these models, ACI and CEB-FIP (1990) models are purely empirical and the only intrinsic parameter employed to represent concrete composition in their compliance formulas is the concrete compressive strength f_c'. The *fib* (2010) is similar to an older version, except for introducing the basic and drying creep similar to models B3 and B4 [38]. Among these models, model B3 and its successor model B4 are different because they are based on a solid mechanical basis: the solidification theory [14][16][17]. According to models B3 and B4, the concrete creep is the sum of basic creep and drying creep. The former is unbounded and consists of short-term strain, viscous strain and a flow term; while the latter is bounded and related to moisture loss. Multiple intrinsic parameters are employed to represent the concrete composition including water-cement ratio (w/c), aggregate-cement ratio (a/c), cement content (c) and concrete strength (f_c'). In model B4, the effects of admixtures, reactive additives, and type of aggregate on the creep and shrinkage behavior are taken into account [11]. The detail formulas of these different concrete creep models can be found in Chapter 1.2.

In order to isolate the differences resulting from the compliance function only, the same set of intrinsic input parameters is employed. Design compressive strength f_c' = 40 MPa is used for all models. Since the real concrete composition is unknown, the composition parameters are obtained based on a virtual mix design that will achieve the given concrete strength. Following the general practice [39] for 28-day standard cylinder compression strength f_c' = 40 MPa, the water to cement ratio by weight w/c = 0.35 is first determined according to Table 7.1 in [39]. By assuming that the maximum aggregate size to be 25mm and the slump is 50mm, the water

26

content per cubic meter is determined according to Table 7.8 in [39] and the cement content is found to be $c = 523.5$ kg/m^3. The weight of aggregates (both coarse and fine aggregates) is determined by subtracting the weights of water and cement from the total weight of concrete and is $a = 1832.25$ kg/m^3. In addition, all the extrinsic parameters, e.g., environmental humidity h and temperature T, construction sequence, curing time and external loads, are the same in all simulations. The mean values of input parameters used for different models are listed in Table 2.2 [40].

Table 2.2. Essential particles Mean and standard deviation of input parameters

Variable	Mean	Distribution type	Standard deviation	C.o.V
E_{28}	30,000 MPa	Lognormal	1,500	0.05
f_c'	40MPa	Lognormal	2.0	0.05
c	523.5 kg/m^3	Normal	104.7	0.2
w/c	0.35	Normal	0.07	0.2
a/c	3.5	Normal	0.7	0.2
h	0.7	Normal	0.035	0.05
T	20 °C	Normal	1.0	0.05
k	0.12	Normal	0.012	0.1
ρ_{1000}	0.035	Normal	0.0035	0.1
$\alpha_{PS,i}$	1.0	Normal	0.10	0.1

Using the improved rate-type formulation, the compliance functions of the creep models are converted to a system of Kelvin units based on the continuous spectrum method. The constitutive law of concrete, now represented by the properties of the Kelvin units, is added to ABAQUS by utilizing the user material subroutine *UMAT*. As for steel, a bilinear law

characterized by the Young's modulus and yield strength of steel is employed in the simulations. $E = 200$ GPa and $f_y = 1674$ MPa are selected for the prestressing tendons. After yield, the stiffness for prestressing tendons is assumed zero. Meanwhile, the steel relaxation is modelled based on the CEB relaxation formulas (CEB 1990) [28] and the related parameters are listed in Table 2.2.

In the simulations, five initial prestress levels (600, 720, 840, 960 and 1080 MPa, respectively) are considered to investigate the effect of prestress and its interaction with concrete creep on long-term deflection. The deflection history at the tip of the long cantilever under different prestress levels is plotted in Figure 2.5 for all creep models. In addition to the linear time scale displayed on the left, the same plot is also given in logarithmic time scale to highlight the long-term asymptote on the right. This is due to the fact that creep asymptote is conspicuous at logarithmic time scale if the model contains a logarithmic time function. Note that the reported deflection values refer to the reference state at the end of construction and any camber predicted at the end of the construction sequence is neglected.

For a large-span bridge, the evolution of the deflection is mainly governed by the competition between the self-weight (including sustained service load) and prestress force. In a cantilever box girder, if the compressive stress in the top slab is greater than the bottom slab, the cantilever will tilt up under the negative moment; otherwise, it will deflect downwards. This is illustrated in Figure 2.5 showing an increase of upward deflection with the prestress level. Due to concrete creep, the upward deflection will start to grow if the exerted compressive stresses induce more creep strain in the top slab than in the bottom slab. As time elapses, the compressive stress in the top slab will drop due to the prestress loss in the tendons, a collective result of

shrinkage, creep and relaxation. Consequentially, the growth of upward deflection will slow and downward deflection will start to develop.

The compliance functions of ACI and CEB-FIP (1990) are both bounded, which means creep will terminate after a certain amount of time. Therefore, the strain in the top slab will be stabilized and the deflection curve will approach a horizontal asymptote. Based on the ACI compliance function, it takes about 30 years for creep to terminate. After that, the deflection curve approaches a horizontal asymptote, as demonstrated in both linear and logarithmic scales in Figure 2.5(a), (b). This behavior, however, contradicts the bridge deflection trends reported in the recent survey of 56 girders [5].

In the case of the *fib* (2010) model the compliance function is unbounded due to the introduction of a split in bounded drying creep and unbounded basic creep. Thus, the compressive stress in the top slab will gradually decrease and the deflection curve will eventually approach an downward asymptote, which is conspicuous in the logarithmic time scale in Figure 2.5(c). Similarly, the compliance functions of basic creep in models B3 and B4 contain viscous and flow terms, which dictate an inclined asymptote too; see Figure 2.5(d), (e).

In addition to the long-term asymptote, the deflection history based on different models differs substantially, although equivalent intrinsic and extrinsic parameters are chosen. For the same level of prestress, the deflection curves of ACI and CEB-FIP are similar, with ACI developing more downward deflection than CEB-FIP. For both models, constant deflections are approached within about 30 years, independent of the prestress level; see Figure 2.5(a), (b). For *fib* (2010), the long-term creep is determined by the logarithmic time function of basic creep, which predicts greater and faster creep growth. Thus, downward deflection will grow and an inclined asymptote is approached in about 10 years in the logarithmic time scale. This is

evidenced by the deflection curves under initial prestress not greater than 840 MPa (Figure 2.5(c)).
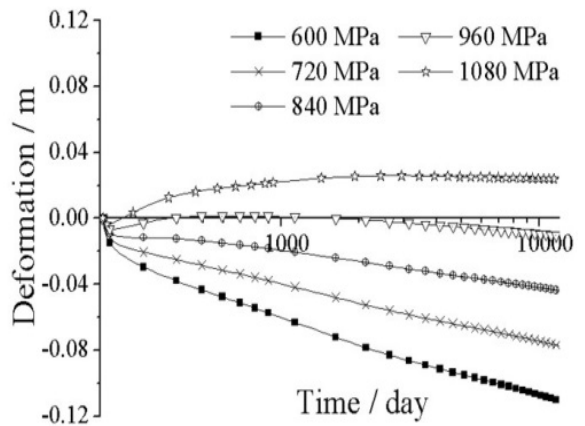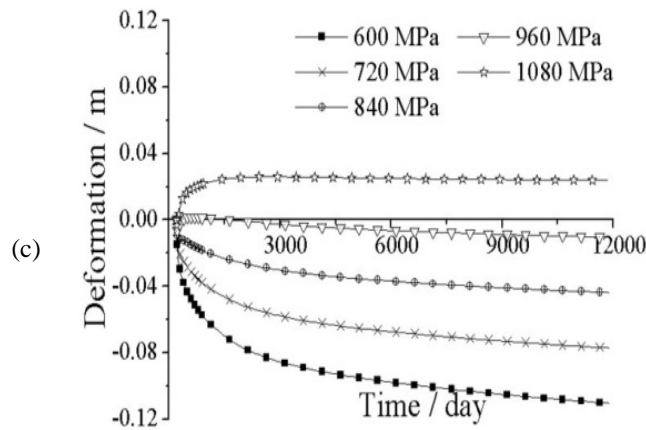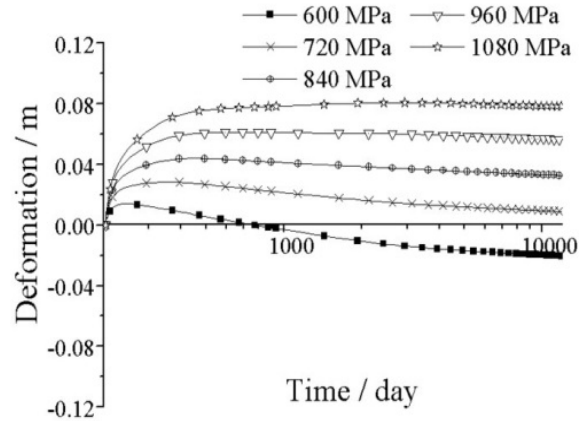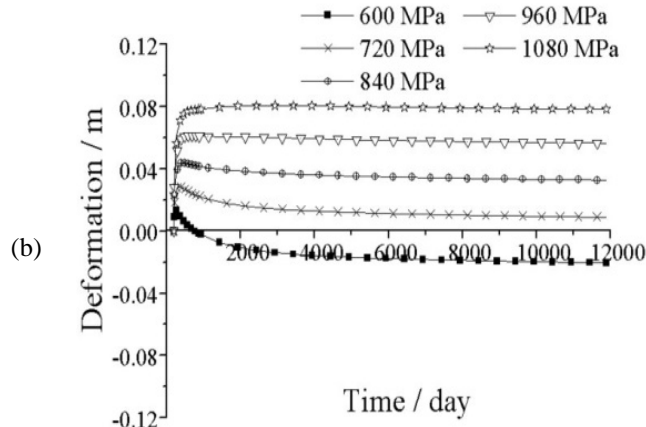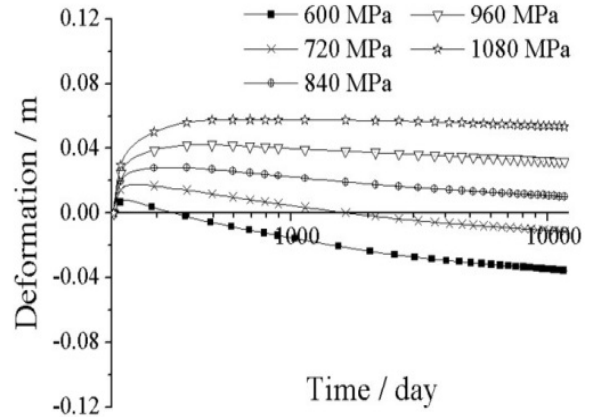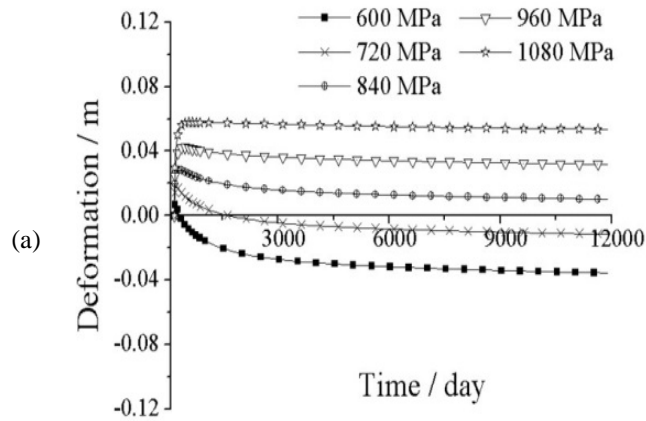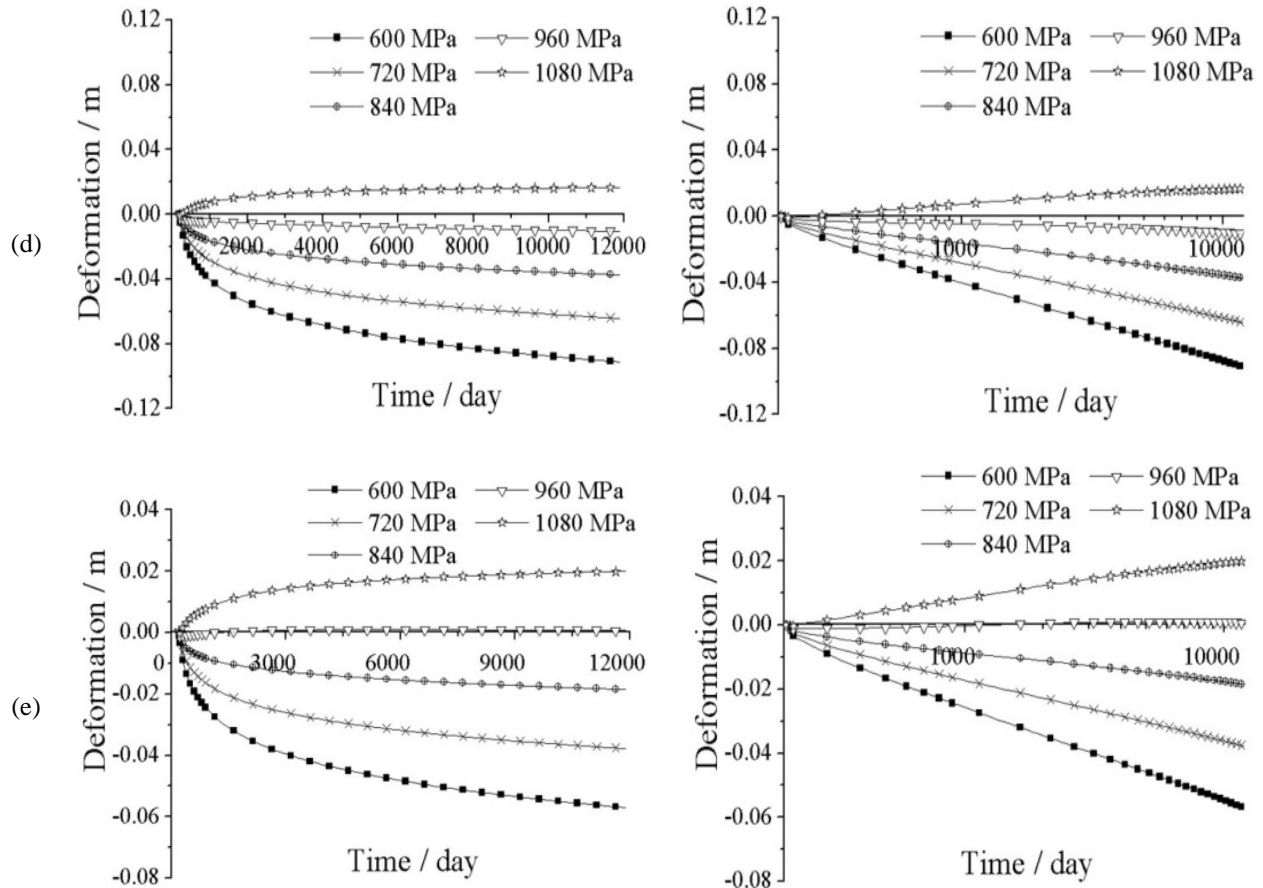
Figure 2.5. Vertical deflection history of long cantilever tip predicted by different creep models: (a) ACI model; (b) CEB-FIP(1990) model; (c) *fib*(2010) model; (d) B3 model; and (e) B4 model.

Among these models, models B3 and B4 are unique in that their viscous term plays an important role at early age and their flow term dominates the long-term behavior. Since both terms are expressed logarithmically in their compliance functions, their asymptotes are conspicuous in the logarithmic time scale. Similar to *fib* (2010), a downward slope is approached in about 10 years for initial prestress not greater than 840 MPa; see Figure 2.5(d), (e). While, for high prestress equal to 960 or 1080 MPa, the downward asymptote is not witnessed in Figure 2.5(d), (e) because the deflection curve is still in the transition from upward to downward. If the simulation is extended to 100 years, the downward asymptote appears (Figure 2.6). Therefore,

models B3/B4 as well as *fib* (2010) model eventually give a downward deflection as time goes to infinity.

Based on the captured long-term asymptotes, it can be seen there is a clear correlation between the deflection curve and compliance function. The establishment of this correlation depends on the properties of the compliance function, as well as the prestress level. Usually, this linear dependence develops quickly if the prestress level is low. For ACI and CEB-FIP (1990) models, this clear correlation will be developed in about 30 years after construction because of the nonexistence of logarithmic term in their compliance functions. For *fib* (2010) and B3/B4 models, which contain logarithmic terms, it can be approached at the 10th year if the prestress level is not high. For high prestress, the coincidence of the long-term asymptotes between the deflection and compliance is pushed back to 30 years or longer.
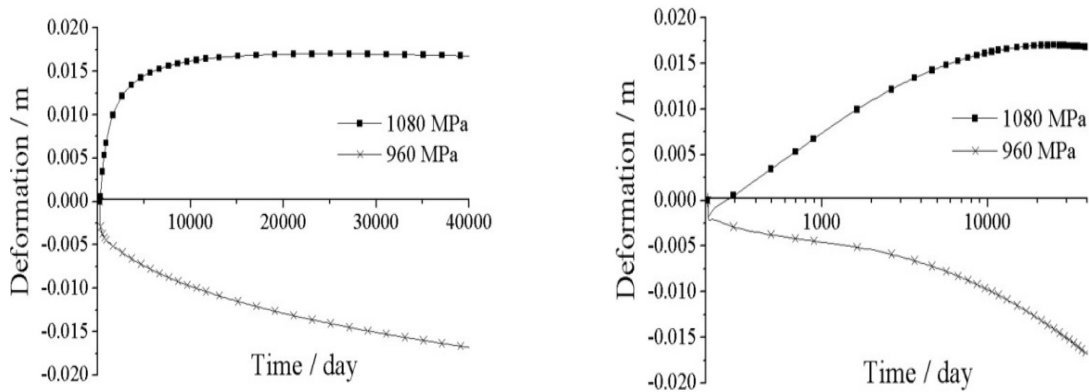
Figure 2.6. Simulations of two high prestress levels are extended to 100 years (based on B3 model): (Left) linear time scale, and (Right) logarithmic time scale.

2.4   STRESS EVOLUTION OF PRESTRESSING TENDONS

The main influences affecting the stress in the tendons are concrete creep and shrinkage, as well as steel relaxation. In this half section bridge model, there are 149 tendons in the top slab over Pier 1, which are prestressed in 26 groups (Figure 2.2(c)) to counteract the self-weight. Figure 2.7 shows the stress history of the total prestressing force at the location of Pier 1 based on different creep and shrinkage models. It can be seen that after a rapid drop, the total prestress loss is approaching an asymptote. Among the models, the *fib* (2010) predicts the highest prestress loss, which results in the largest downward deflection.
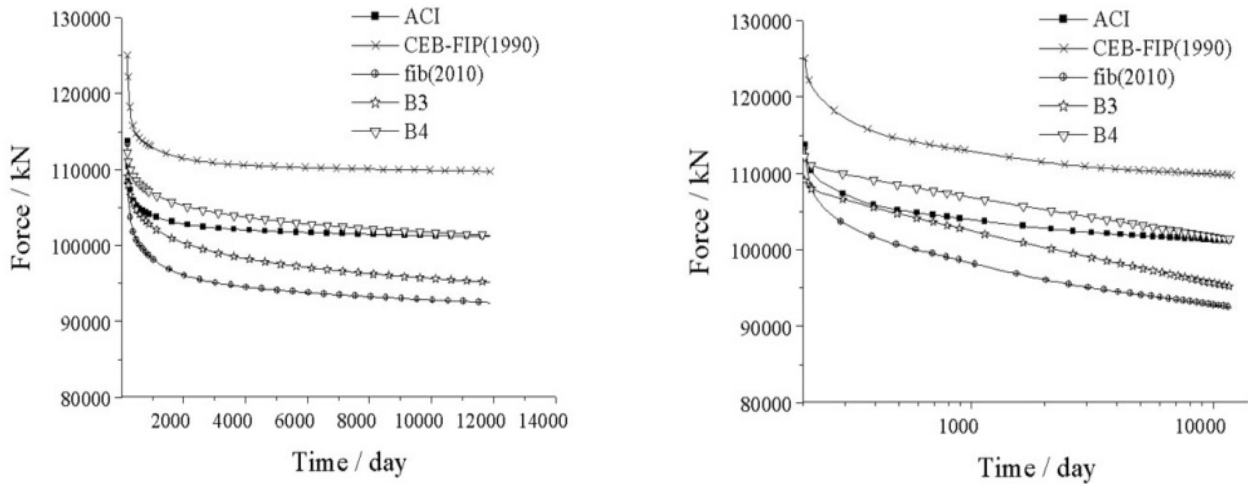
Figure 2.7. Total prestressing force at Pier 1 (half cross-section) based on initial prestress = 1080 MPa: (Left) linear time scale, and (Right) logarithmic time scale.

The stress history of an individual tendon group is more complicated. During construction, an instantaneous prestress loss will happen in the tendons whenever a new segment is stressed; see Figure 2.8. This is due to the elastic shortening caused by the prestress release in

the new segment. On the other hand, the self-weight and external loads in the new segment raise the stress level in the tendons. This competition, coupled with creep, shrinkage and relaxation, leads to a rather complex stress evolution in the tendons during construction (Figure 2.8).
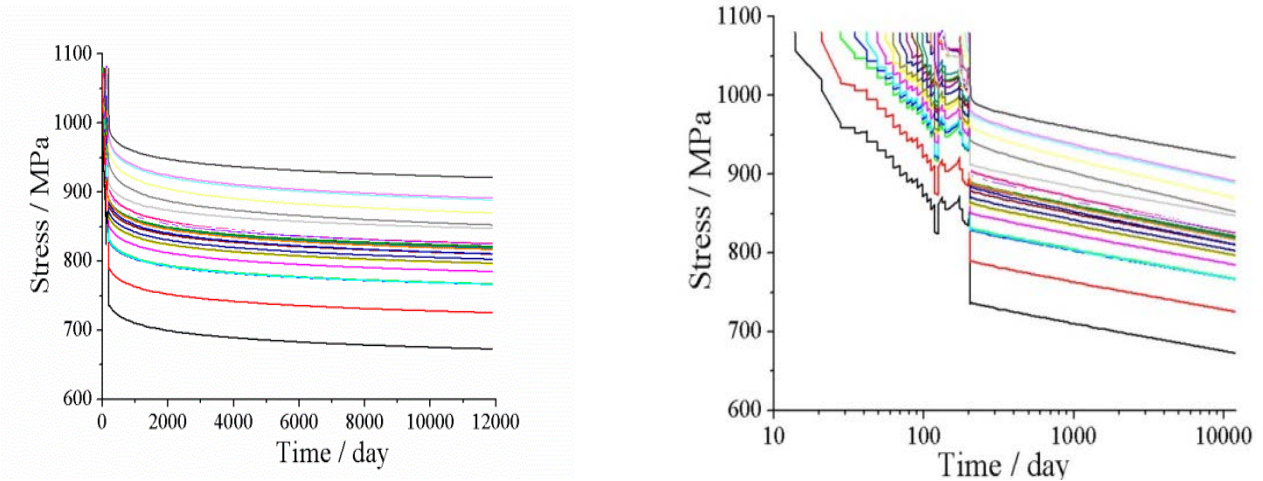
Figure 2.8. Prestress loss of 26 group tendons (based on B3 model): (Left) linear time scale, and (Right) logarithmic time scale.

However, after construction, the stress evolution in the tendons is steady, gradually approaching an asymptote as time elapses. This asymptote is mainly governed by the interaction between concrete creep and steel relaxation. For ACI and CEB-FIP (1990), the concrete creep will terminate because it is bounded in their compliance functions. Therefore, the slope of prestress loss in logarithmic time scale is dictated by steel relaxation (Figure 2.7). While for the *fib* (2010), or B3/B4 models, concrete creep is unbounded. Therefore, the slopes of prestress loss are steeper; see Figure 2.7. Note, in model B3, the prestress loss is not uniform and the prestress in some groups drops relatively faster, which is manifested by the crossing of curves in Figure

2.8. This implies that the deflection of the bridge is more sensitive to the prestress in these tendons.

2.5   CORRELATION BETWEEN THE SHORTENING AND CREEP ASYMPTOTE

Utilizing in-situ measurements to improve the predictive capacity of creep models garners increasing interest in practice because it brings benefits in estimating the long-term deformation as well as supplementing the short-term laboratory tests. Recently, a method [32] was proposed utilizing the deflection measurements 3 years after construction to obtain the long-term asymptote, i.e., using the slope of the deflection curve measured at the end of the 3rd year to extrapolate the long-term deflection. The reason to select the 3rd year is that the effects of differential drying and other short-term influences are no longer affecting the behaviors of bridges, and thus will not disturb the trend afterwards. However, this approach, built upon the correlation between the deflection curve and compliance function, has three main disadvantages:

- The proposed correlation is strongly influenced by the prestress level. For realistic prestress levels, like 1080 MPa used, this approach is not applicable because the deflection curve may still be in its transitional zone as shown by the simulations based on model B3 in Figure 2.6. Therefore, the slope of the deflection curve at the 3rd year cannot be used. Any realistic prediction has to wait for the deflection measurement after 30 years or longer; see Figure 2.6. This dependence on the prestress level was previously neglected and is hypothesized to be responsible for the significant amount of scatter in the inverse identification of long-term slope of the creep compliance as reported by Bažant and Hubler [32].

35

- The correlation between deflection and compliance function is established long after construction. As documented in Figure 2.5(c), (d), (e), the agreement of asymptotes is usually approached about 10 years after construction for *fib* (2010) and models B3/B4. This long duration complicates the practice of utilizing early-age measurements for long-term prediction. It also raises the risk that the asymptote will be contaminated by other coupled phenomena like fatigue and cracking. Thus, the use of the slope of long-term deflection to supplement the missing multi-decade laboratory data may distort any model calibration. Yet, bridge deformation measurements are so far the only available source of multi-decade information.

- The inverse analysis of deflection data to obtain creep compliance information as supplement to short-term creep tests is inconvenient. The reason is that the asymptote of a deflection curve is not directly related to the compliance function, as a consequence of the competing effects of self-weight and prestress. The geometrical characteristics of the segment, which determine the moments generated by the prestressing tendons, play an important role. Therefore, the governing parameters obtained based on this approach may demand complex treatment to avoid significant deviation from the real values.

To circumvent these obstacles, a more efficient and robust approach is proposed for models whose long-term behavior is governed by the logarithmic time function in the basic creep compliance functions. It is found that, if the shortening at the tip of the long cantilever is monitored, the shortening curve approaches its asymptote at a much earlier age than the deflection measurements, as evidenced by the simulations for *fib* (2010), B3 and B4. As for ACI and CEB-FIP (1990) containing no logarithmic terms, there is almost no advantage to use the shortening curve because it approaches the asymptote at about the same time as the deflection

curve, i.e., after 30 years; see Figure 2.9(a), (b). Although up to now no systematic collection of axial shortening information was attempted, this information was likely recorded in course of inspections to judge the performance of expansion joints and bearings.

For *fib* (2010) and B3/B4 models, unlike the deflection measurement, the trend captured in shortening curves is consistent, and negligibly disturbed by the prestress level. For example, after 3 years, the shortening curves approach a constant slope in the logarithmic time scale; see Figure 2.9(c), (d), (e). The close correlation is established at the 3rd year even for the highest prestress level (1080 MPa), while, for deflection curves, this only happens for the lowest prestress level, i.e., 600 MPa. At the initial prestress level of 1080 MPa, this point is delayed to an age of over 30 years because of the long transitional period shown in Figure 2.6.
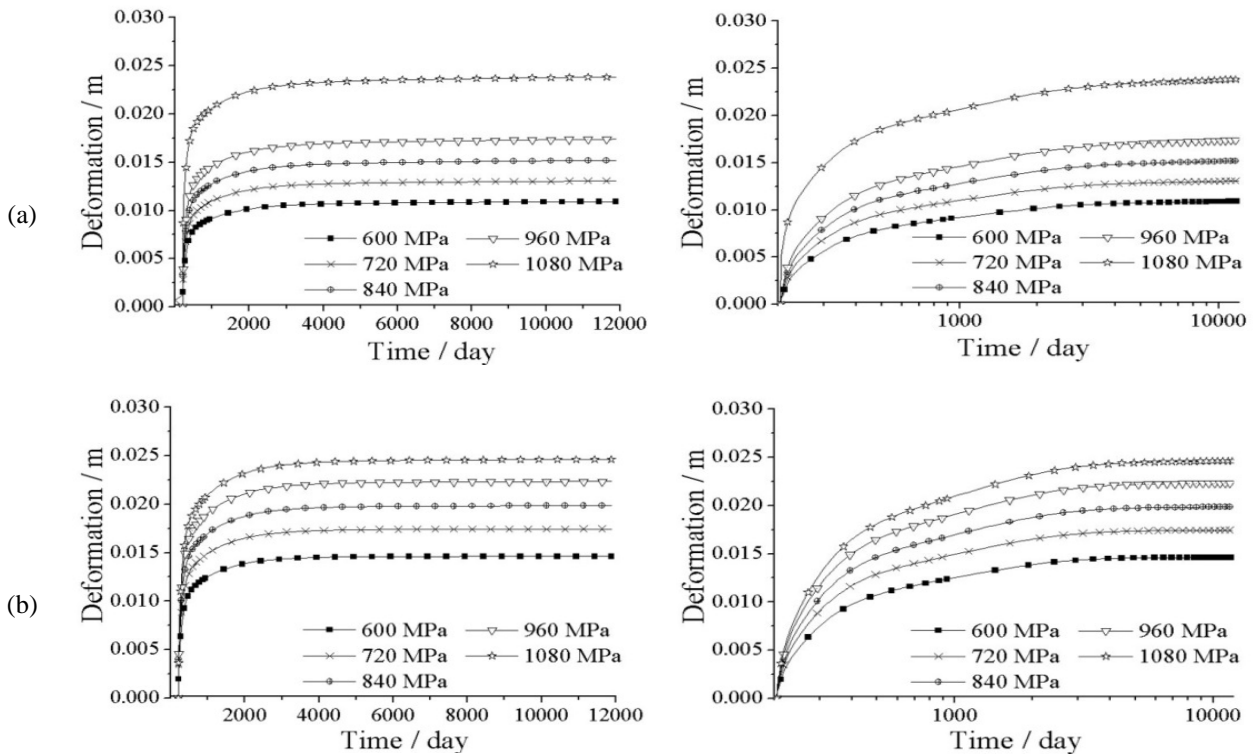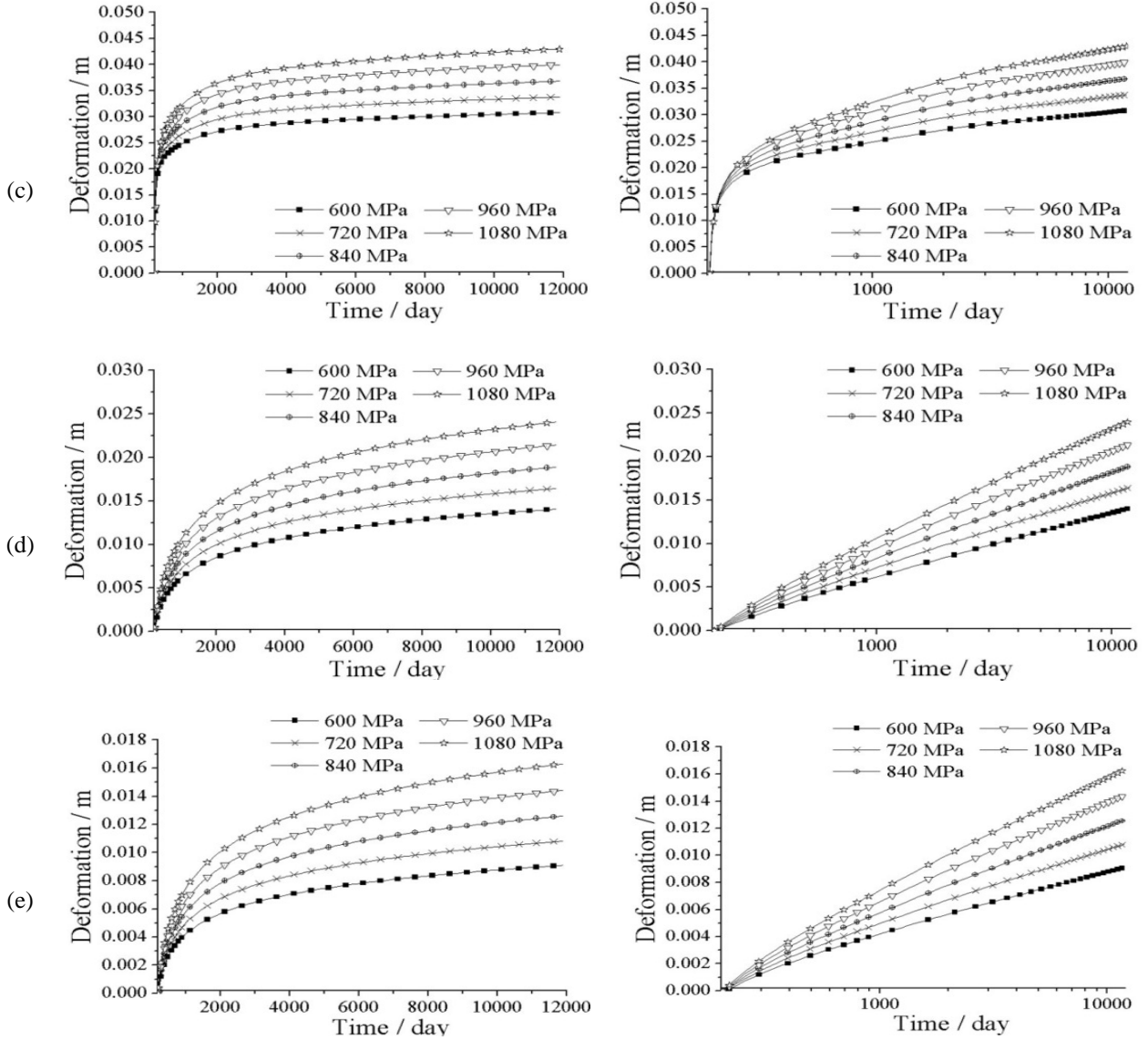
Figure 2.9. Long cantilever shortening based on different creep models: (a) ACI model; (b) CEB-FIP (1990) model; (c) *fib* (2010) model; and (d) B3 model; and (e) B4 model.

The reason for the promptness and consistency is that the shortening curve is directly related to the creep compliance function by the average compressive stress on the cross section. After the short-term influences decay, the strain change during a time increment from t_1 to t_2 in the cantilever beam can be written as:

$$\Delta\varepsilon = [J(t_1,t_0) - J(t_2,t_0)]\sigma + J(t_2,t_1)\Delta\sigma \tag{2.1}$$

where both t_1 and t_2 are much greater than t_0 when the load is initially applied. Because the stress increment $\Delta\sigma$ during Δt is negligible compared to the prestress σ and $J(t_2, t_1)$ is insignificant for aged concrete, Eq. (2.1) can be simplified as

$$\Delta\varepsilon = [J(t_1,t_0) - J(t_2,t_0)]\sigma \tag{2.2}$$

For models containing logarithmic terms, after the short-term influences attenuate, the asymptote will be dictated by the logarithmic terms. For example, in model B3, its compliance is governed by the viscous and flow terms as follows:

$$J = q_3 \ln(1 + (t - t_0)^n) + q_4 \ln\frac{t}{t_0} \rightarrow J \approx (nq_3 + q_4)\ln t \tag{2.3}$$

Based on Eq. (2.2) and Eq. (2.3), we get

$$\Delta\varepsilon = (nq_3 + q_4)\sigma\Delta\ln t \tag{2.4}$$

Thus, in the logarithmic time scale, the asymptote is a straight line with slope = nq_3+q_4. For a cantilever box girder consisting of m segments, the change of its total shortening can be written as:

$$\frac{\delta}{l} = (nq_3 + q_4)\sum_{i=1}^{m}\frac{l_i\sigma_i}{l}\Delta\ln t \tag{2.5}$$

where δ is the change of the total shortening of the cantilever of length l, σ_i is the effective stress in the i-th segment of length l_i.

Eq. (2.5) shows that the governing parameters of a given compliance function and the creep trend can be estimated based on the total shortening, if the effective stress in each segment is known and the slope of the shortening curve at the 3rd year is measured. For simplicity, the initial prestress in each tendon is used and the average cross section of the segment to calculate

the effective stress σ_i. Now, it is found that the ratios of nq_3+q_4 obtained based on Eq. (2.5) to the theoretical values used in the material subroutine are 1.152, 1.11, 1.10, 1.09 and 1.09 for prestress = 600, 720, 840, 960, and 1080 MPa respectively. The minor deviation is mainly due to the errors in σ_i and the sequential construction, which causes the prestress release time t_0 to be different for each segment. However, considering the typical scatter found in concrete creep, the predictions based on Eq. (2.5) are satisfactory and sufficiently consistent.

2.6   INFLUENCE OF PRESTRESS VARIABILITY

As shown in Figure 2.8, the change of prestress loss is not uniform in all tendon groups. This means that deflection is more sensitive to some groups of tendons than others. To study this sensitivity, first a deterministic study based on the model B3 with initial stress = 1080 MPa is performed. The change of deflection caused by a 10% decrease of initial prestress in an individual tendon group while the prestress levels of the other groups remained unchanged is simulated. The deflection variations, compared to the deterministic simulation result, are shown in Figure 2.10. For most groups, the variation of the prestress level has negligible influence on the deflection of the cantilever tip. However, several groups have significant impacts on the deflection. A 10% prestress drop in group 16 and 26 causes a 20% and 50% deflection growth, respectively. The disproportional variation is closely related with the tendon number (Table 2.1) and distribution inside the individual tendon group. The groups 16 and 26 correspond to the completion of the short cantilever and long cantilever, respectively, and therefore contain more tendons than other 24 tendon groups.
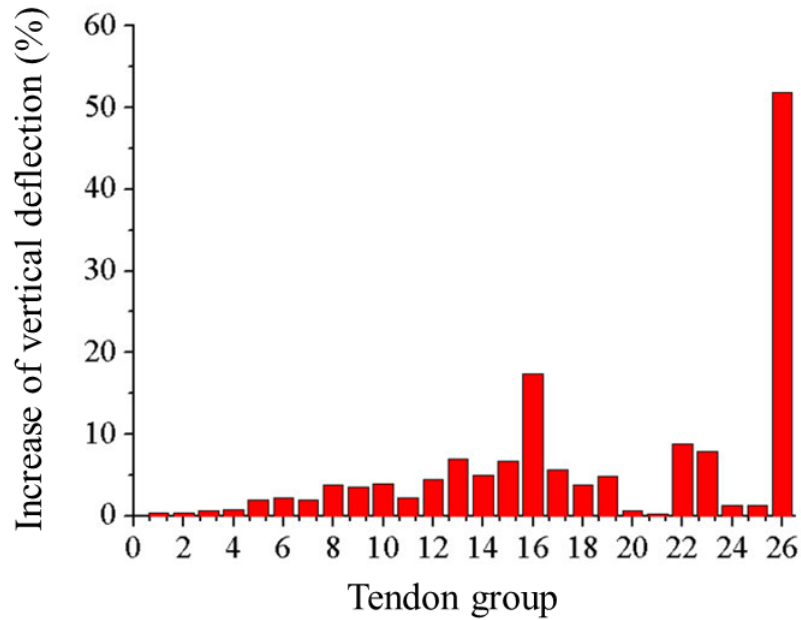
Figure 2.10. Effect of 10% prestress loss on the vertical deflection of the long cantilever.

2.7   PROBABILISTIC SENSITIVITY STUDY

In order to systematically study the effects of variations of the influencing parameters on bridge deformation, which are known to show large scatter, a probabilistic analysis is performed. The correlation between deformation asymptote and creep compliance function is investigated based on model B3 with initial prestress being 1080MPa. The results apply equally to model B4. In Table 2.2, the stochastic models with mean values identical to the deterministic investigation are presented. For the 28-day concrete modulus E_{28} and compressive strength f_c', the coefficient of variation (C.o.V.) is set as 5%, as for this kind of large-span bridges, quality control is strict. The C.o.V. for temperature and humidity is 5%, since they are both annual average values and climate change is not considered. For the relaxation parameters, C.o.V. = 10% or higher is used because the collected databases show that the results of relaxation are scattered. The variability

in the initial prestress level is modelled by uncertainty factors $\alpha_{PS,i}$ with C.o.V. being 10%. These parameters are generated according to the reference [40].

No statistical dependence between the variables is considered with the exception of the concrete properties. Table 2.3 gives the correlation matrix that is described by pairwise linear correlation coefficients according to Pearson [41] and Stigler [42].

Table 2.3. Correlation matrix of concrete properties

	E_{28}	f_c'	c	w/c	a/c
E_{28}	1	0.19	0.06	-0.07	0.05
f_c'	0.19	1	0.5	-0.52	0.36
c	0.06	0.5	1	-0.86	-0.86
w/c	-0.07	-0.52	-0.86	1	0.8
a/c	0.05	0.36	-0.86	0.8	1

The Latin hypercube sampling scheme [36] combined with simulated annealing [43][44] guarantees a lower number of samples can be used to reasonably approximate the statistical characteristics of the marginal distributions as well as their statistical dependence [45]. For this investigation a population size of 45 samples is generated based on all the statistical varieties [40].

In Figure 2.11, the variability in the horizontal shortening of the long cantilever is presented in terms of the individual response curves (grey), the mean value response (bold line), the 5% and 95% confidence bounds and the empirical cumulative distribution at 1133, 4233, and 8833 days, respectively. After about 12 years the modelled variability in the input parameters causes 15.3% scatter in the predicted bridge shortening with a mean response of 1.9 cm. It

implies that the axial shortening of the bridge is not sensitive to the coupling of randomness and variation from different sources. According to the test by Monahan [46] the best fitting distribution changes from a 3-parameter lognormal for early ages to a Gumbel EV1 distribution for long-term predictions.
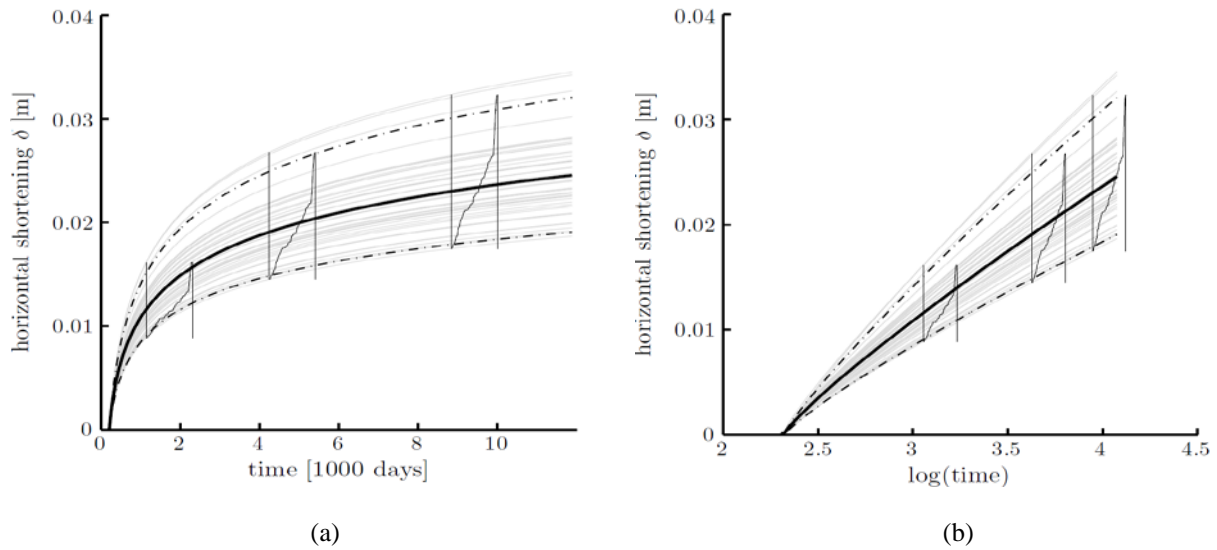
Figure 2.11. Statistical analysis of shortening of the long cantilever in: (a) linear, and (b) logarithmic time.

Although this figure shows a certain amount of scatter, the bridge shortening is consistent. No elongation is observed for the axial deformation. On the other hand, the predicted vertical deformation displays a wide scatter band, ranging from upward camber to downward deflection, see Figure 2.12. The scatter for the 12-year prediction almost approaches a coefficient of variation of 72 %. Considering the variability of input parameters, the deflection is sensitive to the coupling of randomness and variation from different sources. With increasing age the distribution converges towards Gaussian.
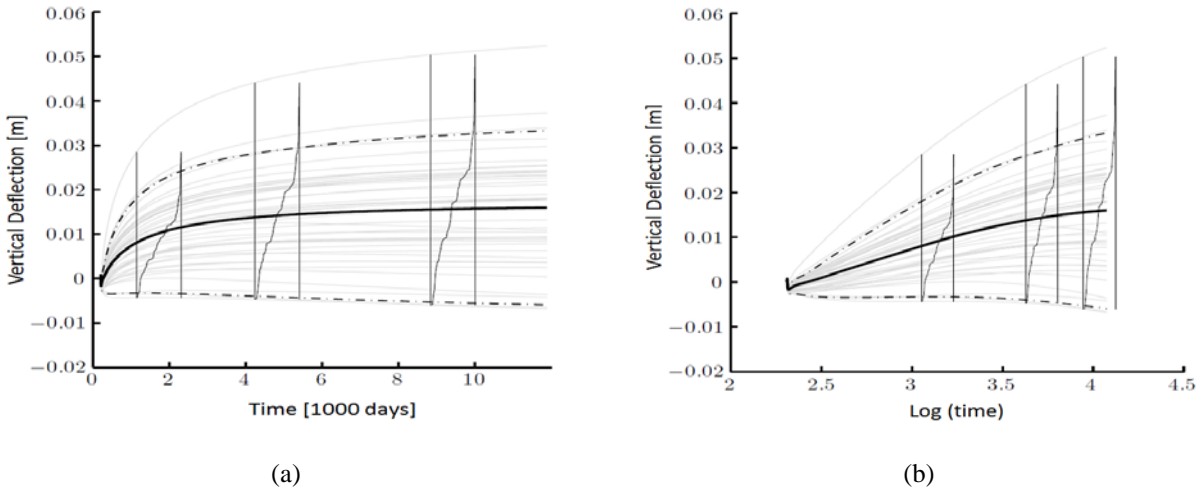
Figure 2.12. Statistical analysis of vertical deflection of the long cantilever in (a) linear, and (b) logarithmic time.

The results of shortening and deflection for the short cantilever are plotted in Figure 2.13 and Figure 2.14 in both linear and logarithmic scale, respectively. Compared to the long cantilever the predicted trends are more consistent with qualitatively similar scatter. Only one sample shows an upward camber. The 12-year scatter amounts to 13.8% for shortening and 34% for vertical deflection. The comparison reveals, as expected, a close correlation between axial shortening and creep asymptote.

(a)   (b)
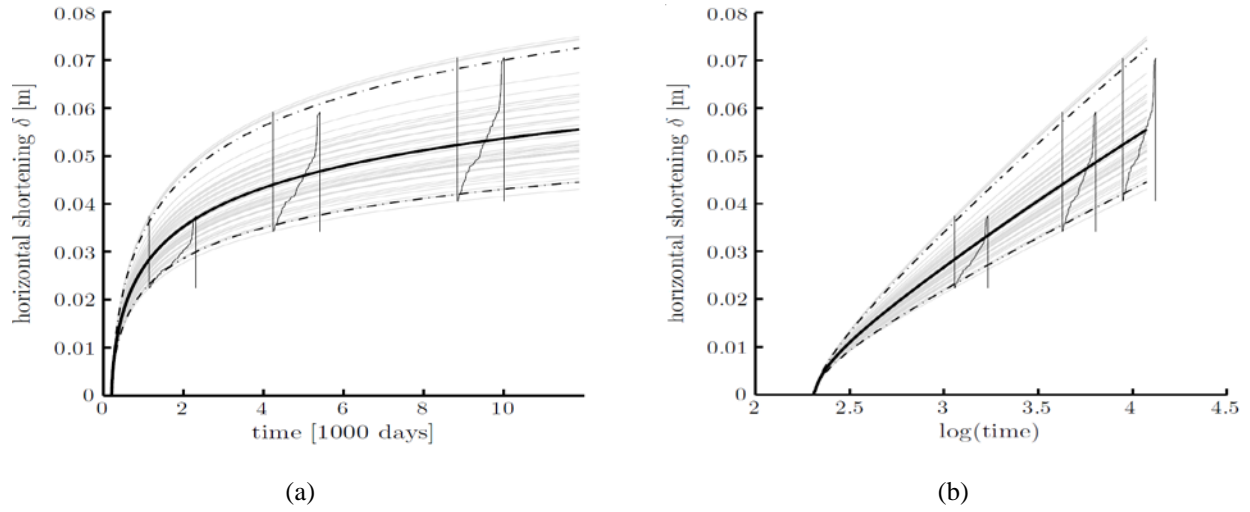
Figure 2.13. Statistical analysis of shortening of the short cantilever in (a) linear, and (b) logarithmic time.

(a)   (b)
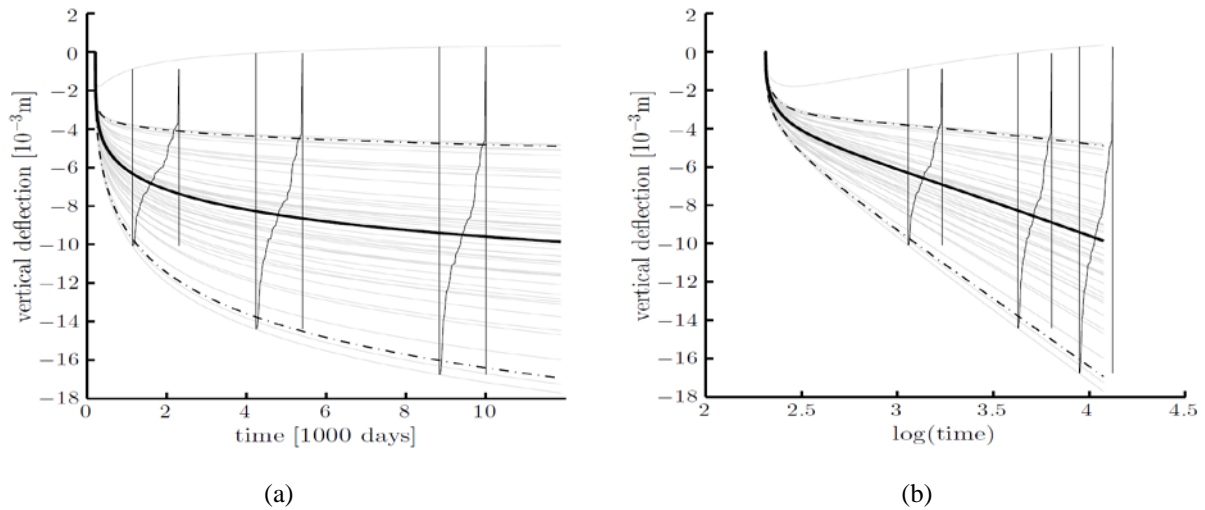
Figure 2.14. Statistical analysis of vertical deflection of the short cantilever in: (a) linear, and (b) logarithmic time.

The prestress force at the Pier 1 is significantly influenced by concrete creep as well as steel relaxation and prestress level. Figure 2.15 shows the scatter band for the prestressing force.

The scatter, however, is significantly smaller and amounts to only 3.6% after 12 years. The best fitting distribution in this case is the 3-parameter Weibull min distribution. On top of a quantification of uncertainty in long-term predictions a primary goal of this investigation lies in the determination of sensitivities between input parameters and structural response, namely deformation. These sensitivities can be expressed in terms of sensitivity factors α. The values of dominating variables have to be selected carefully and variables with low sensitivity can be ignored. A straightforward and simple approach to obtain sensitivity factors is based on the non-parametric rank-order statistical correlation between input variables and structural response variables. The relative effect of each input variable (generated samples) on the (simulated) structural response can be measured using the partial correlation coefficient. The method is based on the assumption that the random variable which influences the response variable more considerably (either in a positive or negative sense) has a higher correlation coefficient than other variables. Since the model for the structural response is generally nonlinear, a non-parametric rank-order correlation is used, quantified by means of the Spearman correlation coefficient a or Kendall τ.
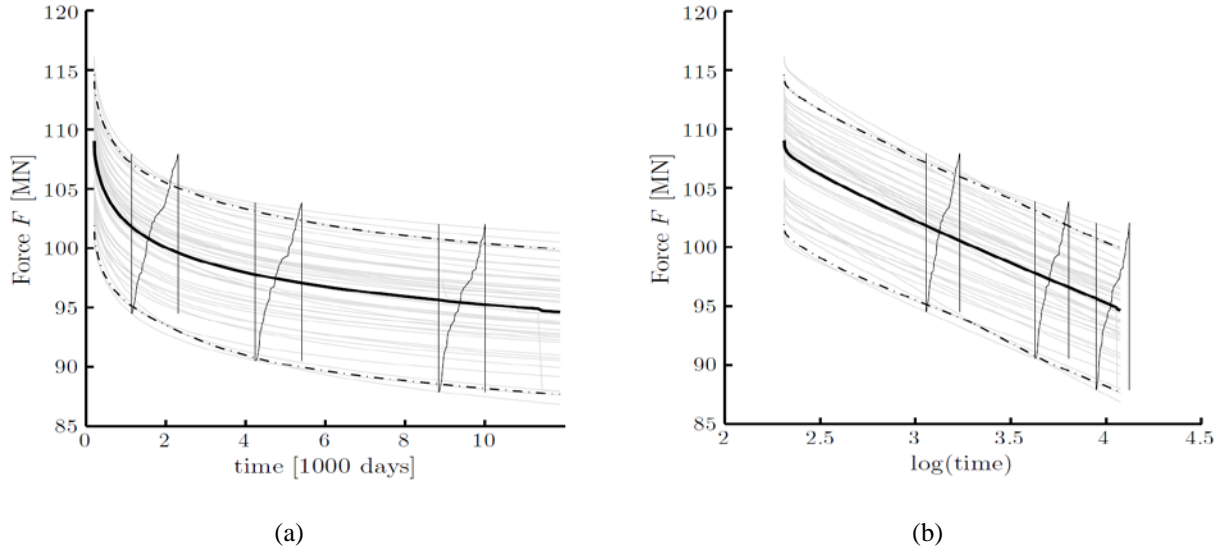
Figure 2.15. Statistical analysis of prestressing force at the Pier 1 in (a) linear, and (b) logarithmic time.

A sensitivity analysis reveals that the shortening of the cantilever is primarily governed by the concrete composition parameters followed by the prestress levels of a selected few tendon groups. With time increasing, the influence of composition parameters rises and the parameters of the relaxation function slowly gain in importance. After 12 years, the most significant input parameters are the aggregate to cement ratio with a sensitivity factors $\alpha_{a/c} = -0.94$, the cement content with $\alpha_c = 0.82$, the compressive strength with $\alpha_{f/c} = 0.31$, and the water to cement ratio with $\alpha_{w/c} = -0.71$. The sensitivities for the shortening of the short cantilever are very close.

In addition to showing a significantly larger scatter, the sensitivity analysis of vertical deflection reveals a reduced sensitivity to the input parameters of the creep model. The most significant 12 year sensitivity factors are $\alpha_{PS26} = 0.67$, $\alpha_{a/c} = -0.44$, $\alpha_c = 0.40$ and $\alpha_{w/c} = -0.39$. In case of the short cantilever, the influence of prestressing levels is even more significant. Out

47

of the first 10 most significant input variables, 9 are prestressing correction factors, or related to steel relaxation.

According to the sensitivity study, the prestress force at the Pier 1 is mainly determined by the prestress of tendon group 26, followed by the concrete composition parameters a/c, c, and w/c. The most significant 12 year sensitivity factors are: $\alpha_{PS} = 0.89$, $\alpha_{a/c} = 0.24$, $\alpha_c = -0.23$ and $\alpha_{w/c} = 0.19$.

Based on the presented sensitivity analysis it can be concluded that vertical deflections show significantly higher scatter and lower sensitivity to creep. Thus, shortening measurements are a better source of information for inverse analysis of creep models as well as long-term predictions.

2.8   SUMMARY

The investigation of the Colle Isarco Viaduct Bridge in this chapter shows that for structural analyses of large creep-sensitive structures, a 3D rate-type approach powered by exponential algorithm and enriched by the continuous retardation spectrum method brings in the benefits of computational efficiency as well as allows the coupling with memory-independent phenomena. Some conclusions can be obtained based on this case study:

1.   The simulations based on a large-span prestressed concrete bridge show that the asymptotes of long-term deflection and axial shortening as well as their curves are very different for different creep models. For creep models containing logarithmic time functions, the deflection and shortening asymptotes eventually approach an inclined straight-line in logarithmic time scale.

48

2. The prestress level in the tendons is critical for achieving the deflection asymptote. If high initial prestress is applied, the arrival of the deflection asymptote will be pushed back to over 30 years due to the long transitional period. Thus, an early establishment of the correlation between creep compliance function and deflection asymptote cannot be achieved.

3. On the other hand, the axial shortening is not sensitive to the prestress level. For initial prestress ranging from 600 to 1080 MPa, the axial shortening consistently reaches its asymptote in about 3 years or earlier. Therefore, an early establishment of correlation between creep compliance function and shortening asymptote can be achieved and then used to predict the long-term bridge deformation as well as supplement the laboratory tests.

4. Statistical analysis based on Latin hypercube sampling scheme shows the coupling of randomness and variation of influencing parameters in creep structural analysis does not augment the scatter of the axial shortening, which consistently approaches its asymptote in about 3 years. Contrarily, the combination of variability of input parameters will magnify the scatter band of the deflection curve and the arrival of deflection asymptote is severely disturbed.

5. Utilizing the early-age in-situ measurement of bridge deformation to improve the creep models so as to enhance the prediction of long-term deformation is a promising approach of both academic and practical significance. The consistency and robustness displayed in the correlation between asymptote of axial shortening and creep compliance function makes axial shortening a good candidate for in-situ monitoring.

3.0 THE INTERTWINED EFFECTS OF CONCRETE DAMAGE, STATIC CREEP AND TRAFFIC-INDUCED CYCLIC CREEP

3.1 MOTIVATION AND BACKGROUND

Until now, deflection studies are almost exclusively focused on the viscoelastic behavior triggered by the static creep of concrete and its effect on the deflection history of prestressed concrete bridge [3]. Nevertheless, this means that the advantages of 3D rate-type formulation of creep analysis, like approximating concrete ageing, concrete creep coupled with damage, shear lag and variations in the environmental conditions, are not fully exploited. The interaction between concrete creep and cracking attracts very limited attention in full-scale creep structural analysis. Some oversimplified methods, for example, quasi-elastic stress-strain relations equipped with a plastic tensile limit [4], are frequently used in creep analysis to approximate concrete responses after cracking. As a consequence, the coupled effects of concrete creep, softening and cracking on the deflection evolution and stress redistribution may be ignored or inadequately estimated in creep structural analysis. However, in reality, the excessive deflection of a prestressed concrete bridge is generally accompanied with the concrete cracking. In addition to static creep due to sustained stress, stress fluctuation induced by traffic loads will cause cyclic creep in concrete. For large-span prestressed concrete bridges, it is found that if the total traffic volume throughout the bridge lifespan is not significant, the effect of cyclic creep on the

deflection growth is not important [47]. Therefore, the time-dependent process triggered by the cyclic creep of concrete is usually neglected in multi-decade deflection predictions.

Increasing demands for sustainable transportation call for considerations of the cracking and cyclic creep of concrete in creep structural analysis. Because the heavy traffic flow and concrete cracking will lead to much more severe stress redistribution of the bridge. Thus, the intertwined effects of concrete static creep, cyclic creep, softening and cracking need to be considered to ensure the serviceability and safety of bridges. To meet this need, a unified constitutive model, which incorporates static creep, cyclic creep and fracture behavior of concrete, is developed and then integrated in the 3D rate-type formulation for the full-scale creep structural analysis. In this unified constitutive model, the rate-type formulation of concrete static creep hinging on the Kelvin chain model (which is described in Chapter 1.3) is utilized. Then a cyclic creep model based on the fatigue growth of microcracks is added in the nonlinear stress-strain incremental relation. Subsequently, an elasto-plastic damage model is employed to describe the concrete softening and cracking under complex stress states. The interactions between the static creep, cyclic creep and concrete cracking are integrated into a unified framework, which can be implemented in a general-purpose FEM program, e.g., ABAQUS. Based on the proposed unified framework, a case study is carried out to investigate the performance of a large-span prestressed concrete bridge. Finally, the results obtained by the numerical simulations are presented and discussed.

3.2   CYCLIC CREEP OF CONCRETE

Different from other creep-sensitive structures, the service load on prestressed concrete bridges fluctuates constantly due to the passing vehicles. The stress variation complicates the viscoelastic behavior of concrete by inducing another type of complex time-dependent deformation, namely cyclic creep, which was initially discovered in 1906 by Féret [48] and then extensively studied by many researchers [49]-[51].

Despite some theoretical attempts based on qualitative terms [52][53], empirical models are predominantly used in current practice to predict the cyclic creep of concrete. In these models, the cyclic creep is usually calculated as an additional inelastic strain [54]-[56] or treated as an acceleration of static creep [49][57]. Although these empirical models generally agree with short-duration tests, their predictive capacity for long-term behavior is inadequate because the phenomenological formulations used are seldom anchored in a mechanistic model capable of describing the microstructure change induced by cyclic loading.

In this chapter, a fatigue mechanics-based model proposed recently by Bažant and Hubler [47] is utilized to estimate the cyclic creep of concrete. In this model, which is different from the purely macroscopic formulation, the cyclic creep is considered as the macroscopic deformation induced by the fatigue growth of the pre-existing microcracks in concrete.

Concrete is full of flaws and preexisting cracks, and the microcracks will grow under the fatigue load. Suppose that the volume per microcrack is l_c^3 and all the microcracks are perpendicular to the direction of applied stress, according to the Castigliano's theorem [47][58], the displacement u per crack can be calculated as:

$$u = [\frac{\partial \Pi^*}{\partial P}]_{a_c} = \frac{1}{l_c^2}[\frac{\partial \Pi^*}{\partial \sigma}]_{a_c} = \frac{\gamma_0}{El_c^2}\sigma a_c^{\ 3} \tag{3.1}$$

where Π^* is the complementary energy (Gibb's free energy) per microcrack; σ is the applied remote stress; P is the remote applied force and $P = l_c^2\sigma$; and γ_0 is a dimensionless constant characterizing the geometry. Hence, the macroscopic strain caused by the formation of the microcrack of size a_c is:

$$\varepsilon^{cc} = \frac{u}{l_c} = \frac{\gamma_0}{El_c^3}\sigma a_c^{\ 3} \tag{3.2}$$

The total microcrack size increment over N_c cycles is $\Delta a_{Nc} = a_{Nc} - a_{0c}$, where a_{Nc} is crack size after N_c cycles and a_{0c} is the initial crack size. Suppose the creep strain is small ($\Delta a_{Nc}/a_{0c} \ll 1$), after N_c cycles, the strain increment due to cyclic loading is:

$$\Delta\varepsilon^{cc} = \frac{\gamma_0}{El_c^3}\sigma(a_{Nc}^3 - a_{0c}^3) \approx 3\gamma_0\frac{\sigma}{E}(\frac{a_{0c}}{l_c})^3\frac{\Delta a_{Nc}}{a_{0c}} \tag{3.3}$$

Except for the very large stress amplitude and very high stress level, the fatigue growth of the microcrack depends on the amplitude of the stress intensity factor ΔK and follows the Paris' law:

$$\frac{\Delta a_N}{N} = \lambda(\frac{\Delta K}{K_c})^m \tag{3.4}$$

where K_c is the critical stress intensity factor; λ and m are empirical constants. The amplitude ΔK is proportional to the remote applied stress amplitude $\Delta K = z\sqrt{a_c}\Delta\sigma$.

For very large or small ΔK, the crack growth rate deviates from the slope m. Nevertheless, the Paris' law can accurately approximate the intermediate range of fatigue crack growth, when ΔK exceeds certain threshold. With the Paris' law, we can arrive at:

$$a_{Nc} - a_{0c} = \lambda \left(\frac{z\sqrt{a_c}\Delta\sigma}{K_c}\right)^m N_c \tag{3.5}$$

Substituting Eq. (3.5) into Eq. (3.3), we can obtain the strain increment due to cyclic creep after the N_c cycles:

$$\varepsilon^{cc} = C_1 \sigma \left(\frac{\Delta\sigma}{f_c'}\right)^m N_c \tag{3.6}$$

where C_1 is expressed as:

$$C_1 = \frac{3\gamma_0}{E} \frac{\lambda}{a_{0c}} \left(\frac{za_{0c}}{l_c}\right)^3 \left(\frac{f_c'\sqrt{a_{0c}}}{K_c}\right)^m \tag{3.7}$$

in which f_c' is the compression strength of concrete.

It is noted that the cyclic creep strain tensor ε^{cc} is dependent on both σ and N_c linearly, this agrees with the available cyclic creep measurements and is convenient for structural analysis. Through experimental calibration, the exponent value m is found to be 4 [59][60] and the coefficient C_1 is about 46×10^{-6} [47].

For large-span prestressed concrete girders, the average stress σ in Eq. (3.6) can be approximated by the stress induced by the dead load, which is much greater than that from vehicular line loading. However, the amplitude of stress variation $\Delta\sigma$ varies due to the travel of different types of vehicles on the girders. Thus, the time shape of a load cycle on a bridge is quite different from the symmetric and periodic ones used in the experiments. To avoid the complication caused by the randomly varied $\Delta\sigma$, a simplified cyclic shape with constant amplitude, which is the time average of different vehicles, is adopted by using Eq. (3.8).

Since cyclic creep is treated as macroscopic deformation induced by the fatigue growth of pre-existing microcracks in the model, this simplified cyclic waveform must generate the

54

same amount of microcrack advance after the same number of cycles when compared to the real waveform of varied amplitude. This requires

$$\int_0^{t_N} C\Delta\sigma(t)^m \, dt = \int_0^{t_N} C\overline{\Delta\sigma}^m \, dt \tag{3.8}$$

where $\Delta\sigma(t)$ represents the random amplitude of the real waveform, $\overline{\Delta\sigma}$ represents the constant amplitude of the simplified waveform and C is a constant. The evaluation of the integral on the left side of Eq. (3.8) is a challenging task because the cycle-cycle interactions are complicated [61]. Since the concrete is generally designed to be under service condition and the amplitude of cyclic load due to traffic is usually low in large bridges, one can simplify this evaluation by assuming that the crack growth increment per cycle is equal to the crack growth rate under constant amplitude loading of the same magnitude [61].

Suppose during a fixed time, two different types of vehicles pass across the bridge, leading to the different stress variations $\Delta\sigma_1$ and $\Delta\sigma_2$, respectively, with different cycles N_1 and N_2, respectively; see Figure 3.1. The constant amplitude of the simplified waveform $\overline{\Delta\sigma}$ is obtained according to:

$$C(\frac{\Delta\sigma_1}{f_c'})^m N_1 + C(\frac{\Delta\sigma_2}{f_c'})^m N_2 = C(\frac{\overline{\Delta\sigma}}{f_c'})^m (N_1 + N_2) \tag{3.9}$$

Typically, $\overline{\Delta\sigma}$ will fall between $\Delta\sigma_1$ and $\Delta\sigma_2$.
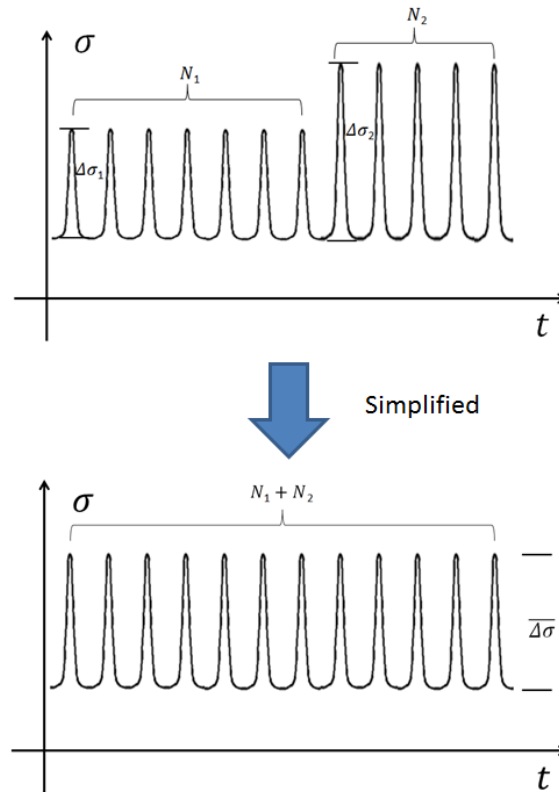
Figure 3.1. Stress fluctuation due to traffic on the bridge and the simplified cyclic load shape for concrete cyclic creep.

3.3   ELASTO-PLASTIC DAMAGE MODEL FOR CONCRETE

To capture the instantaneous responses of concrete under complex stress states, constitutive models based on different theories and formulations have been constructed. Among the continuum models available, the elasto-plastic damage model is selected. The advantages of this model are that: (1) it is capable of capturing the concrete cracking in tension and softening/hardening under low-confined compression, which is typical for prestressed concrete, and (2) the concept of effective stress and the hypothesis of equivalent strain enable the straightforward coupling of concrete cracking with creep structural analysis. The important

56

concepts of this model are briefly introduced here and the detailed process is referred to the recent comprehensive studies [62]-[64].

In this model, the effective stress $\bar{\sigma}_{ij}$ used for the plasticity formulation is the average micro-level stress acting on the undamaged material skeleton. Thus, it is different from the nominal stress σ_{ij} calculated based on the nominal area (i.e., the cross section of a damaged body) containing meso-scale cracks. Since the remaining skeleton is intact, the effective stress $\bar{\sigma}_{ij}$ can be expressed as:

$$\bar{\sigma}_{ij} = \bar{E}_{ijkl} \, \bar{\varepsilon}_{kl} \tag{3.10}$$

where $\bar{E}_{ijkl}$ is the effective modulus and $\bar{\varepsilon}_{kl}$ is the effective strain of the undamaged skeleton. The connection between the undamaged skeleton and the damaged body can be established based on the assumption of strain equivalence or strain energy equivalence. Here the strain equivalence hypothesis is adopted, which leads to

$$\varepsilon_{ij} = \varepsilon_{ij}^e + \varepsilon_{ij}^p = \bar{\varepsilon}_{ij} = \bar{\varepsilon}_{ij}^e + \bar{\varepsilon}_{ij}^p \tag{3.11}$$

where ε_{ij} is the nominal strain of the nominal area, and the superscripts e and p indicate the elastic and plastic components of the strain tensor, respectively. After cracking, the nominal stress can be described by the effective stress based on a damage law as follows [65]:

$$\sigma_{ij} = (1-\Phi)\bar{\sigma}_{ij} = (1-\Phi)\bar{E}_{ijkl}\varepsilon_{kl}^e \tag{3.12}$$

Usually an isotropic damage scalar is used for Φ. However, if spectral decomposition is employed to separate tension and compression, the damage scalar Φ can be decomposed into Φ^+ and Φ^- to account for the anisotropic damage under tension (+) and compression (-) respectively.

57

In this model, the local uniqueness is guaranteed in the plasticity formulation by using the effective stress. Here the yield criterion follows the plastic yield surface f proposed by Lubliner et al. [66]

$$f = \sqrt{3\bar{J}_2} + \alpha\bar{I}_1 + \beta(\kappa^{\pm})H(\hat{\bar{\sigma}}_{max})\hat{\bar{\sigma}}_{max} - (1-\alpha)c^-(\varepsilon_{eq}^-) \leq 0 \qquad (3.13)$$

where $\bar{J}_2$ is the 2nd-invariant of the effective devitoric stress; $\bar{I}_1$ is the 1st-invariant of the effective stress; H is a Heaviside step function of the maximum principal effective stress $\hat{\sigma}$; β is a function of the equivalent tensile and compressive plastic strains $\kappa^{\pm}$; α is a dimensionless constant ranging from 0.08 to 0.14 for normal concrete [66]; and c^- is the compression cohesion dependent on the equivalent compressive strain ε_{eq}^-; $\hat{\bar{\sigma}}_{max}$ is the maximum principle effective stress; and $\kappa^{\pm} = \int_0^t \dot{\kappa}^{\pm}dt$ is the equivalent plastic strain, and is defined as:

$$\dot{\kappa}^+ = r(\hat{\bar{\sigma}}_{ij})\dot{\hat{\varepsilon}}_{max}^p \quad \dot{\kappa}^- = -(1 - r(\hat{\bar{\sigma}}_{ij}))\dot{\hat{\varepsilon}}_{min}^p \qquad (3.14)$$

where the dimensionless parameter $r(\hat{\bar{\sigma}}_{ij})$ is a weight factor depending on the principle stresses and is defined as:

$$r(\hat{\bar{\sigma}}_{ij}) = \frac{\sum_{k=1}^{3} <\hat{\bar{\sigma}}_k>}{\sum_{k=1}^{3} \left|\hat{\bar{\sigma}}_k\right|} \qquad (3.15)$$

where $<\cdot>$ is the Macauley bracket (i.e., $<x> = \frac{1}{2}(|x| + x)$).

The parameter α in Eq. (3.13) is a dimensionless constant given by Lubliner et.al. [66] and is within 0.08-0.14. The parameter β in Eq. (3.13) is given as:

$$\beta(\kappa^{\pm}) = (1-\alpha)\frac{c^-(\kappa^-)}{c^+(\kappa^+)} - (1+\alpha) \qquad (3.16)$$

where the cohesion parameters, $c^+(\kappa^+)$ and $c^-(\kappa^-)$, are given as:

$$c^+(\kappa^+) = f_0^+ + h\kappa^+$$

(3.17)

$$c^-(\kappa^-) = f_0^- + Q\,[1 - \exp(-\omega\kappa^-)]$$

where Q and ω are material constants characterizing the saturated stress and the rate of saturation respectively; h is a material constant obtained from the uniaxial tensile stress-strain diagram; and f_0^+ and f_0^- are the yield stresses for uniaxial tension and compression, respectively.

The non-associative plasticity flow rule is generally utilized to determine the shape of the concrete loading surface at any given loading state. The flow rule connects the loading surface and the stress-strain relation. When the current yield surface f is reached, the material is considered to be loading. In this model, the flow rule is given as a function of the effective stress $\bar{\sigma}_{ij}$ by:

$$\dot{\varepsilon}_{ij}^P = \dot{\lambda}_P \frac{\partial F^P}{\partial \bar{\sigma}_{ij}}$$

(3.18)

where $\dot{\lambda}_P$ is known as the plastic loading factor or known as the Lagrangian plasticity multiplier, which can be obtained by the plasticity consistency condition, $f = 0$, such that

$$f \le 0,\ \dot{\lambda}_P \ge 0, \quad \dot{\lambda}_P f = 0, \quad \dot{\lambda}_P \dot{f} = 0$$

(3.19)

By using the Drucker-Prager function, the plastic potential F^P can be expressed as:

$$F^P = \sqrt{3\bar{J}_2} + \alpha^P \bar{I}_1$$

(3.20)

where α^P is the dilation constant. Then the plastic flow direction is given by:

$$\frac{\partial F^P}{\partial \bar{\sigma}_{ij}} = \frac{3}{2} \frac{\bar{S}_{ij}}{\sqrt{3\bar{J}_2}} + a^P \delta_{ij} \qquad (3.21)$$

Tao and Phillps [67] defined the damage surface $g^{\pm}$ as a function of the damage thermodynamic conjugate force $Y^{\pm}$ and the scalar damage parameter $\Phi^{\pm}$ of a form similar to that of La Borderie et. al. [68]:

$$g^{\pm} = Y^{\pm} - Y_0^{\pm} - Z^{\pm} \le 0 \qquad (3.22)$$

where $Y_0^{\pm}$ are the initial damage thresholds which govern the onset of tensile and compressive damage respectively.

As damage progresses, the initial damage surface changes according to the evolution laws defined by the hardening/softening parameters $Z^{\pm}$. Tao and Phillips [67] assumed that the softening of damage surface followed a power law, in the form of:

$$Z^{\pm} = \frac{1}{a^{\pm}} \left(\frac{\Phi^{\pm}}{1 - \Phi^{\pm}} \right)^{\frac{1}{b^{\pm}}} \qquad (3.23)$$

A stress point in the principal stress space can be either within or on the current damage surface. Once it is on the damage surface, two possible damage states exist. One may be unloading or neutral loading ($\dot{\Phi}^{\pm} = 0$). The other is loading, accompanied with the evolution of damage, and is defined as $\dot{\Phi}^{\pm} > 0$. Mathematically, the above description can be expressed as:

$$\text{If } g^{\pm} < 0, \quad \text{then } \dot{\Phi}^{\pm} = 0$$

$$\text{If } g^{\pm} = 0 \text{ and } \dot{g}^{\pm} \le 0, \quad \text{then } \dot{\Phi}^{\pm} = 0 \qquad (3.24)$$

$$\text{If } g^{\pm} = 0 \text{ and } \dot{g}^{\pm} > 0, \quad \text{then } \dot{\Phi}^{\pm} > 0$$

The Helmholtz free energy can be formed by a series of internal state variables characterizing the elastic, plastic and damage behaviors of concrete. The constitutive model here

is based on the hypothesis of uncoupled elasticity. This hypothesis assumes that the total free energy density per unit volume is formed by the two independent parts: the elastic part and the plastic part. Therefore, the Helmholtz free energy of concrete is:

$$\psi = \psi^e(\varepsilon_{ij}^e, \Phi^+, \Phi^-) + \psi^p(\kappa^+, \kappa^-) \tag{3.25}$$

It is assumed that the damage only affects the elastic one rather than the plastic one. Taking time derivative of the Helmholtz free energy, we get:

$$\dot{\psi} = \dot{\psi}^e + \dot{\psi}^p = \frac{\partial \psi^e}{\partial \varepsilon_{ij}^e} \dot{\varepsilon}_{ij}^e + \frac{\partial \psi^e}{\partial \Phi^+} \dot{\Phi}^+ + \frac{\partial \psi^e}{\partial \Phi^-} \dot{\Phi}^- + \frac{\partial \psi^p}{\partial \kappa^+} \dot{\kappa}^+ + \frac{\partial \psi^p}{\partial \kappa^-} \dot{\kappa}^- \tag{3.26}$$

For isothermal behavior, the second-law of thermodynamics states that the rate of change in the internal energy is less than or equal to the external expenditure of power, which leads:

$$(\sigma_{ij} \dot{\varepsilon}_{ij} - \rho \dot{\psi}) \geq 0 \tag{3.27}$$

By substituting the rate of the Helmholtz free energy density described in Eq. (3.25) into the Clausius-Duhem inequality (Eq. (3.27)), we can get:

$$\sigma_{ij} \dot{\varepsilon}_{ij}^p + (\sigma_{ij} - \rho \frac{\partial \psi^e}{\partial \varepsilon_{ij}^e}) \dot{\varepsilon}_{ij}^e - \rho \frac{\partial \psi^e}{\partial \Phi^+} \dot{\Phi}^+ - \rho \frac{\partial \psi^e}{\partial \Phi^-} \dot{\Phi}^- - \rho \frac{\partial \psi^p}{\partial \kappa^+} \dot{\kappa}^+ - \rho \frac{\partial \psi^p}{\partial \kappa^-} \dot{\kappa}^- \geq 0 \tag{3.28}$$

The above equation is valid for any admissible internal state variable such that the Cauchy stress is defined as: $\sigma_{ij} = \rho \frac{\partial \psi^e}{\partial \varepsilon_{ij}^e}$. Eq. (3.28) can be written as:

$$\sigma_{ij} \dot{\varepsilon}_{ij}^p + Y^+ \dot{\Phi}^+ + Y^- \dot{\Phi}^- - c^+ \dot{\kappa}^+ - c^- \dot{\kappa}^- \geq 0 \tag{3.29}$$

with the damage conjugate force $Y^\pm$ and plasticity conjugate force $c^\pm$ being:

$$Y^\pm = -\rho \frac{\partial \psi^e}{\partial \Phi^\pm} \tag{3.30}$$

$$c^{\pm} = \rho \frac{\partial \psi^{p}}{\partial \kappa^{\pm}} \tag{3.31}$$

Based on the thermodynamic framework, one can obtain the expression for the damage thermodynamic conjugate forces $Y^{\pm}$:

$$Y^{\pm} = -\rho \frac{\partial \psi^{e}}{\partial \Phi^{\pm}} = \frac{1}{2} \frac{\left\| \bar{\sigma}_{ij}^{\pm} \right\|}{\left\| \bar{\sigma}_{ij} \right\|} \{ \varepsilon_{ij}^{e} \bar{E}_{ijkl} \varepsilon_{kl}^{e} - \frac{1}{9}(1-\beta)(\varepsilon_{mm}^{e})^{2} \delta_{ij} \bar{E}_{ijkl} \delta_{kl} \} \tag{3.32}$$

with the damage reduction factor:

$$\beta = 1 - \frac{1}{1 + cY \exp(-d \cdot Y)} \tag{3.33}$$

where c and d can be regarded as two material constants to make β dimensionless.

3.4 UNIFIED CONSTITUTIVE MODEL FOR CONCRETE

To achieve a unified description of the viscoelasticity, plasticity and fracture of concrete, models formulated based on the series coupling of a viscoelastic model and a damage model are frequently mentioned in literature [69]-[71]. In these models, the creep strain and cracking strain are calculated separately by using the same nominal stress increment and then added together. Although this type of formulation is straightforward and effective, its integration into a general-purpose FEM program (e.g., ABAQUS) is inconvenient because the series coupling requires iterations to achieve the same nominal stress increment in the two coupled models. Therefore, a different strategy is used in this thesis.

In Figure 3.2, the proposed unified constitutive model is demonstrated. Based on this one-dimensional illustration, the total strain ε_{ij} in concrete is

$$\varepsilon_{ij} = (\varepsilon_{ij}^{e} + \varepsilon_{ij}^{''}) + \varepsilon_{ij}^{p} + \varepsilon_{ij}^{cc} + \varepsilon_{ij}^{sh} \tag{3.34}$$

here the term $(\varepsilon_{ij}^{e} + \varepsilon_{ij}^{''})$ represents the viscoelastic strain of the Kelvin units. To utilize the quasi-

elastic stress-strain incremental relation of Eq. (1.43), the cyclic creep strain ε_{ij}^{cc}, plastic strain

ε_{ij}^{p} and shrinkage strain ε_{ij}^{sh} should be removed from the total nominal strain.
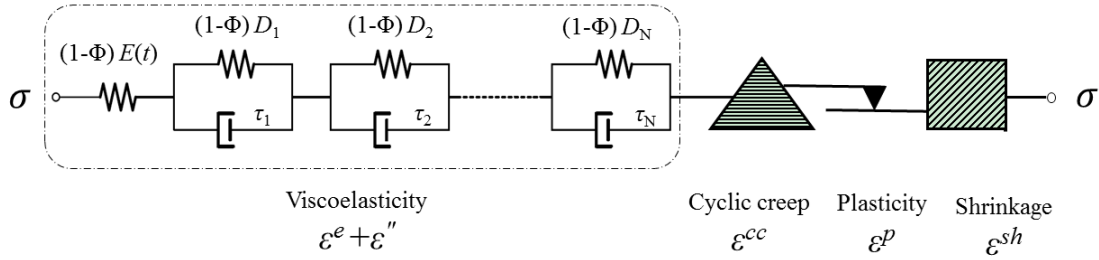
Figure 3.2. 1D illustration of the proposed unified concrete model.

In this formulation, the static creep is assumed to happen only on the undamaged

skeleton, not on the cracked body. This is rational and consistent with creep experiments where

stress much lower than the compressive cracking threshold of concrete is generally used. Thus

the creep strain calculation, similar to the plastic strain, is based on the effective stress $\bar{\sigma}_{ij}$, not

the nominal stress σ_{ij}.

To couple the concrete damage with the rheological model, now a damage scalar Φ is

homogeneously applied to the modulus of each Kelvin unit when the nominal stress of concrete

is calculated. This means the effective modulus obtained in Eq. (1.44) is adjusted based on the

damage evolution given in Eq. (3.22), and thus can be used to calculate the nominal stress shown in Eq. (3.12).

Both ε_{ij}^{cc} and ε_{ij}^{sh} are calculated separately and then input to Eq. (3.34) like eigenstrains. Since Eq. (3.6) is built upon the small fatigue growth of pre-existing microcracks [47] and no strength loss is observed in cyclic creep tests [58], it may be a realistic approximation to assume that the cyclic creep happens only on the undamaged skeleton too. Therefore, simple elastic analysis on intact concrete can be used to attain the average stress σ and the variation amplitude $\Delta\sigma$, for which the influence lines of different types of vehicles have to be exploited.

3.5   FRAMEWORK OF IMPLEMENTATION

In addition to the coupling of different physical processes, another advantage of the proposed unified constitutive model is that it can be embedded as a user subroutine into a general-purpose FEM program. This provides great convenience in modelling, visualization and post-processing, and thus is preferred in creep structural analysis. The general-purpose program ABAQUS is used; the flowchart of the implementation is presented in Figure 3.3.
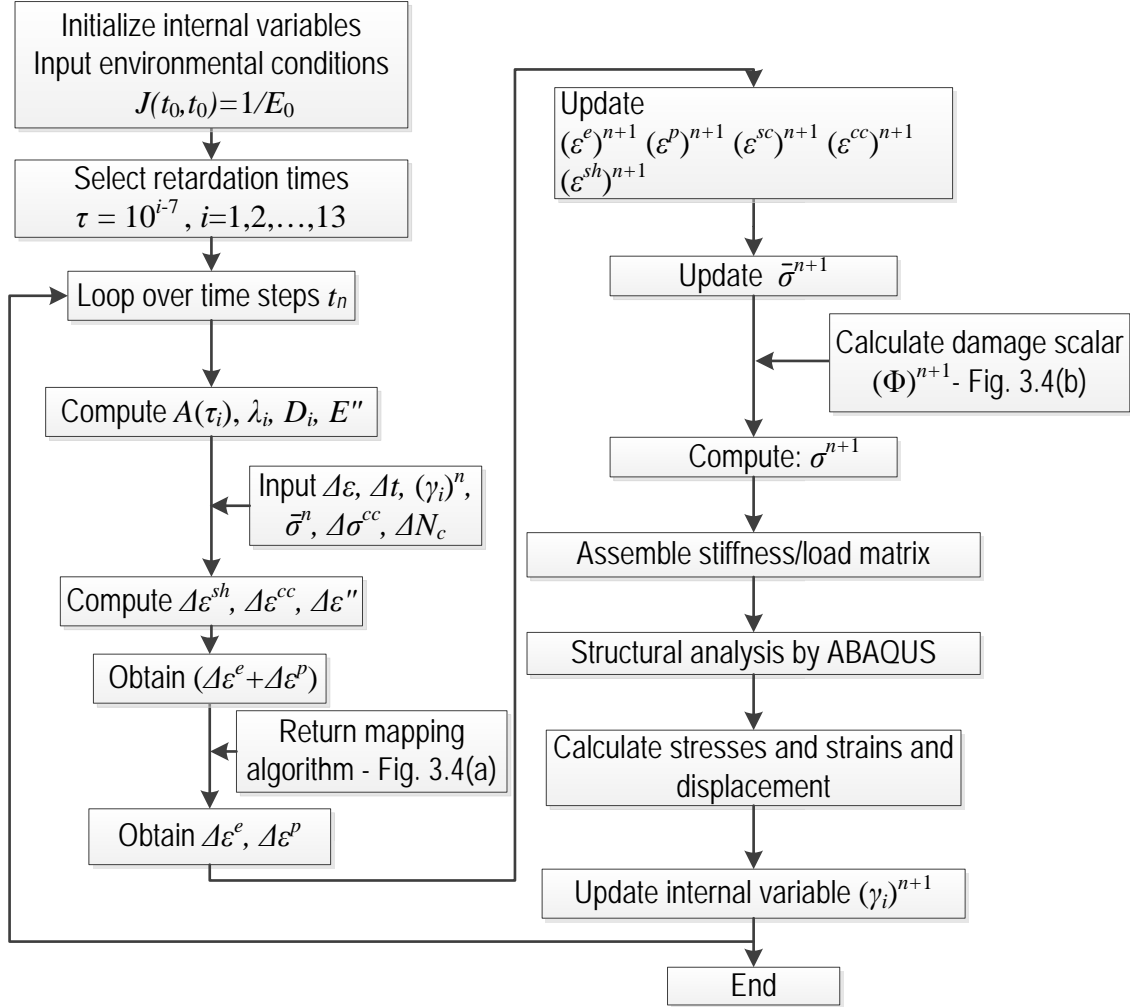
Figure 3.3. Flowchart illustrating the numerical implementation of the proposed unified concrete model in ABAQUS.

At the initiation of the current time step, the total strain increment $\Delta\varepsilon$ is provided by ABAQUS. To obtain the unknown $\Delta\varepsilon^e$ and $\Delta\varepsilon^p$, a return mapping algorithm [72] based on the Newton-Raphson iteration is used here; see Figure 3.4(a). By utilizing the relation between the plastic deformation ε^p and effective stress $\bar{\sigma}$, which is determined by the elastic strain ε^e, this algorithm achieves convergence in less than 10 iterations. After all strain components are determined, the damage scalar for the current time step is calculated (Figure 3.4(b)), and the

corresponding nominal stress σ and effective modulus $(1-\Phi)E''$ of concrete are obtained and then returned to ABAQUS for assembling the global stiffness/load matrix.

$$\bar{\sigma}^n,\ (\varepsilon^e)^n,\ (\varepsilon^p)^n,\ (\kappa^{\pm})^n,\ (\phi^{\pm})^n$$

strain increment $(\varDelta\varepsilon^e+\varDelta\varepsilon^p)$

$$\sigma^{trial} = \bar{\sigma}^n + E\cdot(\varDelta\varepsilon^e+\varDelta\varepsilon^p),\ \varDelta\lambda^p =0$$

$$f(\sigma^{trial}) < 0 \qquad \text{Yes}$$

No

Update $\varDelta\lambda^p=\varDelta\lambda^p+f^{trail}/H$

Calculate $\varDelta\varepsilon^p,\ (\kappa^{\pm})$
Update $\sigma^{trial} =\sigma^{trial}- E\cdot\varDelta\varepsilon^p$
Update hardening functions $c^+\ c^-$

No

Convergence of $f(\sigma^{trial}) = 0$

$$\bar{\sigma}^{n+1} =\sigma^{trial}$$
$$(\varepsilon^p)^{n+1} = (\varepsilon^p)^n$$
$$(\varepsilon^e)^{n+1} = (\varepsilon^e)^n + (\varDelta\varepsilon^e+\varDelta\varepsilon^p)$$

Yes

Update $\bar{\sigma}^{n+1} =\sigma^{trial}$

(a)

Input $(\varepsilon^e)^{n+1}$, $\bar{\sigma}^{n+1}$

Compute $(Y^{\pm})^{n+1}$

Evaluate $g^{\pm}((Y^{\pm})^{n+1}, (\Phi^{\pm})^n) < 0$

No

Update $(\Phi^{\pm})^{n+1}$ Using $(Y^{\pm})^{n+1}$

Yes

$(\Phi)^{n+1} = (\Phi)^n$

Update $(\Phi)^{n+1}$

$(\Phi)^{n+1}$
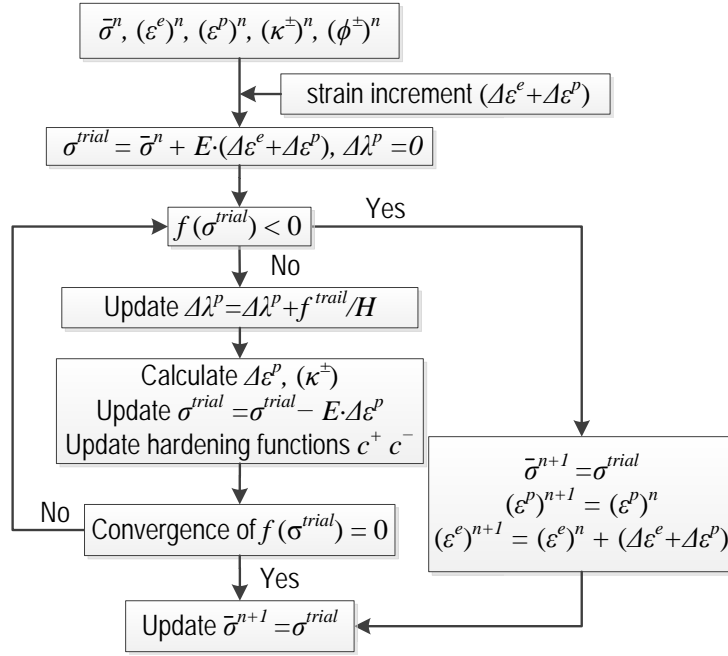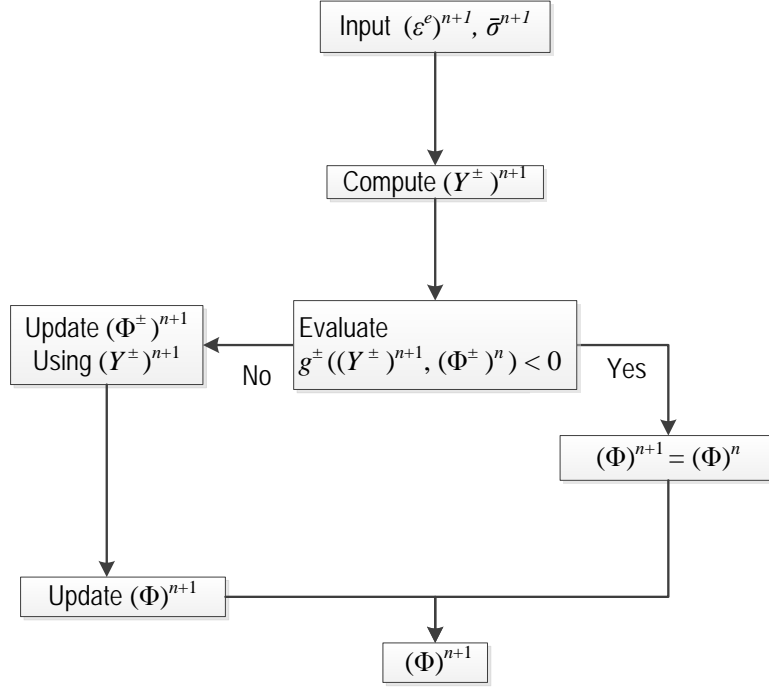
(b)

Figure 3.4. (a) Return mapping algorithm for the plastic softening and (b) subroutine for the damage variable calculation.

To validate the model and test its implementation in ABAQUS, virtual experiments are carried out before the case study of a real bridge. A standard 150 mm cube made of C55 concrete [73], which is identical to the concrete used in the case study, is modelled (Figure 3.5(a)). Based on the strength of concrete, material constants for the elasto-plastic damage model recommended in [62] are adjusted, through which the stress-strain curve of C55 concrete for uniaxial compression and tension can be captured in Figure 3.5(a). These material constants are listed in Table 3.1. Following the general practice [39], the virtual mix design gives the water to cement ratio ($w/c = 0.28$), aggregate to cement ratio ($a/c = 3.8$), and cement content ($c = 520.0$ kg/m^3). Therefore, the material parameters for the viscoelastic model, which adopts *fib* (2010) model

(denoted as MC model in this chapter) and model B4, can be evaluated according to Chapters 1.2.3 and 1.2.4, respectively.

Table 3.1. The material constants for elasto-plastic damage model

Parameter	Value	Parameter	Value
$f_{cu,m}$	63.2×10^6 Pa	f_0^-	20.0×10^6 Pa
μ	0.18	Q	50.0×10^9 Pa
E	34500×10^6 Pa	b	2200
α	0.12	Y_0^+	156 Pa
α^P	0.20	Y_0^-	400 Pa
f_0^+	3.48×10^6 Pa	a^+	3.3×10^{-3} Pa^{-1}
h	25.0×10^9 Pa	a^-	8.4×10^{-6} Pa^{-1}
c	2.0 Pa-1	b^+	1.20
d	0.7 Pa-1	b^-	0.98

Figure 3.5(a) shows the simulation results of the cube under uniaxial tension and compression. The corresponding damage evolution is plotted in Figure 3.5(b). Failure under tension and the softening under compression captured in the virtual tests agree with the typical responses of normal concrete (e.g., the average cube strength of C55 concrete is about 63 MPa and the ratio of tensile strength to compression strength is about 1/14) [27]. Similarly, virtual creep tests are carried out on the same concrete cube. Two service stress levels, i.e., 10 and 15 MPa, are applied to the concrete cube respectively. Figure 3.5(c) shows the corresponding creep

curves obtained based on the B4 and MC models, respectively. It can be seen that the linearity and asymptote of static creep are both realistically reproduced by the proposed framework.

If the sustained stress in concrete is much higher than the service level, concrete will fail within a certain period of time due to the nonlinear creep and fracture growth. This phenomenon is called creep failure [74]. Although creep failure rarely happens in prestressed concrete bridges, it is used here to test the coupling of concrete static creep and damage in the proposed constitutive model. Experiments conducted by Zhou [74] at Lund University are simulated and the material parameters of the model are adjusted based on the experimental report. The notched concrete beams are under 3-point bending with sustained loads of 92%, 85%, 80% and 76% of the maximum load capacity, respectively (Figure 3.5(d)). If creep failure occurs, the beam cannot support the sustained load and the numerical simulation cannot reach convergence. The results of creep failure simulations are plotted in Figure 3.5(d), where the trend observed in Zhou's test [74] is realistically reproduced by the proposed model.

(a)

(b)

69
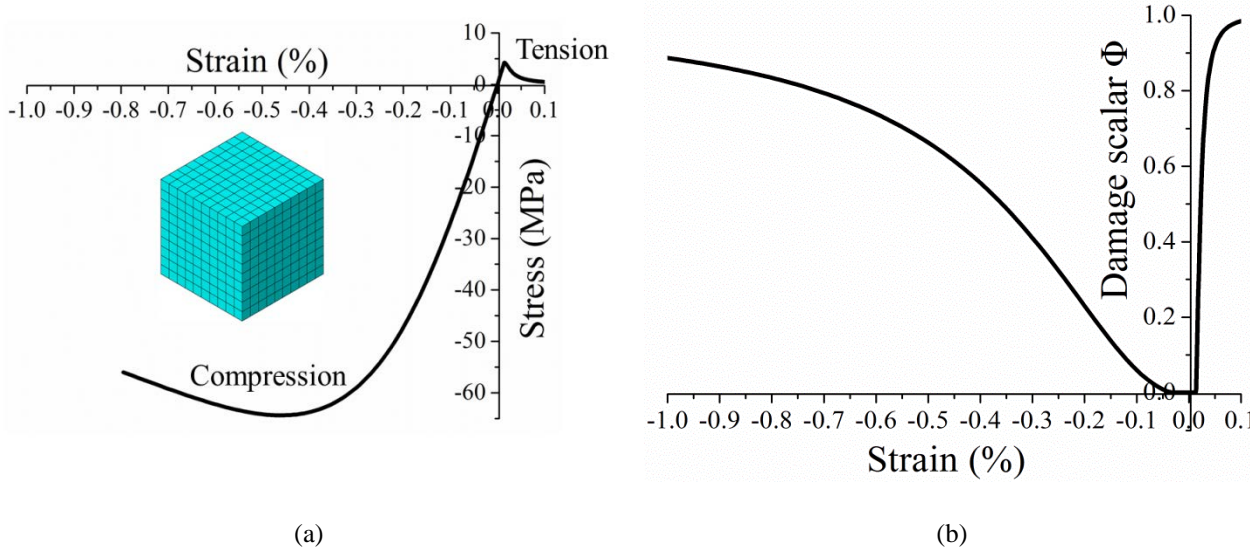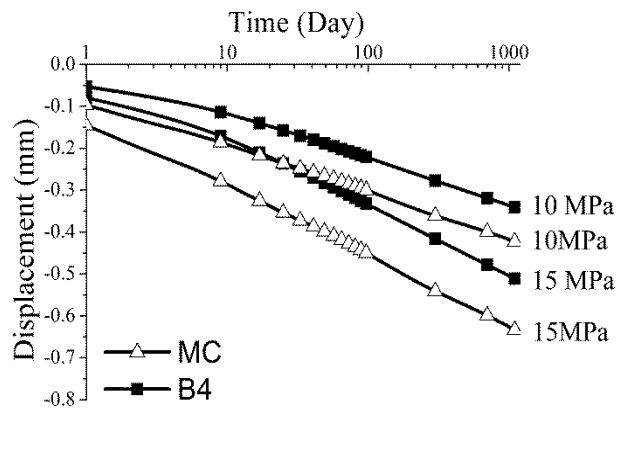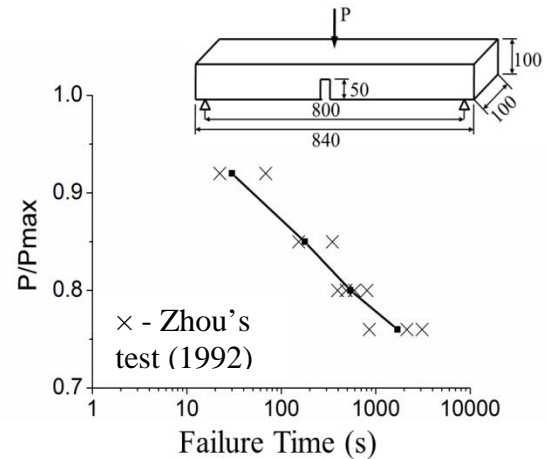
(c)   (d)

Figure 3.5. Validation of the implementation in ABAQUS: (a) stress-strain curve of a virtual concrete cube under uniaxial compression and tension; (b) corresponding damage evolution; (c) creep curves based on the MC and B4 models, respectively; and (d) simulated creep failure under different load levels using B4 model.

Another purpose of these virtual experiments is to regularize the localized damage, which cannot be objectively described by a local constitutive model. Without a localization limiter to regularize the fracture energy release, the structural response to cracking will be mesh-sensitive. A remedy to this problem will be the nonlocal formulation utilizing the weighted spatial average for the damage variables [75]-[77]. But it is currently difficult to implement the nonlocal formulation in ABAQUS. Therefore, another approach is used here. In line with the classical crack band theory [78], a mesh size-dependent parameter will be used to adjust the damage law in the proposed model [79]. Considering the compression in concrete is typically within the service range, this alternative is sufficient for the numerical analyses of large-span prestressed concrete bridges.

70

3.6   MODELING OF A LARGE-SPAN BRIDGE

The bridge under study is the Humen Bridge in Guangdong Province, China. It consists of two adjacent identical but independent bridges (I and II), which carry vehicles travelling in opposite directions respectively (Figure 3.6(a)). The busy traffic flow containing a considerable number of heavy trucks makes the Humen Bridge a unique case to study the intertwined effects of static creep, cyclic creep and concrete cracking and softening.

This 3-span prestressed concrete bridge was erected segmentally and the continuous main span (270m long) set the world record for prestressed box girders when the construction was completed in 1997; see Figure 3.6(a). Following a quadratic parabolic curve, the height of the box girders decreases from 14.8 m at the piers to 5.0 m at midspan (Figure 3.6(b)). Similarly, the thickness of bottom slab and webs changes from 1.3 m and 0.6 m at the piers to 0.32 m and 0.4 m at the midspan respectively. The thickness of the top slab is constant along the traffic direction (Figure 3.6(b)).

For bridge I, the main span (consisting of 63 segments) and the two side spans (consisting of 36 segments for each) are both erected sequentially by 94 prestressing tendon groups (ASTM A416-94 [80]), among which 66 groups are used to prestress the top slab and the remainder in the bottom slab. In addition, to enhance the shear resistance, threaded bars (diameter = 32 mm) are installed vertically to prestress the webs with a spacing of 1 m. The distribution of prestressing tendons and threaded bars for bridge I is plotted in Figure 3.6(c).

(a)

(b)
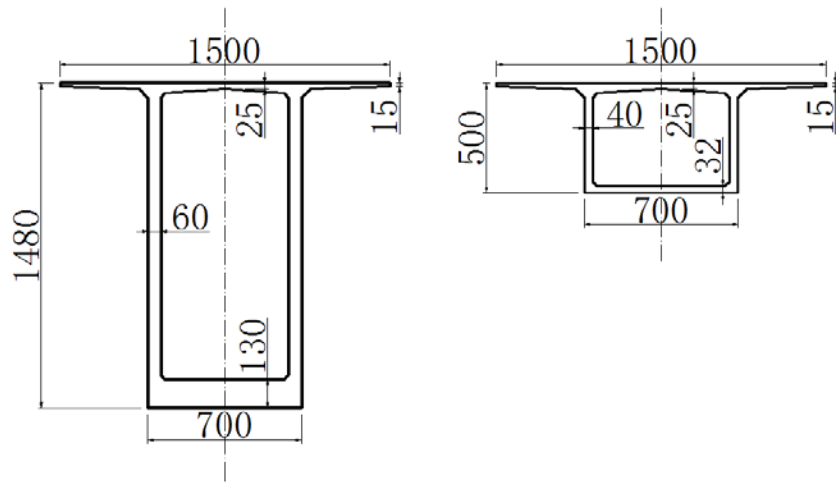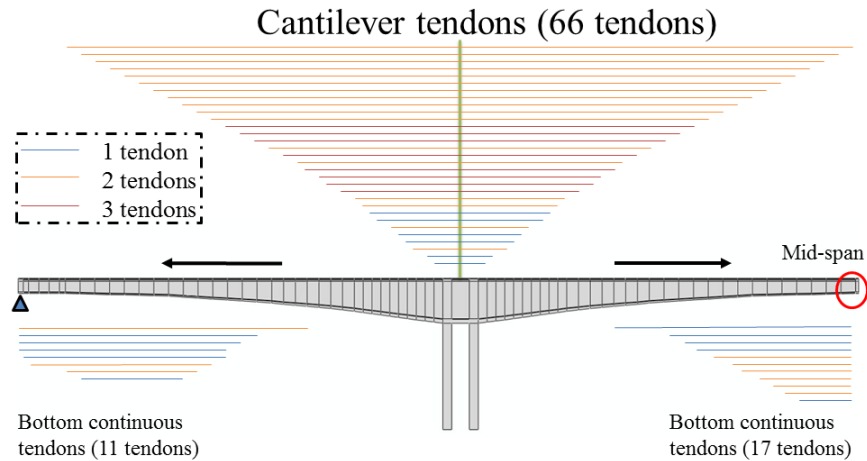
Figure 3.6. The Humen Bridge: (a) the bridges I and II (Unit: m); (b) cross-sections of box girders at the piers and midspan (unit: cm); and (c) the tendon layout for bridge I.

Based on the information provided by the available drawings [73], a 3D model of bridge I was built in ABAQUS (Figure 3.7(a)). Since prestressing tendons or threaded bars exist in all slabs, the top slab, bottom slab and webs are all meshed with 2 layers along the thickness direction so as to accommodate the prestressing tendons and bars at the middle. In this model, concrete is meshed by 3D hexahedral isoparametric elements (Figure 3.7(a)), and the tendons with 3D truss elements (Figure 3.7(b)) with the nodes perfectly bonded with the concrete elements. As for the mild steel, it is smeared into concrete due to its extremely low percentage and quasi-uniform distribution.

Since the tendons are almost straight, the curvature friction is negligible and only the wobble friction is considered. For each group of tendons, the prestress is applied 7 days after the

anchoring segments are cast. The initial prestress level for tendons is 1080 MPa and for screw-threaded bars is 400 MPa. The final layout of the prestressing tendons and bars in the model is shown in Figure 3.7(b).

To approximate the balanced construction process, which leads to a complex loading history in the concrete and tendons, the segments are deactivated at first in the simulations and then progressively activated based on the construction sequence provided in the drawings. In order to focus on the post-construction behavior, which is recorded in the inspection reports, the camber generated during the segmental construction will not be considered in the deflection analysis.
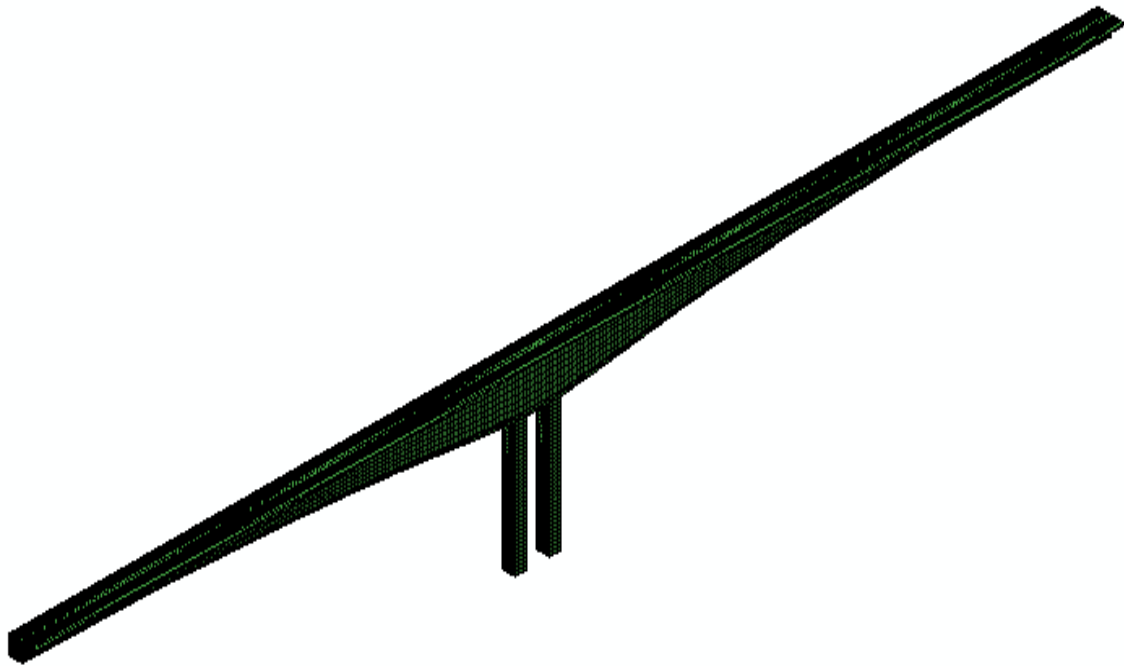
(a)
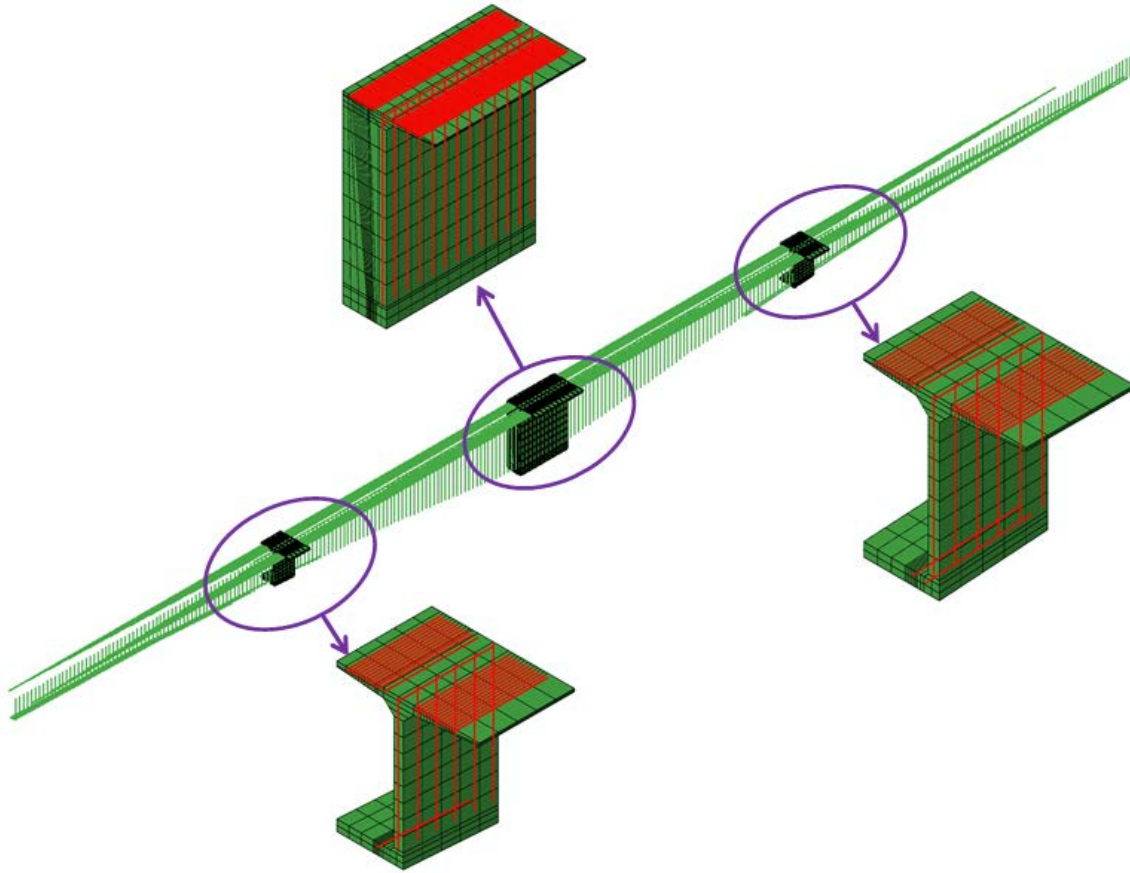
(b)

Figure 3.7. (a) Modelling of Humen bridge, and (b) modeling of prestressing tendons and threaded bars.

As a critical link connecting Guangdong Province and Hong Kong, the Humen Bridge is among the busiest traffic flows in the world. Based on the record of the highway toll system installed in this bridge, the annual traffic flow on the Humen Bridge is documented in Figure 3.8. It grew from 6,381,541 vehicles in 1998 to 22,994,003 vehicles in 2008 [73]. The vehicles are categorized by weight into six groups (

Table 3.2), whose proportions in the traffic flow are also recorded by the toll system. The pie chart in Figure 3.8 shows the composition of the traffic flow recorded in 2002. Based on the record of the toll system, it is assumed that the traffic volumes and compositions on these two

bridges are similar. The annual traffic flow and average weight of each vehicle type used for simulation are listed in Table 3.2.
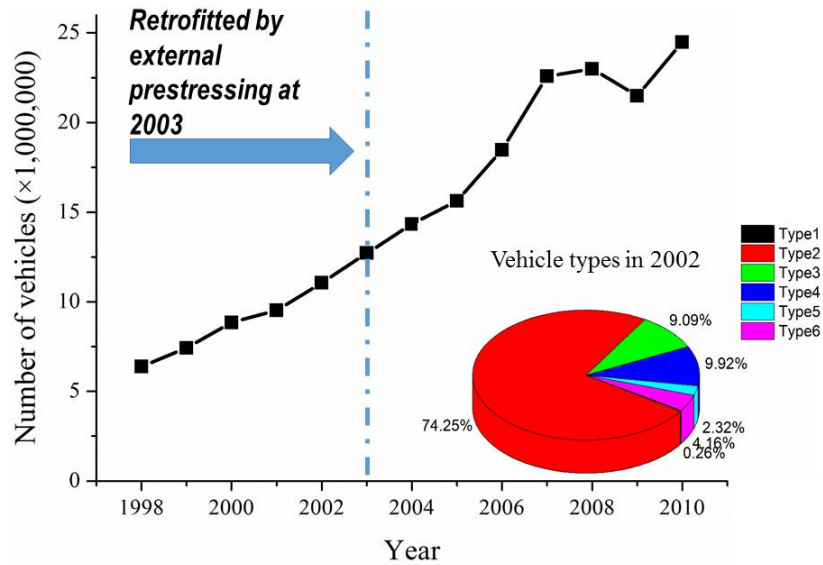
Figure 3.8. The records of annual traffic flow on the Humen Bridge and its composition in 2002.

Table 3.2. The annual traffic flow and average weight of each vehicle type [73].

	Weight (Ton)	Average weight (Ton)	Annual traffic flow					
			1998	1999	2000	2001	2002	2003
Type I	-	-	-	-	-	-	-	-
Type II	0 ~ 2	1	4407805	5303888	6453875	7074112	8206501	8152148
Type III	2~ 5	3.5	957902	984534	1086003	1024960	1004673	1546715
Type IV	5~ 8	6.5	368171	499203	653313	799117	1096677	255937
Type V	8~ 20	14	242644	240844	257730	237732	255937	387985
Type VI	> 20	38	196872	303862	319146	344340	460140	380974

3.7   SIMULATION AND RESULTS

To demonstrate the coupled effects induced by cyclic creep and concrete cracking, two types of simulations are run in this chapter. In the first type of simulations, the effects of concrete plasticity, damage and cyclic creep are not considered. This means the subroutines shown in Figure 3.3 and Figure 3.4 to account for these effects will be deactivated in the numerical analysis. Thus, only the static creep and shrinkage of concrete and steel relaxation will play a role in the time-dependent deflection. While, in the second type of simulations these effects will be considered and the subroutines will be activated. To compare these two types of simulations, the same intrinsic and extrinsic parameters, including the material parameters of concrete and steel, temperature, humidity, construction sequence, curing time before prestressing and traffic loads, are used.

In this investigation, the static creep of concrete, as well as concrete shrinkage, is approximated by the B4 and MC models. For both models, their intrinsic parameters need to be determined based on the concrete properties. Although the compressive strength is known for the C55 concrete used in the Humen Bridge, the composition of this concrete is not provided. Therefore, a virtual mix design, which achieves the given compressive strength, is used to obtain the composition parameters.

As for the relevant extrinsic parameters, the average humidity h is selected to be 70% and average temperature T is 20°C based on the bridge location. The construction sequence follows the drawings and the curing time before prestressing is set as 7 days. For the prestressing tendons, a bilinear law characterized by the Young's modulus $E = 200$ GPa and yield strength f_y = 1674 MPa is employed. For the threaded bars, the yield strength f_y in the bilinear law is changed to 785 MPa. After yield, the stiffness for prestressing prestressing tendons and threaded

bars is assumed zero. The relaxation parameters of prestressing tendons and bars are selected based on the CEB code formula [28]. To take into account the effect of strain variation (e.g., the shortening of the side spans), an improved relaxation formula utilizing a viscoplastic constitutive relation [20] is used in the simulation.

For traffic loads, a simplified cyclic shape with constant amplitude is used; see Figure 3.1(b). Since there are two lanes on bridge I, the cyclic shape depends on the vehicle weight as well as the ways of the vehicles to use these two lanes. The average weight used for each type of vehicles can be found in

Table 3.2, where the effect of Type I vehicles, standing for motorcycles, is not considered due to the negligible effect of motocycles on the stress fluctuation. Based on the traffic record, a traffic pattern (Pattern I) illustrated in Figure 3.9 is used to approximate the complex traffic flow on bridge I. In this pattern, vehicles in the same group drive on the lanes side by side, except that 95% of the trucks (Type VI) pass the bridge one by one. Based on the average weight in

Table 3.2 the influence lines of different types of vehicles are obtained, and the cyclic shape is subsequently determined according to Eq. (3.8).
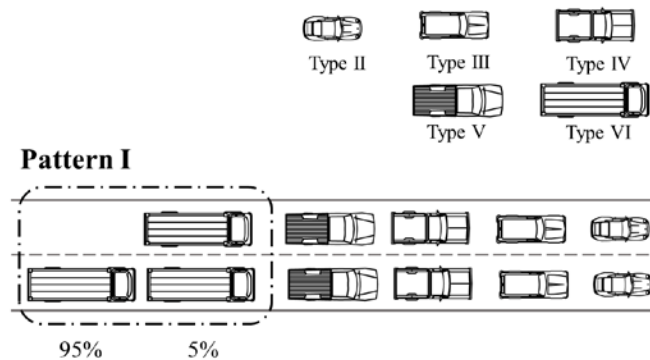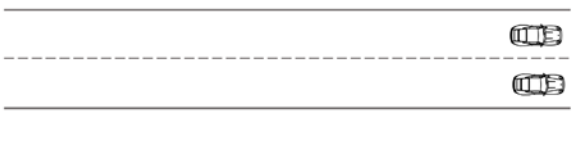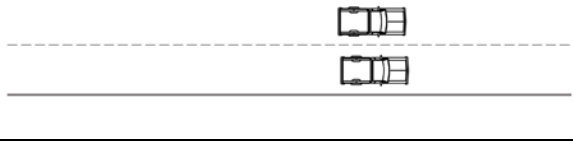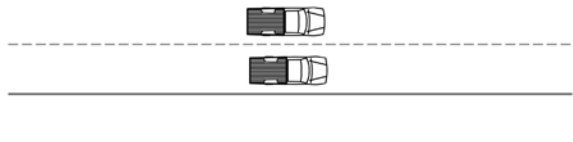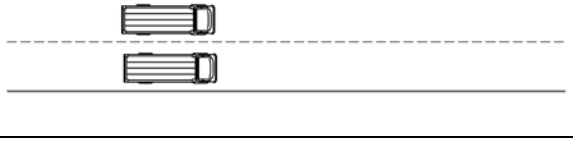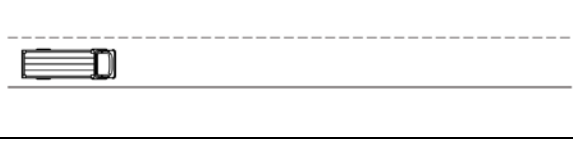
Figure 3.9. Approximate traffic flow (Pattern I) on the bridge I of the Humen Bridge.

For example, the total vehicles passing bridge I and bridge II are about 11 million in 2003. For Bridge I, the vehicles of Type II, III, IV, V and VI are 4076074, 773358, 127968, 193992, and 190487, respectively. Based on the traffic Pattern I in Figure 3.9, the cycles N_c of Type II vehicles are 2038037, and the vehicles drive on the lanes side by side. The cycles for other types of vehicles in 2003 are presented in Table 3.3. The range of stress variation $\Delta\sigma$ caused by the different vehicle type, for both top and bottom slabs, are also shown in Table 3.3.

Table 3.3. Cycles for traffic Pattern I of the year 2003.

Vehicle		Cycles (N_c)	$\Delta\sigma$ (MPa)
Type II		2038037	Top: 0.01~0.10 Bottom: 0.01~0.16
Type III		386679	Top: 0.02~0.20 Bottom: 0.03~0.35
Type IV		63984	Top: 0.03~0.36 Bottom: 0.05~0.64
Type V		96996	Top: 0.07~0.12 Bottom: 0.80~1.39
Type VI		4762	Top: 0.20~2.36 Bottom: 0.34~4.09
		180963	Top: 0.10~1.18 Bottom: 0.17~2.05

The traffic loads will induce fluctuations in both the normal and shear stress in concrete. An approach to treat this complexity is to calculate the variations of the principal stresses, based on which Eq. (3.6) is applied to determine the cyclic strains in the corresponding principal directions. The calculation can be further simplified by taking advantage of the stress distribution in a box girder section, in which the normal stress is mainly carried by the top and bottom slabs and the shear stress is mainly supported by the webs. For the traffic Pattern I, the ratios of the average stress variation $\overline{\Delta\sigma}$ obtained using Eq. (3.8) to the concrete strength f'_c, of the webs, top and bottom slabs, are listed in Appendix. A (Table A.1). These values vary from 0.003 to 0.013 in the top slab, and 0.001 to 0.005 in the bottom slab.

Using the recommended parameters listed in Table 3.1, numerical analysis of bridge I is carried out. The midspan deflection history in the first six years is obtained by the first type of simulations and plotted in Figure 3.10 in both linear and logarithmic time scales, the latter highlighting the asymptotical slope of the deflection curve.

(a)

80
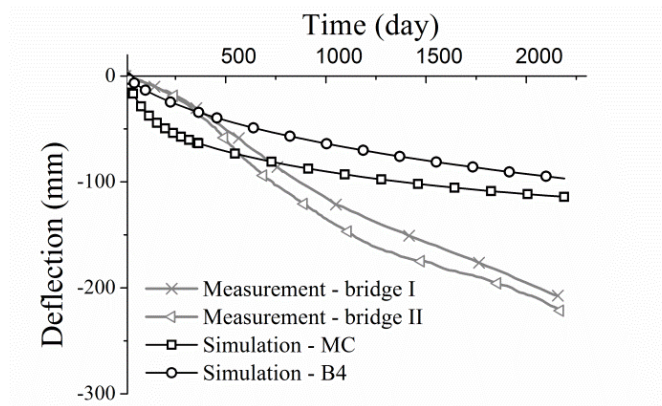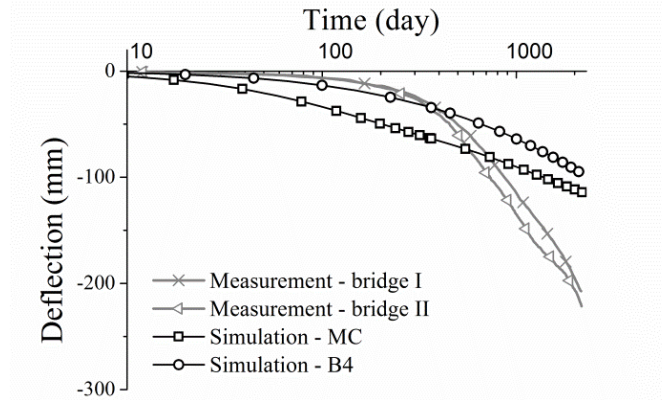
(b)

Figure 3.10. Comparison of the midspan deflection between the measurements and simulations without considering the coupled effects of cyclic creep and concrete cracking: (a) linear time scale, and (b) logarithmic time scale.

The measured midspan deflections of bridges I and II are also plotted in Figure 3.10 for comparison. It can be seen that after only six years in service the midspan deflection reaches 210 - 220 mm, exceeding 1/1300 of the length of main span. This unexpected deflection triggered a retrofit in 2003, which changed the structural form of the Humen Bridge. Since the information about this retrofit is not available, the bridge performance after 2003 is not simulated.

When compared to the in-situ measurements, the first type of simulations significantly underestimates the midspan deflection (Figure 3.10). For both the B4 and MC models, the predicted midspan deflections before retrofit are only about 100 mm, less than 50% of the measurements. In addition, the shape of the predicted deflection history substantially differs from the measured deflection history. The asymptotical slopes of B4 and MC models in logarithmic time scale, based on which the long-term creep growth may be estimated, are much less than those of the measured curves. Furthermore, since concrete damage is not considered, no concrete cracking is reported in the simulations.

81

In the second type of simulations, the plasticity, damage and cyclic creep in the unified model are all activated. The predicted midspan deflections are plotted in Figure 3.11 to compare with the measurements in both linear and logarithmic time scales. It can be seen that the prediction is significantly improved after the coupled effects are considered. Based on the MC and B4 models, the midspan deflections after six years in service are 237 and 224 mm respectively, which are close to the measurements (Figure 3.11). Except for the early-age development estimated by the MC model, the shape of the predicted deflection curves agrees well with the measured ones. In Figure 3.11, both models exhibit asymptotical slopes similar to the in-situ measurements.
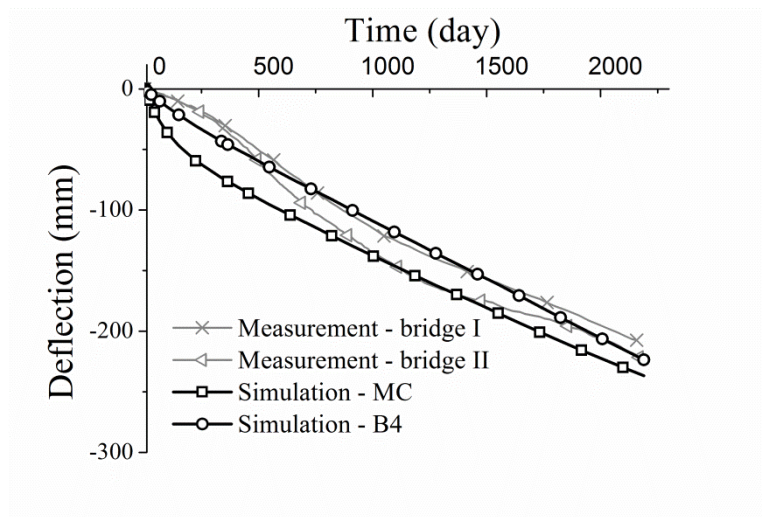
(a)
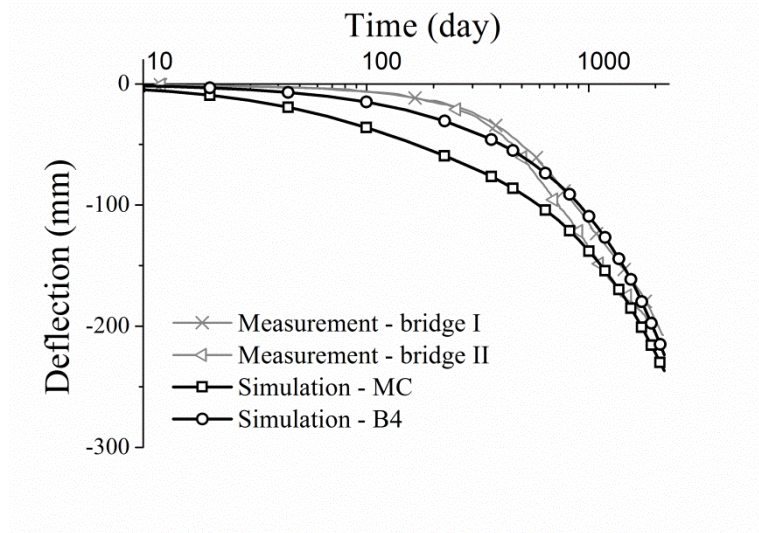
(b)

Figure 3.11. Comparison of the midspan deflection between the measurements and simulations considering the coupled effects of cyclic creep and concrete cracking: (a) linear time scale, and (b) logarithmic time scale.

In addition to the deflection of midspan, the deformed profiles of the bridge are also estimated in the second type of simulations. The measured profiles of bridges I and II after two, three, four and five years in service are plotted in Figure 3.12. It can be seen that after taking into account the intertwined effects of plasticity, damage and cyclic creep, the proposed unified constitutive model reproduces the deformed profiles realistically in the second type of simulations. This means that the proposed unified framework is capable of approximating the global time-dependent response of Humen Bridge.
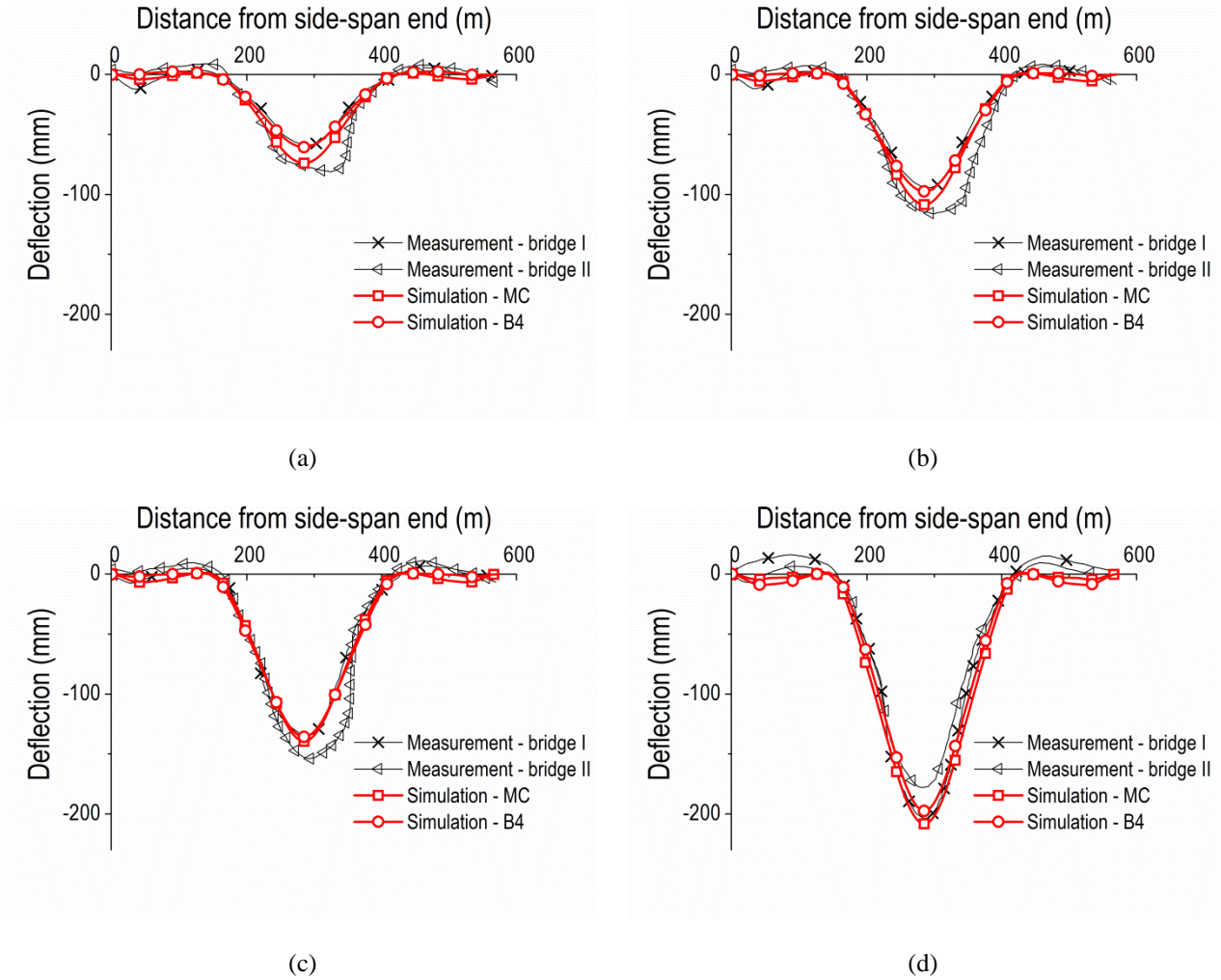
Figure 3.12. Comparison of the deformed bridge profile between the measurements and simulations considering the coupled effects of cyclic creep and concrete cracking: (a) 2 years; (b) 3 years; (c) 4 years; and (d) 5 years after construction.

Based on the inspection report [73], a number of cracks are found in the segments close to the midspan six years after construction (Figure 3.13(a)). The cracks initiate in the bottom slab and then propagate gradually to the webs [73]. For some segments located around the ¼ span, minor skewed cracks are recorded on the top portion of webs (Figure 3.13(a)). For segments near the piers, no visible cracks are reported in the inspection.

84

In the second type of simulations, the damage scalar Φ is used to indicate the extent of concrete cracking. The development of cracking in concrete captured in the simulations is demonstrated in Figure 3.13(b). The simulations show that initially there is almost no concrete cracking along the bridge after construction. After one-year service, cracking is developed in some segments (Figure 3.13(b)). Since the cracking is minor (i.e., the damage scalar $\Phi < 0.1$), it can be ignored. After four years, cracking grows around the midspan ($\Phi < 0.23$). At the end of the sixth year, severe cracking is developed in the bottom slab close to the midspan ($\Phi < 0.86$), and some of the cracks penetrate into the webs (Figure 3.13(b)). In some segments around the ¼ span, mild cracking (i.e., $\Phi < 0.15$) in the top portion of webs is captured after six years' service. For the segments at the piers, the concrete is in good condition (i.e., $\Phi \approx 0$). Clearly, the cracking distribution in concrete shown in Figure 3.13(b) agrees well with the inspection report [73].

The results of the two types of simulations show that the static creep alone is inadequate for estimating the time-dependent deformation of prestressed concrete girders carrying heavy traffic flows. The neglect of cyclic creep and concrete cracking may lead to significant underestimation of the long-term deflection growth and inaccurate prediction of the damage development. This is very different from bridges carrying light or mild traffic flows. For example, the extensive study [47] on the Palau Bridge determined that the light traffic load on this large-span bridge (about 200 cars per day) had a negligible effect on the deflection evolution and damage development.

(a)

(b)
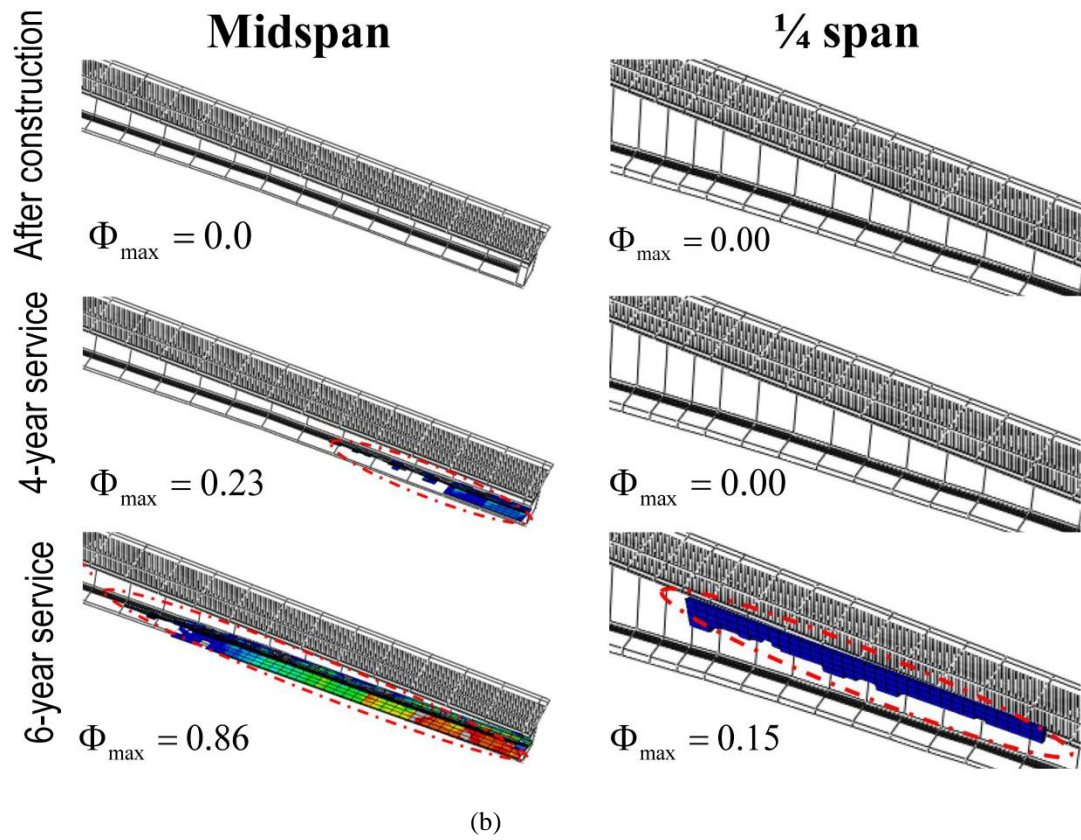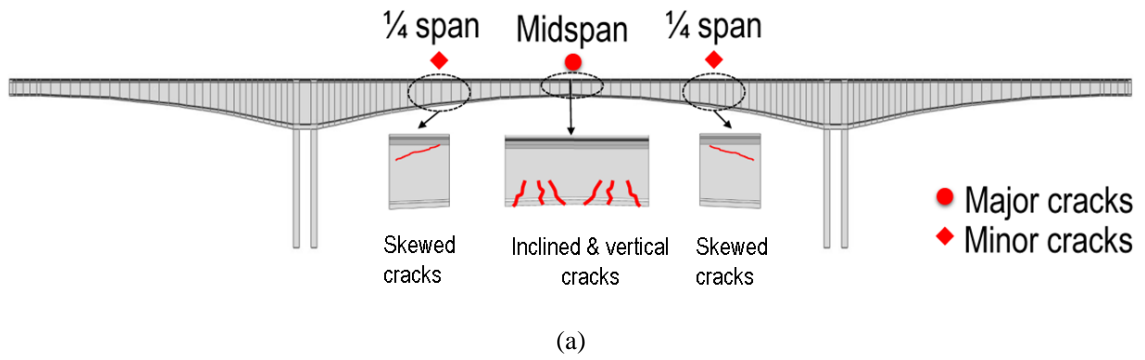
Figure 3.13. (a) Crack distribution recorded in the inspection report, and (b) simulated damage distribution at different ages using B4 model.

3.8   INFLUENCE OF TRAFFIC WEIGHT AND VOLUME

The cyclic creep of concrete, which is found to be non-negligible for the damage accumulation and deflection growth in the Humen Bridge, is governed by the time shape of cyclic load [47]. Due to the random passage of vehicles, the correlation of concrete cyclic creep with traffic weight and flow is very complex. Thus, simplified traffic patterns must be used in creep structural analysis. To ensure that the traffic Pattern I shown in Figure 3.9 is an acceptable simplification, a qualitative exploration focused on the sensitivity of cyclic creep to traffic pattern is carried out.

In addition to Pattern I shown in Figure 3.9, five more simplified traffic patterns are studied (Figure 3.14). In Pattern II, all the vehicles pass the bridge one by one, randomly on either of the two lanes. This simplistic traffic pattern is highly possible for the heavy trucks but not realistic for the cars on a busy bridge. To approximate the traffic flow of cars, except for certain types of vehicles, side-by-side driving is allowed in Patterns III and IV, in which vehicles from the same group drive in pairs on the bridge. This is different from the real traffic flow, in which different types of cars may occupy adjacent lanes. However, the pairing strategy used in Patterns III and IV can maximize the amplitude of stress variation induced by the heavier vehicles, and thus give more conservative predictions of the cyclic creep. To probe the effect of heavy vehicles, trucks driving in pairs on the lanes are increased to 10% in the Pattern V and to 50% in the Pattern VI. Pattern VI is very unlikely to occur in a bridge equipped with toll systems; it is used here to illustrate the extreme scenarios that may be triggered by heavy trucks. For the traffic Patterns II, III, IV, V and VI, the ratios of the average stress variation $\overline{\Delta\sigma}$ obtained using Eq. (3.8) to the concrete strength f_c', of the webs, top and bottom slabs, are listed in Appendix. A

87

(from Table A.2 to Table A.6), respectively. Clearly, from traffic Pattern II to Pattern VI, the maximum ratio increases from 0.018 to 0.031, which is affected by the random passage of vehicles.
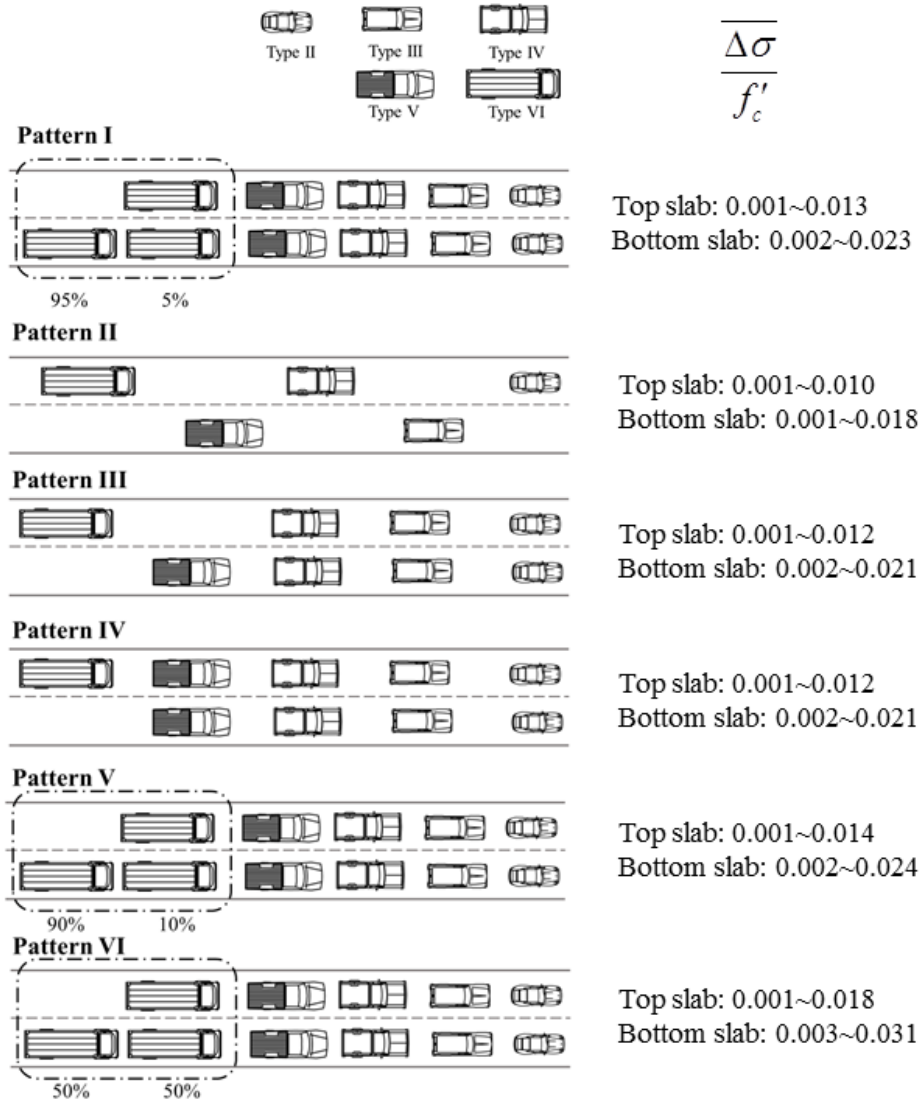
Figure 3.14. Six traffic patterns on the bridge I of the Humen Bridge.

Here only B4 model is used for the unified framework because it performs better than the MC model in predicting the early-age development of midspan deflection (see Figure 3.11). The simulation results based on the respective traffic patterns are plotted in Figure 3.15 to compare with the measured deflections. It can be seen that the deflection curves based on the Patterns I-V give good approximations of the real measurements. The difference among the Patterns II-IV is negligible because the predicted deflections are almost same (~200 mm). This means that the bridge deflection is insensitive to the traffic pattern of cars less than 10 tons. The deflection growth induced by the cyclic creep primarily depends on the total number of cars travelling through the bridge.
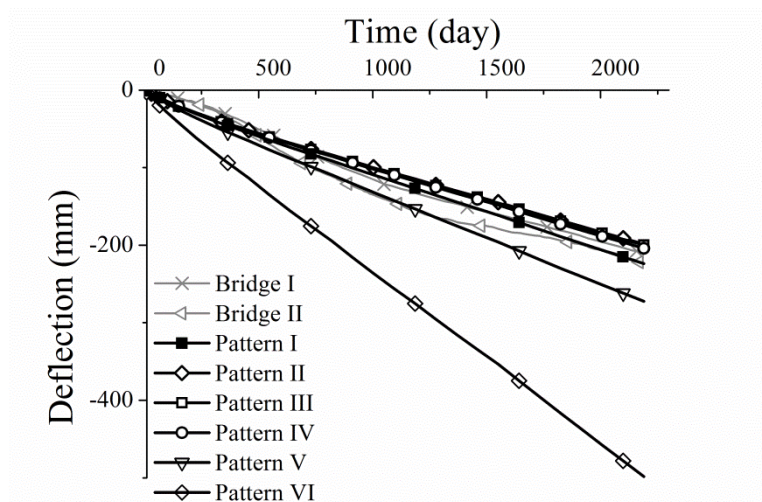
(a)
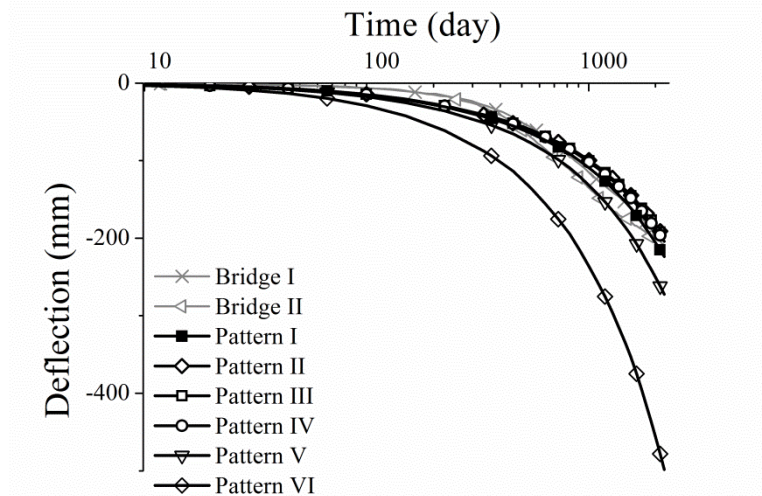
(b)

Figure 3.15. Comparison of the midspan deflection between the measurements and simulations under different traffic patterns: (a) linear time scale and (b) logarithmic time scale.

If heavy trucks are allowed to pass in pairs, the influence of traffic pattern on deflection development becomes non-negligible. When 5% of the trucks drive side by side on the lanes (the Pattern I), the deflection gains a minor increase and the final deflection grows to 224 mm. This change coincides with the deflection difference between bridges I and II; see the gray lines in Figure 3.10. When the proportion of paired trucks rises to 10% (the Pattern V), the final deflection will reach 272 mm, beyond the measured deflections. However, if trucks follow Pattern VI, a striking increase in deflection will appear and the final deflection will surprisingly approach 500 mm.

Although unrealistic, the excessive deflection exhibited by Pattern VI is consistent with experimental results. In cyclic creep tests [81][82], it was found that when the average stress and stress amplitude were about 25% and 10% of the concrete compressive strength respectively, the cyclic creep of concrete under cyclic compression reached about 2.3 times the elastic

90

deformation after only 100,000 cycles. The cyclic shape based on traffic Pattern VI, which is not realistic for heavy trucks, displays a stress fluctuation of 4.0 MPa. Therefore, the cyclic creep and bridge deflection predicted by this pattern are reasonable.

The numerical investigation shows that the bridge deflection is insensitive to the traffic pattern of lightweight vehicles and the simplified traffic Pattern I (Figure 3.9) used in the simulations is acceptable. It also implies that the traffic pattern of heavy trucks may contribute to the deflection difference between bridges I and II, which have identical structure and carry similar traffic loads. The greater deflection measured in bridge II may be attributed to a higher percentage of paired trucks on it. Of course, this is just a conjecture based on the simulations. The possibility that other sources (e.g., the material and construction randomness) triggered this deflection difference cannot be excluded.

To mitigate the risk of excessive deflection, the trucks travelling on the bridge need to be managed. A prudent traffic management plan, which can be implemented in some bridges, is to assign only one lane to the trucks. To make it more effective, the assigned lane may be alternated after a period (e.g., 3 years) so as to distribute the damage accumulation in concrete. Figure 3.16(a) shows two hypothetic traffic management plans, one assigning a fixed lane to the trucks (Plan A) and the other alternating the truck lane every 3 years (Plan B). To compare these two plans, the respective traffic flows are applied in the numerical investigation. The deflection developments predicted by the simulations corresponding to these two plans are shown in Figure 3.16 (b), respectively. The simulated damage distribution in concrete is shown in Figure 3.16 (c) for Plan A and Figure 3.16 (d) for Plan B. It can be seen that both the deflection growth and damage development are slower if the truck lane is alternated (Figure 3.16 (b-d)).

(a)   (b)

(c)   (d)
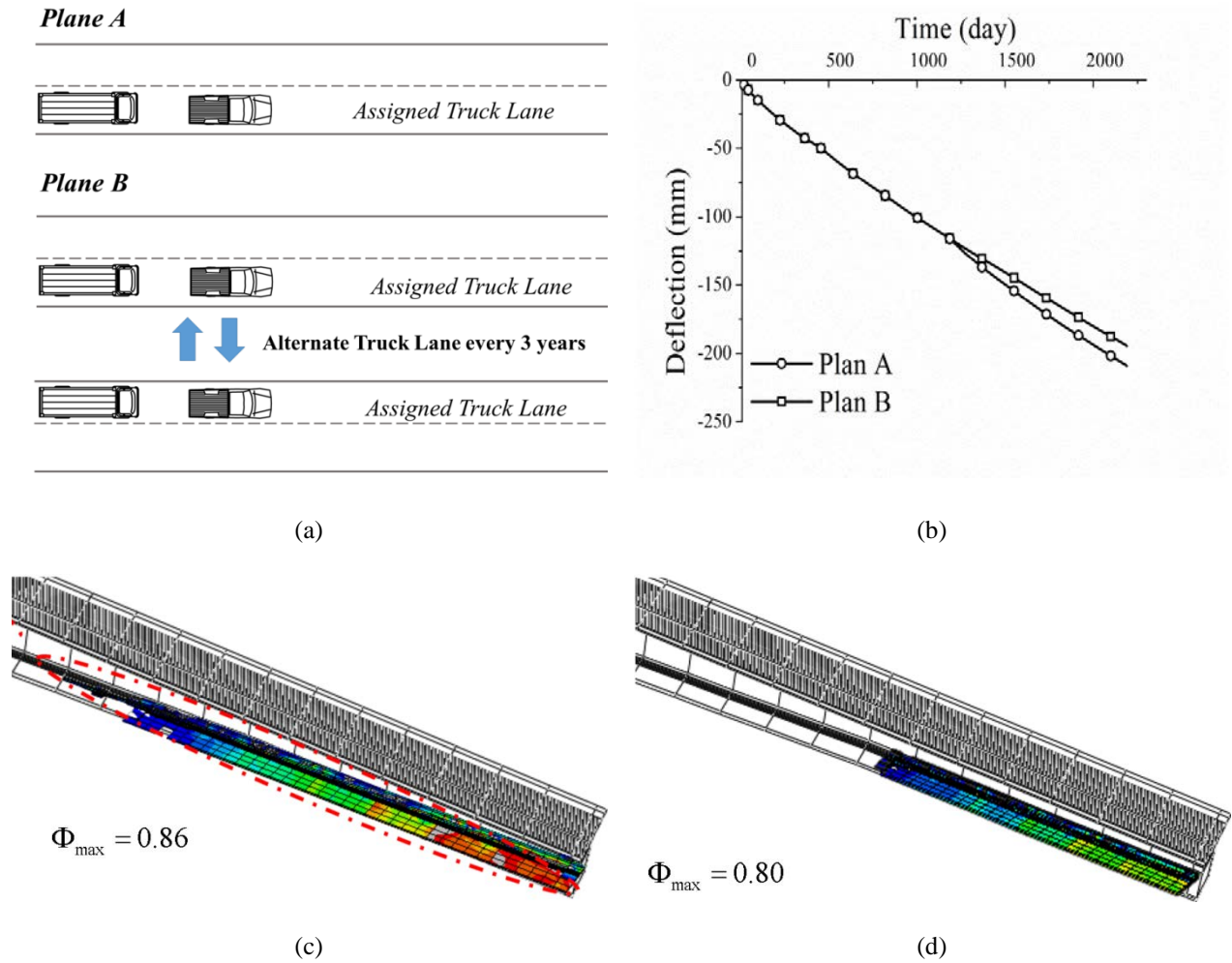
Figure 3.16. Comparison of the traffic management planes A and B: (a) illustration of lane assignment; (b) corresponding midspan deflections in linear time scale; (c) simulated damage distribution around the midspan for the plan A; and (d) simulated damage distribution around the midspan for the plan B.

3.9   SUMMARY

A unified constitutive model, coupling the static creep with the cyclic creep, damage and softening of concrete, is constructed and integrated into a 3D rate-type framework for creep structural analysis. The intertwined effects of concrete viscoelasticity, cracking and plastic

softening on the time-dependent deformation are investigated by a case study of a large-span prestressed concrete bridge carrying a heavy traffic flow. Based on the simulation results, the conclusions drawn from this study include:

1. To predict the multi-decade deflection of large-span prestressed concrete box girders, a realistic constitutive model is needed to approximate the complicatedly intertwined time-dependent processes in concrete. The proposed unified constitutive model, coupling the B4 (or MC) creep and shrinkage model with an elasto-plastic damage model and a fatigue mechanics-based cyclic creep model, is capable of describing the concrete viscoelastic behavior as well as the concrete responses under mild-level confinement.

2. As demonstrated in the case study of a large-span prestressed concrete bridge, the proposed numerical framework is efficient for large-scale creep structural analysis. The 3D rate-type formulation used in the framework provides the key assistance to couple the static creep with the cyclic creep, concrete cracking, and other processes, which may not be compatible with the integral-type formulation.

3. For large-span segmentally prestressed concrete bridges supporting heavy traffic flows, the case study of the Humen Bridge shows that viscoelastic analysis based on the static creep of concrete alone is not adequate. It provides limited information of concrete damage and may significantly underestimate the bridge deflection. To improve the predictive capacity of creep structural analysis, it is recommended that the intertwined effects of concrete cyclic creep and concrete cracking should be considered for bridges similar to the case study.

4. The cyclic creep of concrete for Humen Bridge is insensitive to the traffic pattern of vehicles less than 10 tons, because lightweight vehicles have lesser ratio of stress variation to concrete compressive strength, and hence have a little impact on cyclic creep strain. However,

93

the traffic pattern of heavy trucks cannot be ignored. The percentage of trucks driving in parallel with each other can significantly impact the bridge deflection development and stress redistribution in concrete.

5. To mitigate the coupled effects of concrete cyclic creep and crack propagation on the deformation growth in busy segmental bridges, besides the total traffic volume, the traffic pattern of heavy trucks needs to be managed. Traffic management plans assigning and alternating lanes for trucks can effectively mitigate the risk of excessive deflection and concrete cracking induced by the traffic loads. In addition, increasing the concrete strength may also aid in resisting the cyclic creep.

In this investigation, the performance of Hunmen Bridge is studied based on the deterministic simulations. The randomness induced by the intrinsic and extrinsic sources associated with the bridge behavior is not considered and its role in the bridge performance is not evaluated. Only the average trend of the intertwined effects of concrete viscoelasticity, softening and damage is qualitatively studied in the numerical analyses. Therefore, although the proposed model adequately captures the general trend of the bridge performance in the case study, for more accurate quantification of the deflection history, this inadequacy needs to be remedied in future by incorporating statistical analysis. After equipped with proper sampling strategies (e.g., Latin hypercube sampling), the proposed framework can be extended to statistically quantify and assess the coupled effects of different physical processes so as to provide more general and reliable prediction for the long-term performance of large-span prestressed concrete bridges. In addition, some of the conclusions derived in this chapter are based on the simulation of the Humen Bridge. Further investigations of more prestressed concrete bridges are required to validate these conclusions.

4.0   MULTISCALE TIME-DEPENDENT SIMULATIONS OF CONCRETE

4.1   MOTIVATION AND BACKGROUND

In Chapters 2 and 3, the parameters of different concrete creep models, including ACI (2008), CEB-FIP (1990), *fib* (2010) and B3/B4 models, are calibrated by macro-scale creep experiments. In these macroscopic formulations, concrete is treated as a homogenous material. However, concrete is a heterogeneous material composed of multiple phases. The macro-scale time-dependent mechanisms of cementitious materials are intrinsically governed by these phases at meso-, micro-, or even nano-scales. Multi-scale experiments and simulations of cementitious materials can offer more accurate insights to the mechanical, time-dependent, and transport behaviors of cementitious materials [23]-[25]. Although the numerical studies of concrete properties at different scales can provide more accurate results, it is prohibitively expensive to model concrete at micro-scale or nano-scale due to the limited computational capacity. Fortunately, meso-scale structure is accurate sufficiently to obtain the fundamental understanding of the mechanical and time-dependent mechanisms, which can be utilized in the macro-scale analysis [26]. At the meso-scale, concrete can be decomposed to mortar matrix, coarse aggregate, interface transition zone (ITZ) and air voids.

Generally two different approaches are adopted to generate models at the meso-scale for concrete. The first approach is based on the digital images of concrete meso-scale structures

95

obtained by microscopes or more advanced techniques [83]-[85]. These digital images are then converted into finite element meshes to model the multiple phases with real sizes, shapes and distributions. The image-based approach can realistically reflect the meso-scale structures of concrete but the cost is expensive. Thus, the image-based approach is not suitable for parameter study. The second approach is the parameterization modelling method, where the meso-scale structures of concrete are generated virtually by the computer [26]. More specifically, the indirect and direct algorithms can be used for the parameterization modelling method. Different phases are not explicitly modelled in the indirect algorithm. Instead, different phases inside the heterogeneous materials are modelled as spatially-varying random fields assigned to conventional FE meshes [24], or by lattice model in which lattice elements are randomly assigned as aggregates or mortar [86]. In the direct algorithm, coarse aggregates of different shapes are randomly packed into the space, and embedded within the mortar matrix to form the meso-scale structures of concrete. The direct algorithm can generate a large number of samples easily, and thus is suitable for parametric study.

Based on the parameterization modelling approach, this paper presents a study of mechanical and time-dependent behaviors of concrete at meso-scale. The conventional "taking" and "placing" procedure [87] is applied to randomly generate the meso-scale structure of concrete. Under a given grading curve of coarse aggregates, the circular, elliptical and polygonal coarse aggregates, and circular and elliptical air voids are considered in the numerical specimens. After the geometry of the numerical specimen is determined, the solid elements are used to mesh the concrete domain. After that, zero-thickness cohesive elements with different damage and softening behaviors are inserted between the meshed solid elements to capture the fracture and damage of mortar matrix and ITZ.

96

The uniaxial tensile and compressive behaviors are investigated for these numerical concrete specimens, using a displacement-control scheme. First, the maximum tensile and compressive loads for these numerical concrete specimens are obtained. After that, two different load levels, 20% and 60% of the maximum compressive load, are applied on the specimen to investigate creep-induced deformation, respectively.

In order to map the simulation result of meso-scale structure to the macro-scale behavior of concrete, two different approaches are utilized. The first approach adopts the framework of computational homogenization based on the Hill's stationary condition, whose computational cost is relatively high but can provide accurate results. The second approach is based on the theoretical solution of a matrix-inclusion problem, whose computational cost is inexpensive but is limited by the shape of the meso-scale structure.

4.2   MESO-STRUCTURE OF CONCRETE

The meso-scale structure of concrete is generally characterized by the phases of mortar matrix, coarse aggregate, ITZ and air void. At this length scale, the mortar matrix is simply treated as a homogeneous material. In this section, the meso-scale structure of concrete, in accordance with a given gradation of coarse aggregates, is constructed numerically. Different shapes of coarse aggregates (circular, elliptical and polygonal coarse aggregates) and different shapes of air voids (circular and elliptical air voids) are considered in the modelling. The typical "taking" and "placing" algorithm [26] is realized in MATLAB to generate and pack these particles in the given concrete domain. After the geometry of the meso-structure is determined, pre-processing functionalities in ABAQUS controlled by Python script are adopted to mesh the concrete domain

by solid elements. After that, the cohesive elements are inserted between each solid element to simulate the damage and failure behaviors of concrete.

Aggregates are generally divided into fine aggregate (sand) and coarse aggregate (i.e. gravel or crushed stone). The sum of coarse aggregates and fine aggregates can occupy up to 60~80 % volume of the normal concrete, of which 30~50% of the total volume of concrete is coarse aggregate. The fine aggregate is not explicitly considered at the meso-scale as it is embedded in the mortar matrix. Therefore, "aggregate" hereafter refers to the coarse aggregate only. The shape of aggregate depends on the aggregate type. Generally, gravel aggregate has a rounded shape while the crushed aggregate has an angular shape [87]. Gravel aggregate is assumed to have a circular or elliptical shape, while the convex polygonal shape is used to simulate the crushed aggregate.

Grading refers to the particle size distribution of aggregates, which is usually expressed as a cumulative percentage passing through a series of sieves of increasingly finer openings. The grading of coarse aggregates is often characterized by the Fuller curve, which generally leads to the optimum density and strength of concrete. The Fuller curve can be written as [24]:

$$P(d) = 100 \, (\frac{d}{d_{max}})^n \tag{4.1}$$

where $P(d)$ is the cumulative percentage passing a sieve with aperture diameter d, and d_{max} is the maximum size of aggregate particles and n is a constant ($n = 0.45\text{-}0.70$).

In practice, the Fuller curve can be replaced with a number of segments, where the area of aggregate A_{agg} within each grading segment $[d_i, d_{i+1}]$ can be expressed as [87]:

$$A_{agg}[d_{i+1}, d_i] = \frac{P(d_{i+1}) - P(d_i)}{P(d_{max}) - P(d_{min})} P_{agg} A \tag{4.2}$$

where $d_{\min}$ denotes the minimum size of aggregates; P_{agg} is the area fraction of aggregates; and A is the sample area of concrete.

In this study, a four-segment size distribution of coarse aggregates (Table 4.1 and Figure 4.1) is adopted [88]. Only coarse aggregates with a size greater than 2.36 mm, like gravels and crushed stones, are considered in the meso-scale model. Gravel aggregates having a circular or elliptical shape and curshed aggregates having a polygonal shape are modelled to investigate the effect of aggregate shape on the macro-scale behavior of concrete.

Voids and pores in concrete can be roughly divided into air voids, cappillary pores and gel pores [89]. The capillary and gel pores are too small (less that a few micrometers) and can be ignored at meso-scale [26]. The air voids have relatively larger size and are included in the meso-structure of concrete. The size of air voids, which is circular or elliptical, is uniformly distributed within the range from 2 to 4 mm [90].

Table 4.1. Four-segement gradation of aggregate size distribution

Sieve size (mm)	Total percentage passing (%)
19.00	100
12.70	97
9.50	61
4.75	10
2.36	1.4
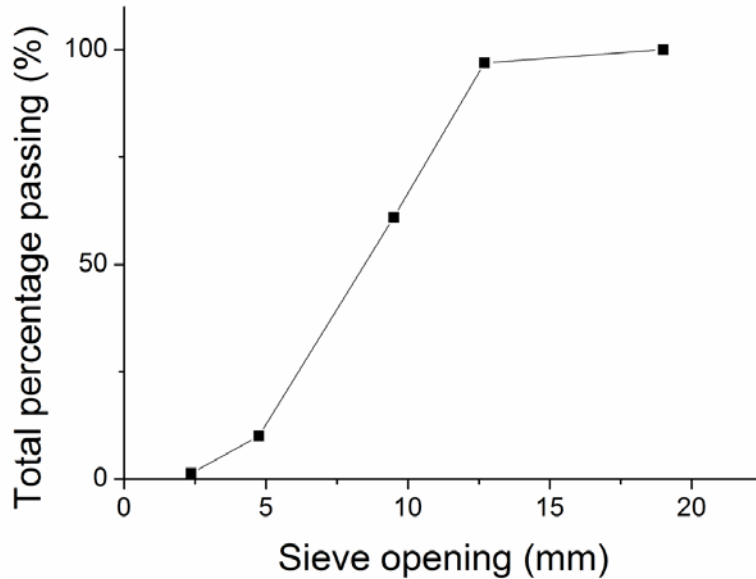
Figure 4.1. Aggregates size distribution.

After dividing the grading curve into several segments, the generation and packing of aggregates starts from the largest size particles. A typical "taking" and "placing" algorithm is utilized to generate and place the aggregates randomly in a 2D domain [87]. The "taking" and "placing" algorithm is implemented in MATLAB and the procedures are explained in detail as follows:

The "taking" process generates an individual aggregate or air void in accordance with the grading curve in Figure 4.1. The generation of aggregates and air voids is repeated until the target volume of aggregates and air voids is achieved for each grading segment.

1.   The areas for the aggregates in each grading segments $[d_i, d_{i+1}]$ and air voids are calculated.

2.   The generation of aggregates starts with the grading segment containing the largest aggregates. For different grading segments, one may assume a uniform distribution

between d_i and d_{i+1}. The aggregate size d is calculated by $d = d_i + \eta(d_{i+1} - d_i)$, where η is a random number between 0 and 1.

3. Calculate the area of the aggregate and subtract it from the total area for the grading segments $[d_i, d_{i+1}]$.

4. The generation of aggregate for this grading segment (Steps 2 and 3) is repeated until the area of aggregate to be generated is less than $\pi d_i / 4$, which means the remaining area for this grading curve is not enough to generate another aggregate. This remaining area is added to the next grading segment $[d_{i-1}, d_i]$.

5. Repeat Steps 2, 3 and 4 until the last particle of the smallest size of the grading segment is finished.

6. Assume that the size of air voids distributes uniformly between d_0 and d_1. The air void size is $d = d_0 + \eta(d_1 - d_0)$. The generation of air voids is repeated until the area of void to be generated is less than $\pi d_0 / 4$, indicating no extra space to place another air void.

The "placing" process inserts the aggregates and air voids into the predefined domain subjected to the prescribed physical constraints. First, the coarse aggregates are placed into the predefined domain. In order to save computational time, the insertion of aggregates begins from the large size to the small one. The aggregates with smaller size are then inserted between the larger aggregates to dense the domain. After positions for all aggregates are determined, then the air voids are inserted between these aggregates. Based on the "taking" and "placing" algorithm described here, Wang et.al [26] successfully created the meso-scale structures of concrete with 40% coarse aggregates and 2% air voids in volume. The meso-scale structures with 45%

polygonal coarse aggregates are also obtained in [87]. Therefore, this algorithm is utilized in this chapter.

In order to place the aggregates and air voids randomly within the concrete domain, two physical constraints need to be satisfied. First, all aggregates and air voids should be within the concrete domain. Second, the newly inserted aggregate or air void must not have any overlap with the previously placed aggregates and air voids. In addition to these two constraints, the third physical constraint requires that each aggregate should be coated with a mortar film of a certain minimum thickness. The minimum thickness of the mortar film is thought to be related to the particle size and aggregate content. Schlangen and Mier proposed [91] that the minimum thickness was $0.1(d_a + d_b)/2$, where d_a and d_b are the sizes of the two aggregates. Two constant values, the minimum distance γ_1 between the aggregate/void and specimen boundary and the minimum distance γ_2 between the newly inserted aggregate/void and the existed aggregate/void, are utilized.

Random numbers are generated to define the position of the aggregates and air voids. If any of these three physical constraints is violated, this newly inserted aggregate/void is disregarded and another random number is generated to place the same aggregate/void in another position. Otherwise, the position for this aggregate/void is accepted. Using the above "taking" and "placing" algorithm, concrete specimens with different shapes and sizes of aggregates and air voids can be obtained. In this chapter, γ_1 and γ_2 are set as 0.5 mm. The aspect ratio $R = [2, 2.5]$ is adopted for elliptical aggregates and air voids. The number of sides for the convex polygons is set as $N = [4, 7]$ for the crushed aggregates, which means the number of sides for the convex polygons randomly varies from 4 to 7. Some numerical samples of generated meso-scale

structures for concrete with different shapes and contents of aggregates and air voids are illustrated in Figure 4.2-Figure 4.4.

<div align="center">(a)   (b)   (c)</div>
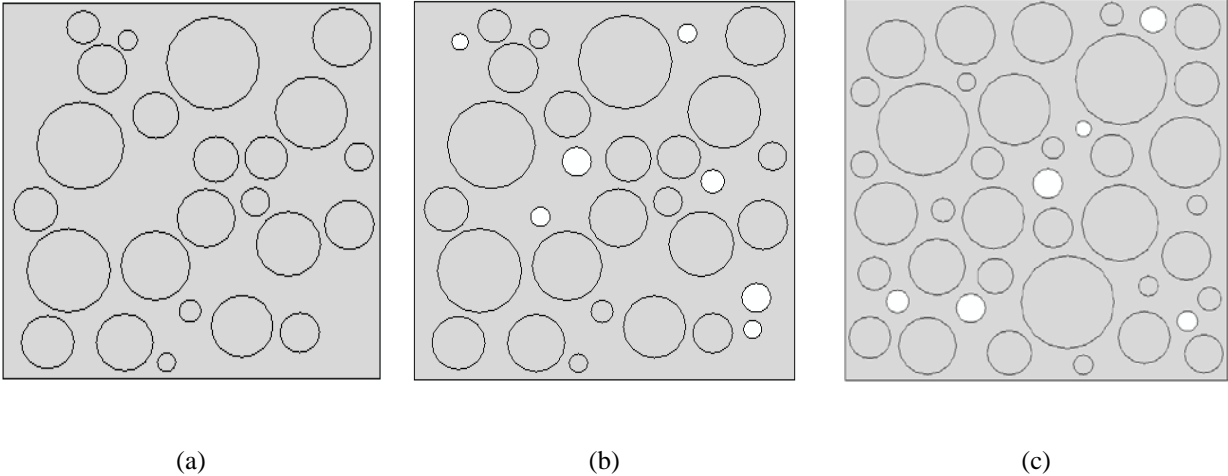
Figure 4.2. Numerical samples with circular aggregates: (a) P_{void}=0%, P_{agg}=40%; (b) P_{void}=2%, P_{agg}=40%; and (c) P_{void}=2%, P_{agg}=45%.

<div align="center">(a)   (b)   (c)</div>
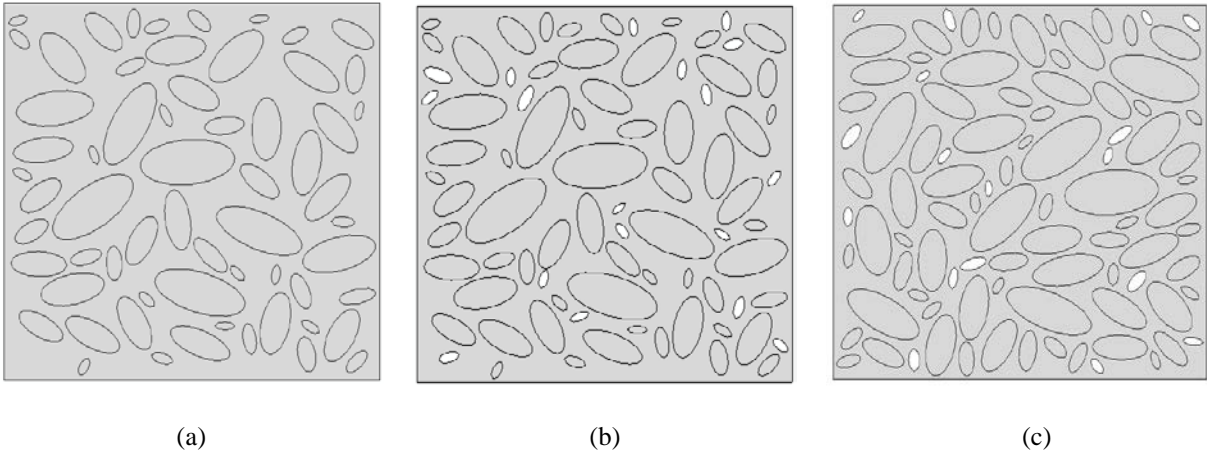
Figure 4.3. Numerical samples with elliptical aggregates: (a) P_{void}=0%, P_{agg}=40%; (b) P_{void}=2%, P_{agg}=40%; and (c) P_{void}=2%, P_{agg}=45%.
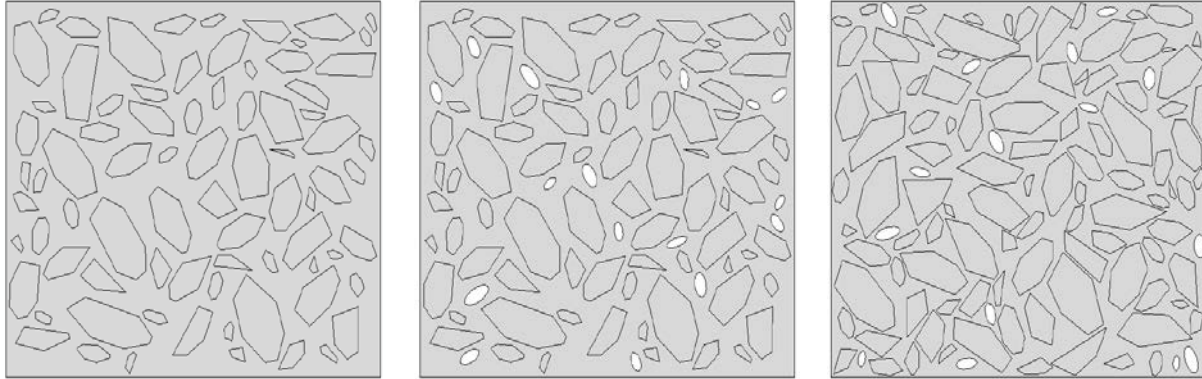
Figure 4.4. Numerical samples with polygonal aggregates: (a) P_{void} =0%, P_{agg}=40%; (b) P_{void} =2%, P_{agg}=40%; and (c) P_{void} =2%, P_{agg}=45%.

After the meso-scale structure is obtained, the pre-processing functionalities in ABAQUS controlled by Python script are utilized to generate the finite element model. The regions for the aggregates and air voids are identified by Boolean operations. The sample is meshed automatically by 3-node linear plane stress triangle elements (CPS3).

The 4-node two-dimensional cohesive element (COH2D4) is inserted between adjacent CPS3 elements to realistically capture the fracture process of concrete. Three sets of cohesive elements with different traction-separation softening behaviors are inserted. The COH-AGG elements are inserted inside the aggregates, which are assumed to be elastic and no damage will happen in COH-AGG elements. The COH_MOR elements are inserted inside the mortar matrix. At the interface between mortar and aggregate elements, the COH_ITZ elements with weaker strength are inserted in order to simulate the ITZ zone. For example, for the circular aggregates and air voids, the three sets of cohesive elements are illustrated as red lines in Figure 4.5.

<div align="center">(a)   (b)   (c)</div>
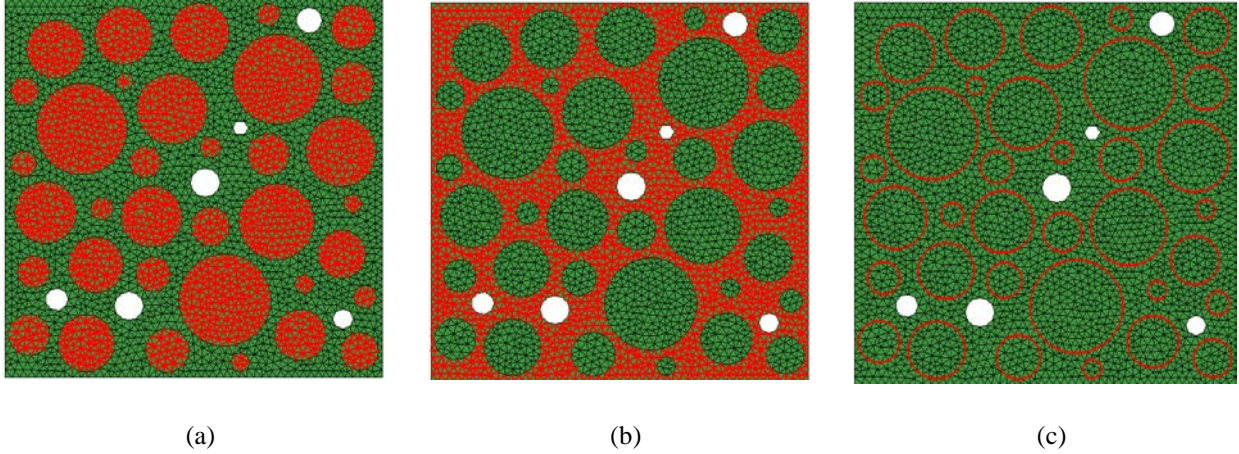
Figure 4.5. The finite element mesh showing different cohesive interface elements: (a) COH-AGG; (b) COH-MOR; and (c) COH_ITZ.

4.3   CONSTITUTIVE MODELS

Only the mortar matrix is assumed to have time-depenent bahavior while the aggregate is assumed to be purely elastic. The viscoelastic behavior of the mortar matrix is captured by the rheological model consisting of aging Kelvin chain units. The complete 1D model for mortar creep and shrinkage has been schematically represented in Figure 3.2. Model B4 is utilized here to characterize the creep bahavior of mortar matrix.

Moisture transport processes associated with drying shrinkage are not considered here due to the fact that the dimension of the meso-scale structure utilized is relatively small. Drying shrinkage of the mortar matrix in the 2D model is therefore assumed uniform. Shrinkage of the mortar matrix is linked to the moisture state through the shrinkage coefficient, i.e. the slope of the strain vs. relative humidity curve. This curve is approximately linear for the cement paste with *w/c* ratio from 0.4 to 0.5 in the relative humidity range of 40%-100% [92]. Constant shrinkage coefficient of 0.07 mm/m%RH is adopted [92].

The simulation of the energy dissipation process in the fracture process zone (FPZ) during fracture can be realistically captured by the cohesive crack model proposed by Barenblatt [93] and Dugdale [94]. The cohesive element assumes that there exists a normal traction t_n and a tangential traction (shear cohesion) t_s across the crack surface, through which the fracture mechanisms like material bonding, aggregate interlocking and surface friction can be simulated. The cohesion force decreases monotonically as a function of the corresponding relative displacement of the crack surfaces (crack opening displacement δ_n and crack sliding displacement δ_s).

The typical linear softening curves for the cohesion force and crack opening in the normal direction (t_n-δ_n) and in the shear direction (t_s-δ_s) are illustrated in Figure 4.6. The linear ascending branch is added in each softening curve to model the initially un-cracked material. The unloading paths are also indicated. The areas under the curves represent the mode-I fracture energy G_{nf} and the mode-II fracture energy G_{sf}, respectively. Both G_{nf} and G_{sf} can be treated as material properties. The initial tensile stiffness k_{n0} before tensile strength t_{n0} should be high enough to represent the un-cracked material, but not high enough to cause numerical ill-conditioning. If δ_n is negative during loading increments or iterations, a compressive stiffness equal to k_{n0} is assigned in order to prevent penetration of crack surfaces.

(a)   (b)
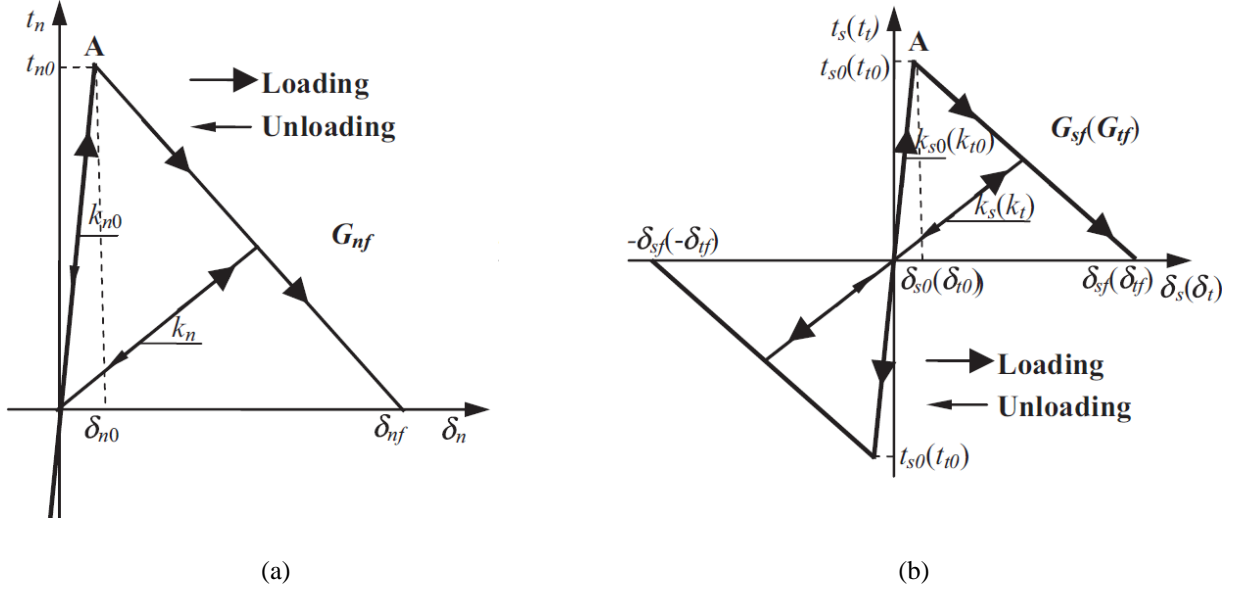
Figure 4.6. Traction-separation laws for the cohesive elements [24]: (a) in normal direction, and (b) in shear direction.

The evolution of damage under the combined normal and tangential separations is described via a scalar index D. To this end an effective relative displacement δ_m, introduced as:

$$\delta_m = \sqrt{<\delta_n>^2 + \delta_s^2} \tag{4.3}$$

where $<>$ is the Macaulay bracket, is used to define the damage scalar:

$$D = \frac{\delta_{mf}(\delta_{m,\max} - \delta_{m0})}{\delta_{m,\max}(\delta_{mf} - \delta_{m0})} \tag{4.4}$$

where $\delta_{m,\max}$ is the maximum effective relative displacement obtained during the load history, and δ_{m0} (δ_{mf}) denotes the effective relative displacement at damage initiation (final failure). Damage variable D affects the stiffness coefficient k_n and k_s for the loading and reloading, which change correspondingly to:

$$k_n = (1-D)k_{n0}, \quad k_s = (1-D)k_{s0} \tag{4.5}$$

This also affects the tractions, which change to

$$t_n = \begin{cases} (1-D)\overline{t}_n, & \overline{t}_n \geq 0 \\ \overline{t}_n, & \overline{t}_n, < 0 \end{cases},$$

$$k_s = (1-D)k_{s0} \tag{4.6}$$

$$t_s = (1-D)\overline{t}_s$$

where $\overline{t}_n$ and $\overline{t}_s$ are the traction components predicted by the elastic traction-displacement behavior for the current separation without damage.

The theoretical framework described above is used for the cohesive elements with different parameters for the three sets. The simulations are run with zero-thickness cohesive elements. The results are found to be strongly sensitive to the normal stiffness of the elements. High values of the normal stiffness would cause the convergence problem while low values will cause spurious compliance. This effect becomes more pronounced with a higher aggregate content.

4.4   VERIFICATION

The capability of the presented material model and the capability of cohesive elements to capture the micro-scale cracks of concrete are verified by modelling a well-documented experiment [92]. The drying shrinkage of the mortar matrix is subject to mechanical restraint caused by the coarse aggregates in concrete, which would lead to micro-cracking inside the mortar matrix. The experiment shows that the aggregate-induced cracks upon drying shrinkage and creep increase

with the aggregate size and volume fraction. There is a critical aggregate size, below which the aggregate-restraint does not cause experimentally detectable microcracks.

The 2 mm thick square plates are cast with the Portland cement (Type I) of $w/c = 0.50$. The aggregates are replaced by steel cylindrical inclusions whose axes are perpendicular to the plate. The spatial distribution of these steel inclusions is determined by the pseudo-random number for each coordinate of the inclusion center. The geometrical restrictions are set to avoid the overlapping of the inclusions and the contact between the inclusions and boundaries. Two volume fractions of inclusions, 10% and 35%, with deferent sizes of steel inclusions and square plates, are adopted in the experiments. In this section, the two volume fractions of inclusions are simulated and compared with the experimental results. One is 10% with 5.97 mm diameter steel cylinders embedded in a 65 mm square plate and the other is 35% with 3.98 mm diameter steel cylinders embedded in a smaller 43.3 mm square plate.

The drying tests start at age of 28 days and are carried out in a climate chamber at 20 ±2 ºC. These samples are dried from both surfaces, while the 2mm-thick sample edges are covered with layers of adhesives tape. The relative humidity in the climate chamber is lowered to 60% in one week: 1 day at 95%, 3 days at 80%, and 3 days at 70%. Next, relative humidity is kept at 60% for additional 31 days. After that, the specimens are impregnated with epoxy resin, which penetrates into the cracks by capillary force. The specimens are then photographed with a high-resolution camera under a fluorescent light, which is reflected by the dye in the epoxy resin [92]. However, this method does not allow for the detection of cracks at the matrix-inclusion interfaces.

Unfortunately, the experiment [92] does not give the macro-scale tensile or compressive strength of cement paste with $w/c = 0.50$. The strength of the cement paste has to be adjusted to

realistically capture the experimental results. According to the suggested values given in [95], the adjusted parameters for the cement paste with $w/c = 0.50$ are given in Table 4.2. In both models, the drying shrinkage of the matrix phase in the 2D-model is assumed to be uniform, and is taken as 0.07/mm/m/%RH, which corresponds to the slope of the experimentally measured curve of cement paste with $w/c = 0.5$. The creep parameters of model B4 are determined by fitting short-term experimental data measured on sealed and saturated samples made with the same water-cement ratio ($w/c = 0.5$) [95]. The material parameters used in this chapter for B4 model are listed in Table 4.3.

Table 4.2. Material properties for mechanical behavior

	Aggregate	Mortar	COH-AGG	COH-MOR	COH_ITZ
Young's modulus (GPa)	70	20	/	/	/
Poisson's ratio	0.2	0.2	/	/	/
Elastic Stiffness k_{n0} (MPa/m)	/	/	10^9	10^9	10^9
Elastic Stiffness k_{s0} (MPa/m)	/	/	10^9	10^9	10^9
Cohesive strength t_{n0} (MPa)	/	/	/	4	2
Cohesive strength t_{s0} (MPa)	/	/	/	6	4
Fracture energy G_f (N/m)	/	/	/	60	30

Table 4.3. The material constants for the model B4 in mortar matrix

q_1 (10^{-6}/MPa)	13.9
q_2 (10^{-6}/MPa)	0.0011
q_3 (10^{-6}/MPa)	123
q_4 (10^{-6}/MPa)	58.9
q_5 (10^{-6}/MPa)	540

The comparisons of the measured crack patterns at the middle-section with the computed patterns are shown in Figure 4.7 and Figure 4.8. The computed crack patterns do not show microcracks narrower than 1 micrometer, which probably could not be detected by the experimental method. The comparisons suggest that the meso-scale model can capture the time-dependent behavior of the experiment.

(a)   (b)
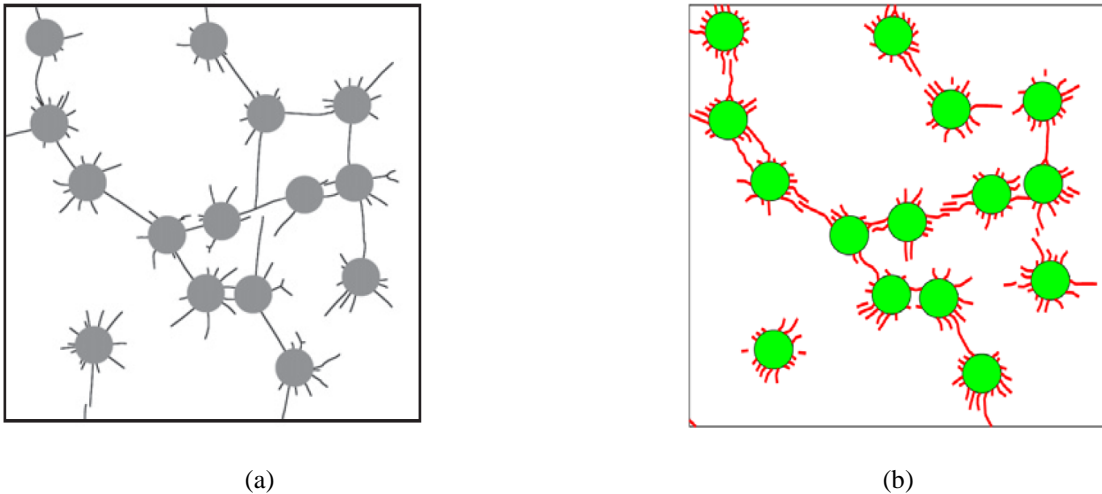
Figure 4.7. Comparison of sample with 10% aggregate content: (a) measured crack patterns [92], and (b) computed crack patterns.

<div align="center">(a)   (b)</div>
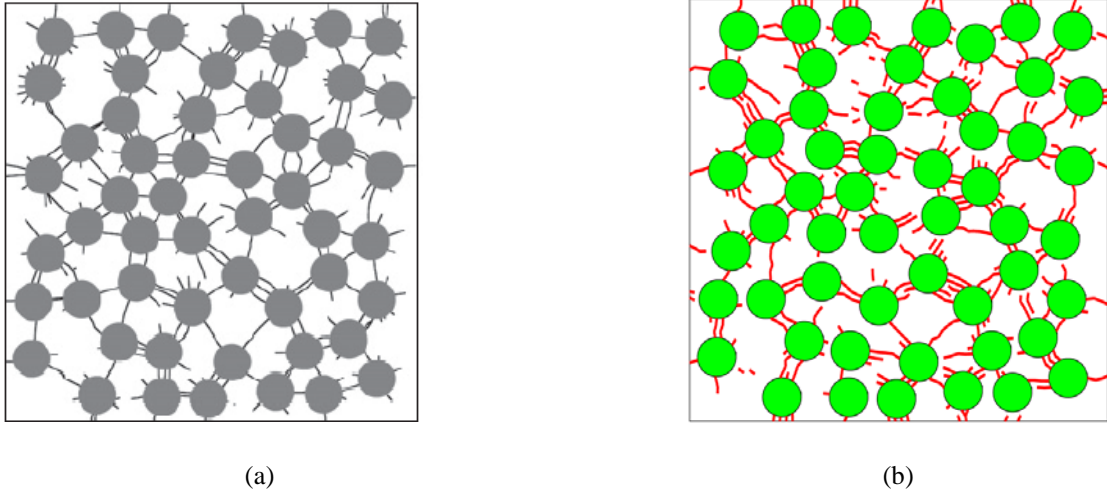
Figure 4.8. Comparison of sample with 35% aggregate content: (a) measured crack patterns [92], and (b) computed crack patterns.

4.5   MECHANICAL BEHAVIOR

Several 50×50 mm numerical meso-scale structures are simulated to investigate the mechanical and time-dependent behaviors of concrete. The solid elements for aggregates and mortar are assumed linear elastic. The damage at meso-scale is captured by the cohesive elements. The linear tension/shear softening law is used to model the linear damage evolution criteria in cohesive elements. The quadratic nominal stress initiation criterion is utilized to determine the damage initiation. For the purpose of parametric study, the material parameters listed in Table 4.2 are utilized for the virtual simulations. The volume fractions of the coarse aggregate and air voids are selected as P_{agg}=40% and P_{void}=2%, respectively. In practice, the coarse aggregates take about 30-50% of the concrete volume. Nevertheless, placing a high content of coarse aggregate ($\geq 50\%$) in a predefined domain using "taking" and "placing" algorithm is still a research challenge [24]. In light of this obstacle, P_{agg}=40% is selected here. Three combinations,

namely, circular aggregate & circular air void, elliptical aggregate & elliptical air void, and polygonal aggregate & elliptical air void, are selected for the study. For each combination, three cases are simulated to study the random distributions of aggregates and voids. The numerical samples are illustrated in Figure 4.9, Figure 4.10, and Figure 4.11, respectively.

| (a) | (b) | (c) |
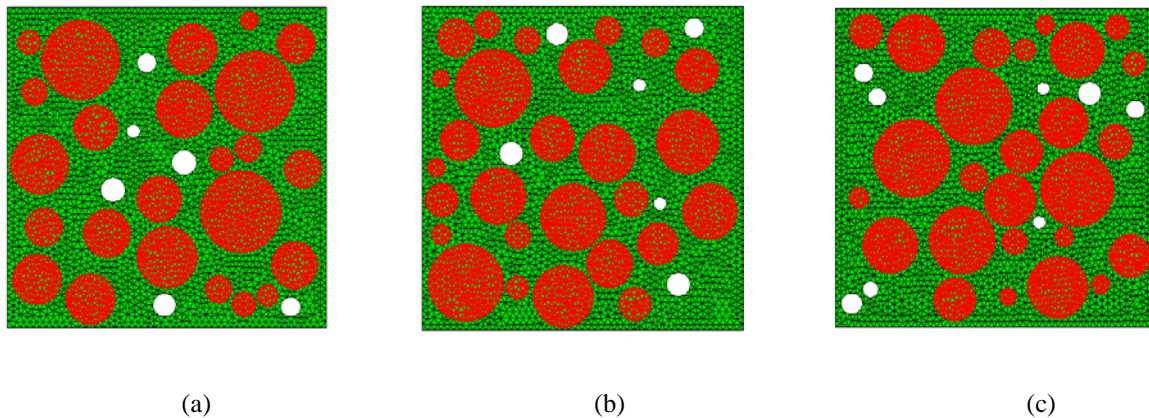
Figure 4.9. Numerical samples with circular aggregates and circular voids (P_{void}=2% and P_{agg}=40%): (a) Case 1; (b) Case 2; and (c) Case 3.

| (a) | (b) | (c) |
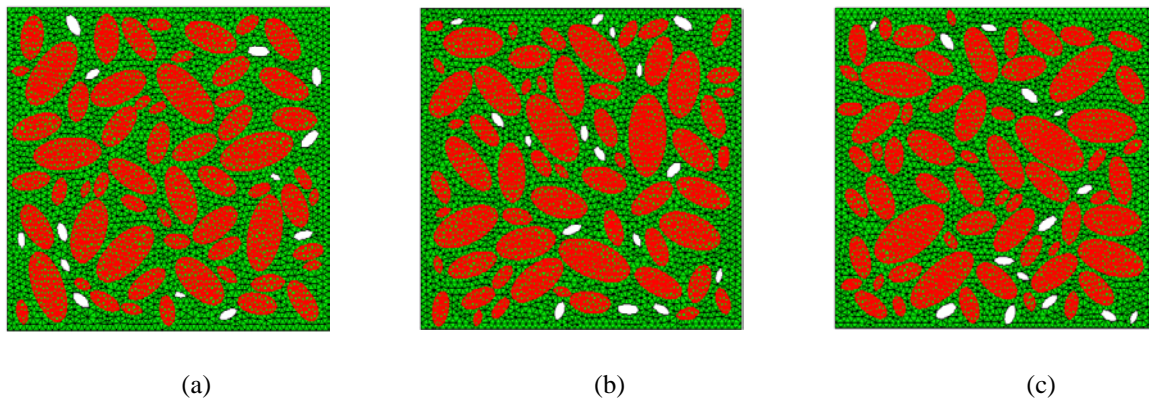
Figure 4.10. Numerical samples with elliptical aggregates and ellptical voids (P_{void}=2% and P_{agg}=40%): (a) Case 1; (b) Case 2; and (c) Case 3.

(a)   (b)   (c)
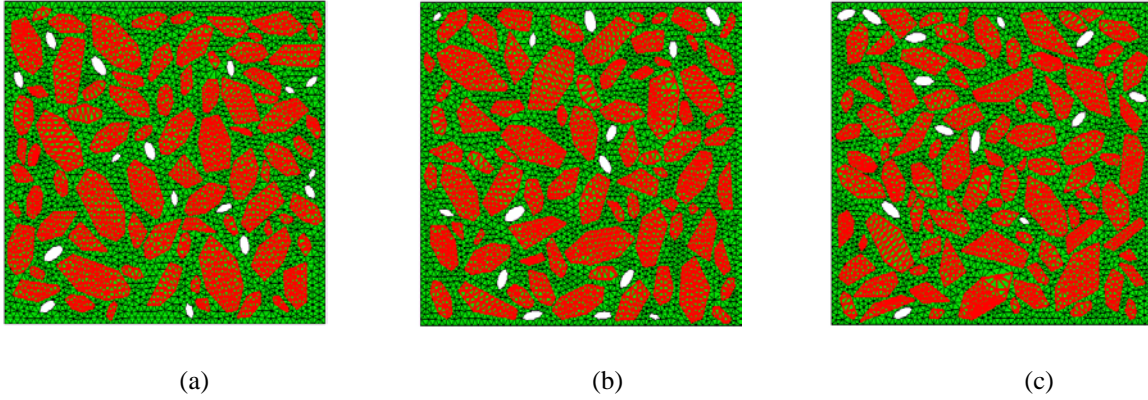
Figure 4.11. Numerical samples with plygonal aggregates and ellptical voids (P_{void} =2% and P_{agg}=40%): (a) Case 1; (b) Case 2; and (c) Case 3.

For the uniaxial tension and compression simulations, all the models are fixed at the left boundary in the horizontal direction (Figure 4.12). A displacement-control scheme is utilized for the mechanical simulations and the uniformly distributed displacement is applied at the right side boundary. For uniaxial tension (compression), the analysis is terminated at a displacement of 0.1 (-0.2) mm or a strain of 0.2% (-0.4%).
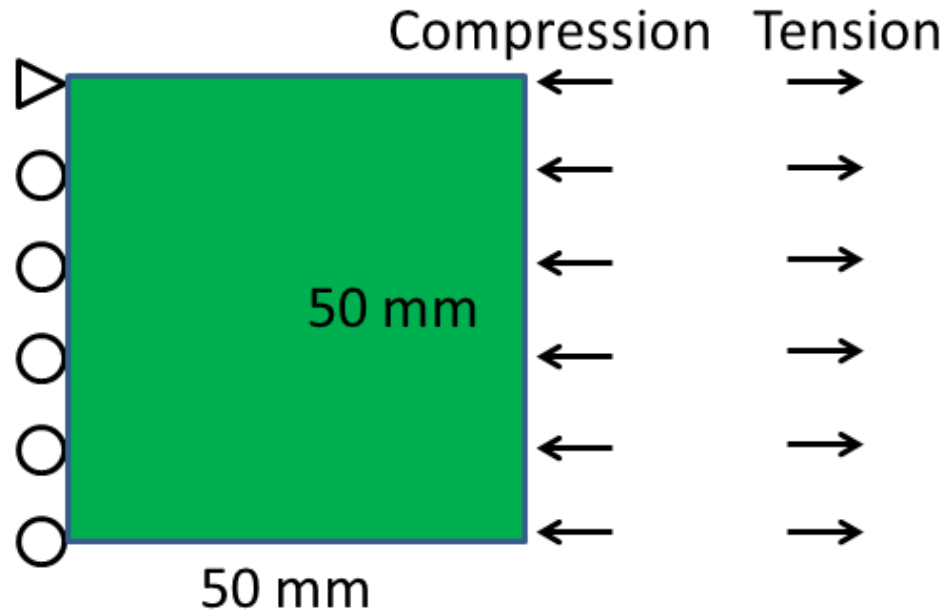
Figure 4.12. loading and boundary condtions for meso-scale structure.

The mechanical and time-dependent problems are solved in a quasi-static manner based on Newton's second law of motion. When conducting the explicit quasi-static analysis, the kinetic energy of the meso-scale structure is compared with the internal energy during the simulation. The conservation of energy requires that the sum of kinetic energy and internal energy is equal to the work done by the external forces. A quasi-static process is achieved if the kinetic energy is less than 5% of the internal energy at any time step. In order to realize the quasi-static analysis, the loading time for the mechanical analysis is tried several times. Finally, the loading time is selected as $t = 0.1$s, which can, on one hand lead to the steady quasi-static analysis, and on the other hand save computational cost. A mesh convergence study is also conducted by setting element length $L = 2$ mm, 1 mm and 0.5mm, respectively. The meso-scale structure with circular coarse aggregates and voids is tested (Figure 4.13), and the stress-strain curves corresponding to different element sizes for the uniaxial tension are plotted in Figure

115

4.14. It can be seen that the difference between the curve for $L = 1$ mm and curve for $L = 0.5$ mm is ignorable, indicating the achievement of convergence. Therefore, $L = 1$ mm is finally chosen for all the subsequent analyses.

(a)   (b)   (c)
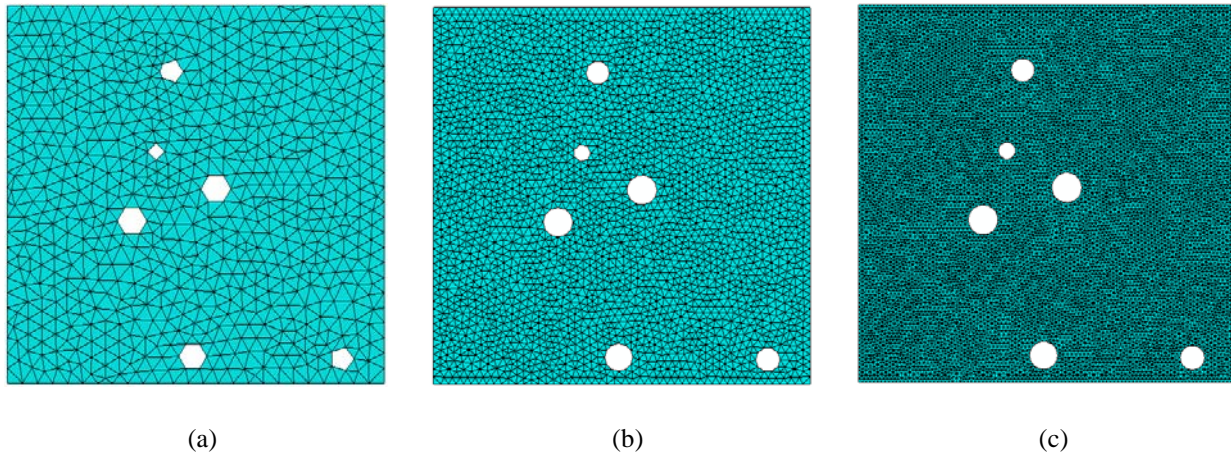
Figure 4.13. Meshing with different element size: (a) L = 2 mm; (b) L = 1 mm; and (c) L = 0.5 mm.
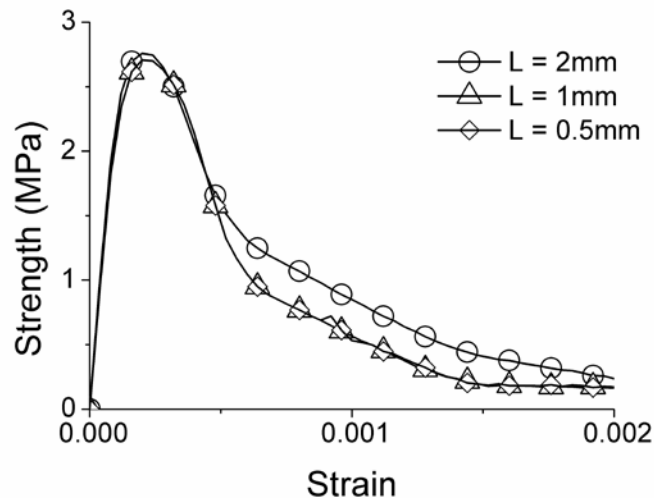
Figure 4.14. Strain-stress curves of uniaxial tension for different mesh length.

The stress-strain curves for the tension computed from the three samples with random distribution of aggregates and air voids are shown in Figure 4.15. The mean curve is shown by the red line and the individual test is shown by a black line. The peak stress decreases when the shape of aggregate changes from circle (2.65MPa) to ellipsoid (2.52MPa) and polygon (2.59MPa). When the aggregate is circular, the stress concentration will be mitigated when compared to the ellipsoid and polygon aggregates, which will lead to relatively higher tensile stress [26]. Before the peak stress is reached at about $d = 0.01$mm, the scatter of the stress before the peak stress is relatively low for the circular and elliptical aggregates. Also, the magnitude of peak stress seems to be less affected by the distribution of circular and elliptical aggregates. For the polygonal aggregates, the scatter is conspicuous for the peak stress, indicating that the sharp shape of the polygonal aggregates has a considerable influence on the tensile strength. As for the post peak part, the softening response seems to be more sensitive to the random distribution of aggregates and air voids.

(a)

117
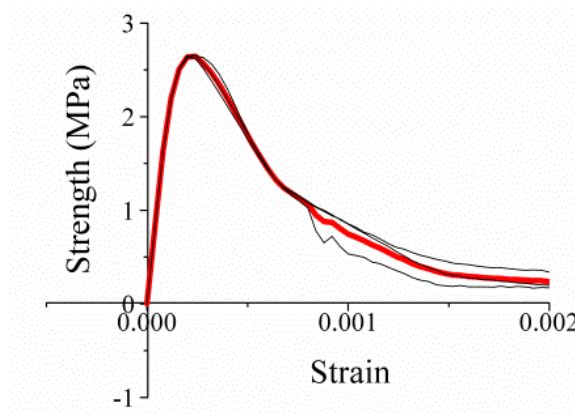
(b)
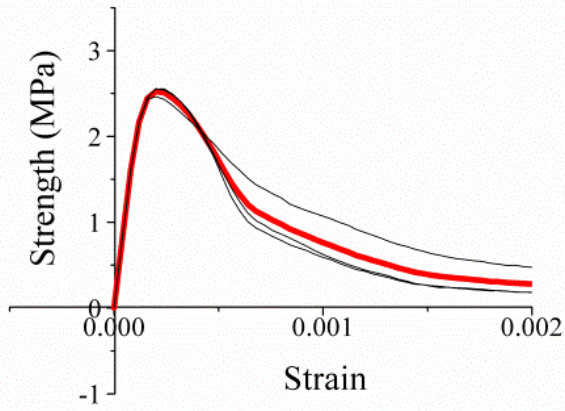
(c)
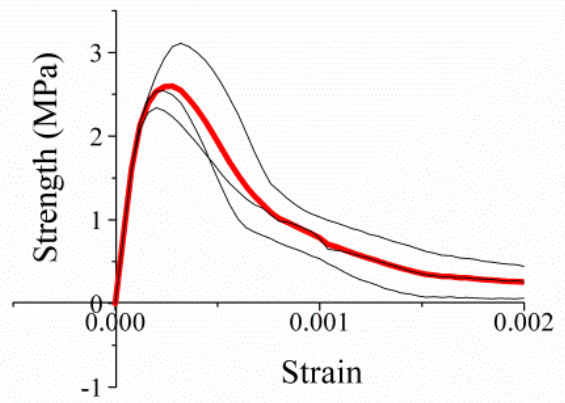
Figure 4.15. Strain-stress curves of uniaxial tension for: (a) numerical samples with circular aggregates and air voids, (b) numerical samples with elliptical aggregates and air voids, and (c) numerical samples with plygonal aggregates and ellptical air voids.

The microcracks initiate on the aggregate-mortar interface due to the ITZ zone that has lower fracture properties than mortar. Microcracks before peak load are not evident. As the displacement increases, some aggregate-mortar interfacial cracks continue to propagate and are gradually coalesced with the newly formed cracks in the mortar. The predicted post-peak microcracks for the numerical specimens are shown in red color in Figure 4.16. Two typical fracture patterns are observed for the numerical samples under uniaxial tension.

118
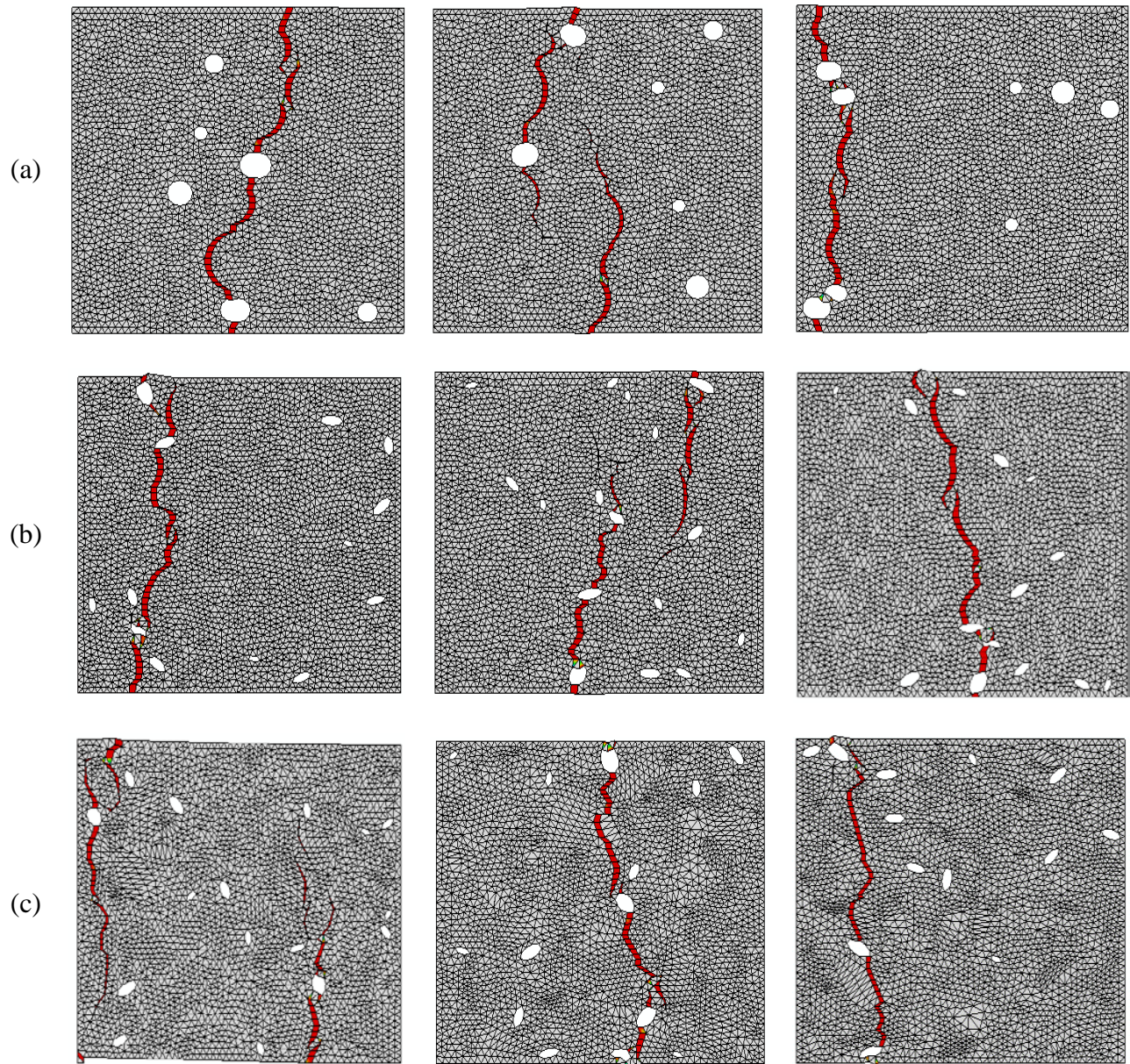
Figure 4.16. Crack pattern for the uniaixal tension after failure: (a) numerical samples with circular aggregates and air voids, (b) numerical samples with elliptical aggregates and air voids, and (c) numerical samples with plygonal aggregates and ellptical air voids.

The stress-strain curves for the uniaxial compression computed from three samples with random distribution of aggregates and air voids are shown in Figure 4.17. The mean curve is

shown by the red line and the individual test by a black line. The peak stress decreases when the shape of aggregate changes from circle (40.1MPa) to ellipsoid (37.6MPa) and polygon (35.3MPa). Similar to uniaxial tension, the stress concentration will be mitigated compared to the elliptical and polygonal aggregates when the aggregates are circular. The scatter of the stress before the peak stress is low. The constitutive laws for the cohesive elements are primarily for modelling the interface fracture, and do not represent fully the coupling of shear and normal responses, particularly the interaction between shear and compression. It is expected that this simplification only has a minor effect on the analysis of concrete under uniaxial compression in the pre-peak regime dominated by tensile micro-cracking. The effect on the post-peak regime dominated by compressive micro-cracking, governed by the micro-crack coalescence and associated development of shear failures, might be captured less effectively. The predicted post-peak microcracks for the numerical specimens are shown in red color in Figure 4.18.

(a)
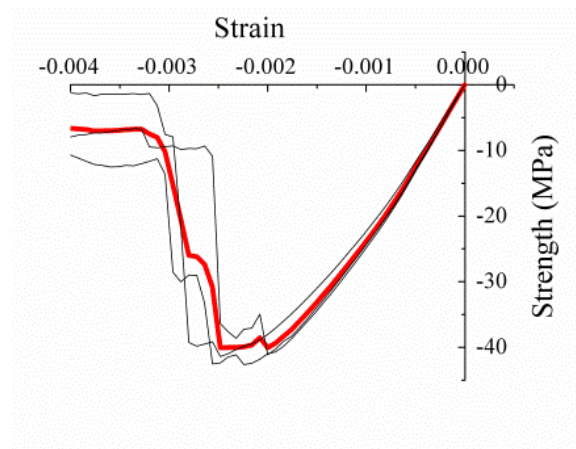
(b)
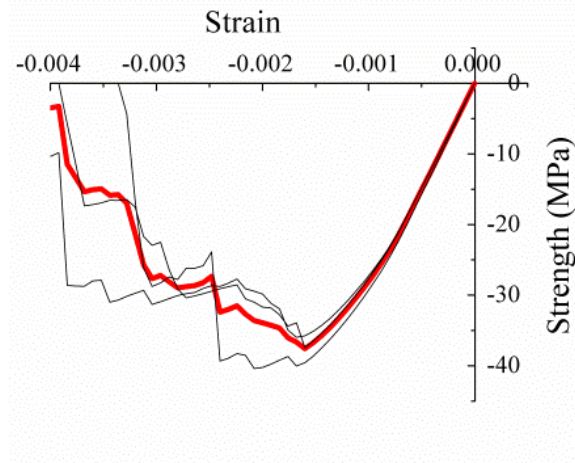
(c)
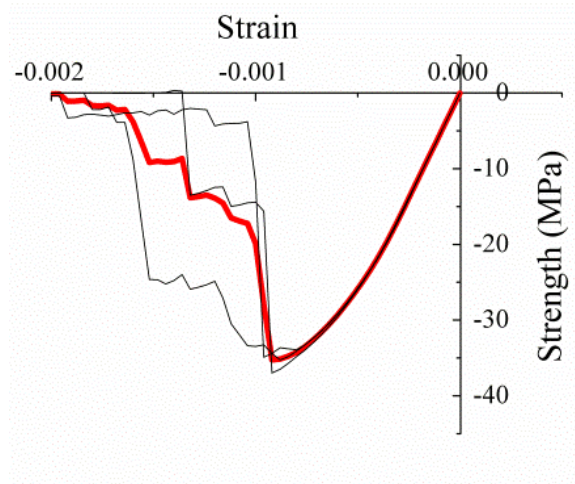
Figure 4.17. Strain-stress curves of uniaxial compression for: (a) numerical samples with circular aggregates and air voids, (b) numerical samples with elliptical aggregates and air voids, and (c) numerical samples with plygonal aggregates and ellptical air voids.
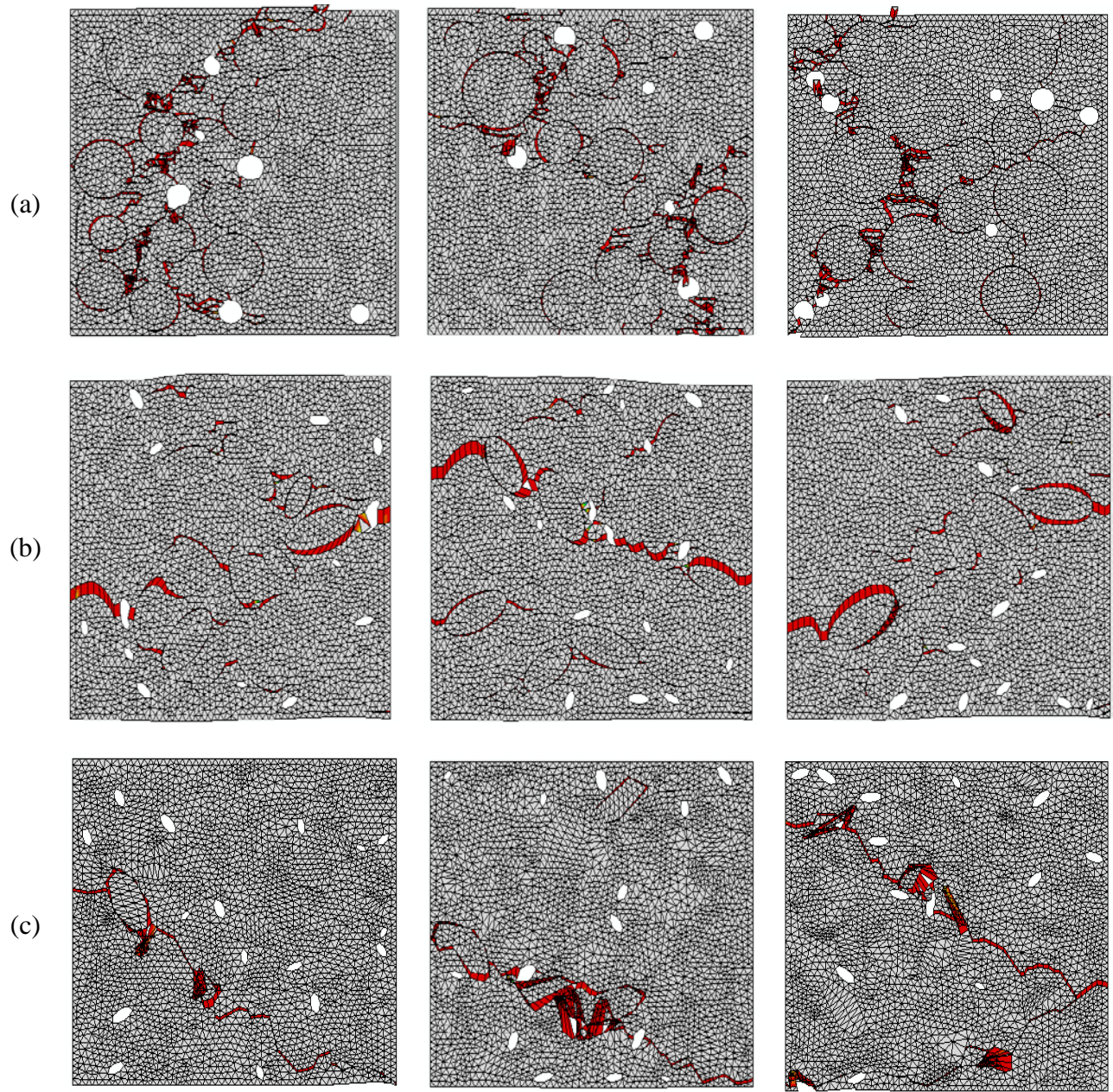
Figure 4.18. Crack pattern for the uniaixal compression after failure: (a) numerical samples with circular aggregates and air voids, (b) numerical samples with elliptical aggregates and air voids, and (c) numerical samples with plygonal aggregates and ellptical air voids.

4.6   TIME-DEPENDENT BEHAVIOR

After the maximum compression force is determined for the numerical specimen, two load levels, 20% and 60% of the maximum compressive force, are applied on the same numerical meso-structure of concrete, to investigate the time-dependent deformation under different load level. In order to simplify the analysis, the shrinkage deformation is not considered for all the cases and only creep deformation, which is approximated by the model B4, is considered. The creep deformation lasting 5 days after loading is investigated.

For the different combinations of aggregates and voids, the creep deformations are shown in Figure 4.19(a), Figure 4.20(a), and Figure 4.21(a), respectively. The average creep deformation of the 20% load level $\zeta_{0.2}$ is shown with the blue line and the average creep deformation of the 60% load level $\zeta_{0.6}$ are shown with the red line. The ratios of creep deformation ($\frac{(\zeta_{0.6}/0.6)}{(\zeta_{0.2}/0.2)}$) are shown in Figure 4.19(b), Figure 4.20(b), and Figure 4.21(b), respectively. The average ratios of creep deformation are plotted as the red line.
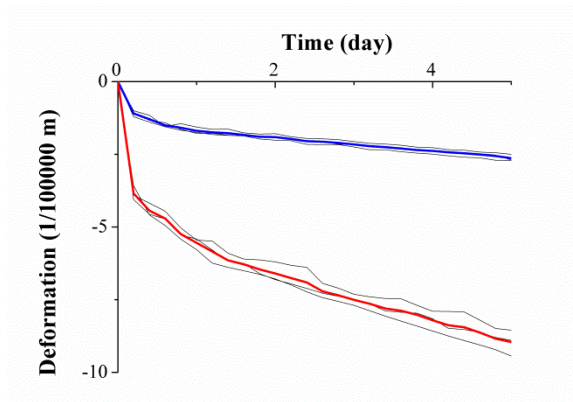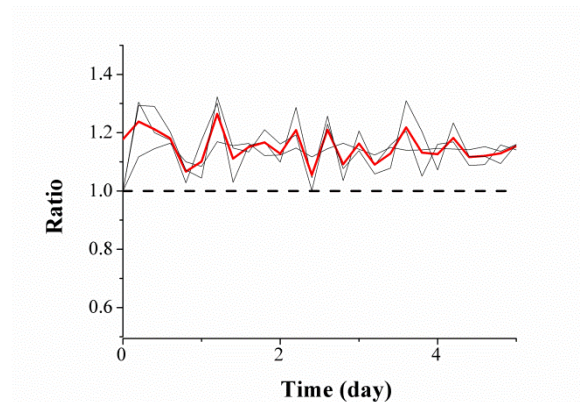
(a)   (b)

Figure 4.19. Numerical samples with circular aggregates and circular air voids: (a) creep deformaiton, and (b) ratio of creep deformation.
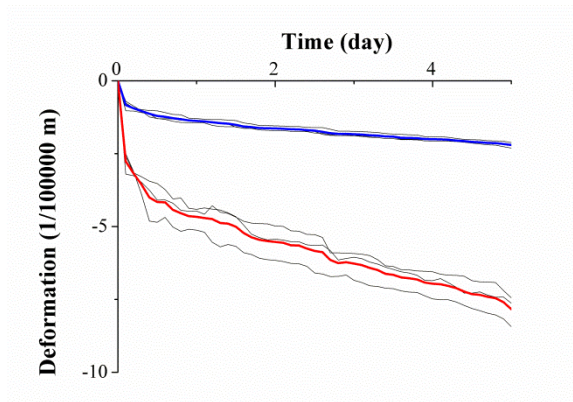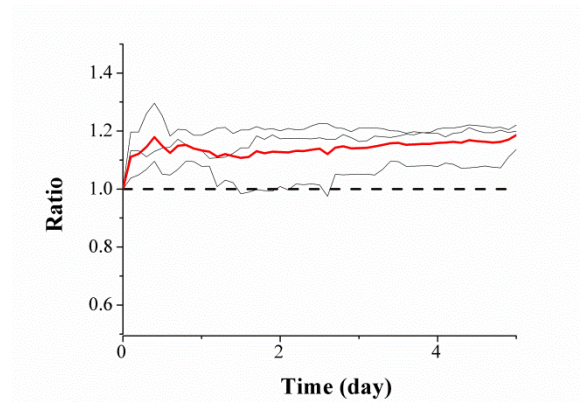
(a)   (b)

Figure 4.20. numerical samples with elliptical aggregates and elliptical air voids: (a) creep deformaiton, and (b) ratio of creep deformation.

124
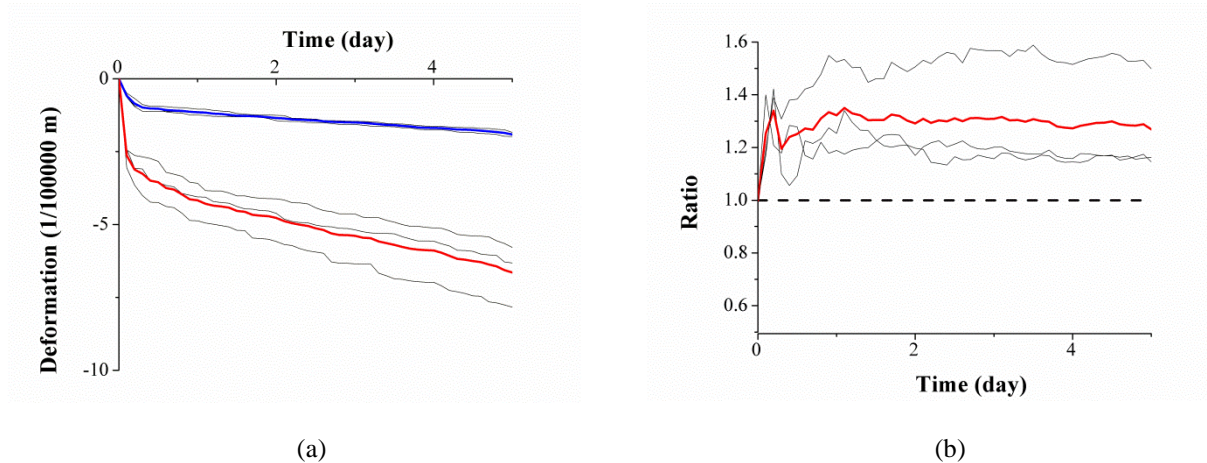
Figure 4.21. numerical samples with plygonal aggregates and elliptical air voids: (a) creep deformaiton, and (b) ratio of creep deformation.

If there were no damage evolution inside the mortar matrix and ITZ zone, the creep deformation of the numerical specimens would vary linearly with the level of applied load. The ratio of $\dfrac{(\zeta_{0.6}/0.6)}{(\zeta_{0.2}/0.2)}$ should be equal 1.0. However, Figure 4.19 (b), Figure 4.20 (b), and Figure 4.21 (b) indicate that when the loading level is high (in this chapter, 60% of maximum load), the nonlinear creep phenomenon is more significant. This is documented by the observation that the average ratios for all the simulations are greater than 1.0. The damaged cohesive elements for numerical specimen with circular aggregates and air voids (case 1 in Figure 4.9), are shown in red color in Figure 4.22, to illustrate the damage in the sample 0 and 5 days after 60% of the ultimate compressive force is applied, respectively. Clearly, there is no damage inside the mortar matrix or the ITZ zone immediately upon after applying the load. After 5 days, the damage is apparent.

(a)   (b)
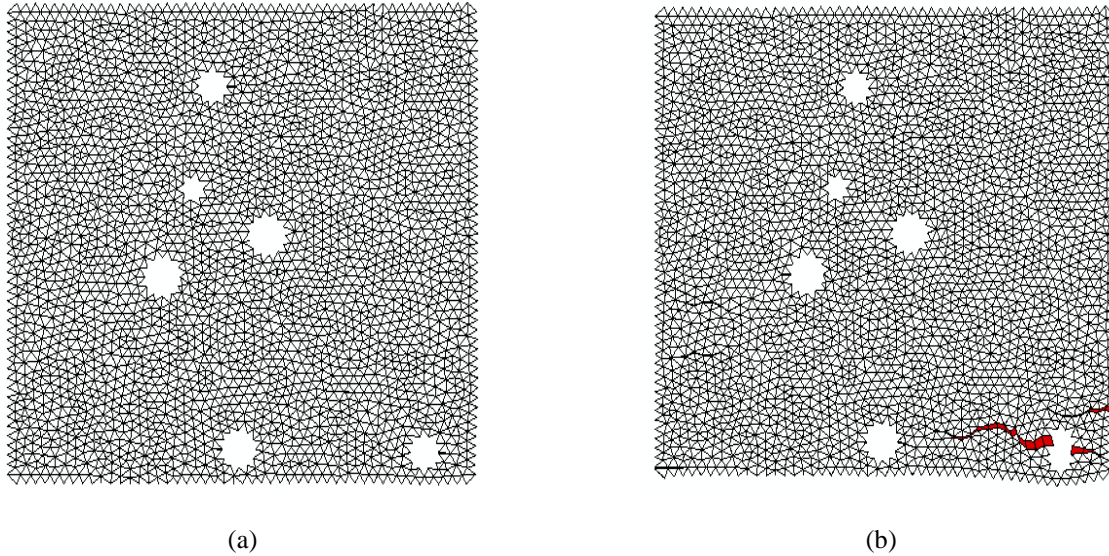
Figure 4.22. Failure cohesive elements for the mortar matrix and ITZ of the 60% of maximum load: (a) 0 day after applying load, and (b) 5 days after applying load.

4.7   MULTISCALE TIME-DEPENDENT SIMULATION

In this section, two different approaches are utilized to map the mechanical and time-dependent behaviors of the meso-scale structure to the macro-scale behavior. The first approach, the "computational multiscale analysis", directly links the macro-scale and meso-scale together. The basic idea for the computational multiscale analysis is to obtain the unknown constitutive relationship at the macro-scale by solving local finite element problems at the meso-scale [96]. The second approach, referred to as "multiscale material model", is based on the analytical solution of matrix-inclusion problem.

In this section, the results from the two different approaches are compared and their advantages and disadvantages are discussed. Only coarse aggregates and mortar matrix are

126

considered in the meso-structure of concrete. The creep using model B4 is considered and the shrinkage is not considered to simplify the analysis.

4.7.1   Computational multiscale analysis

A domain Ω^0 with an external boundary $\partial\Omega^0$ (Figure 4.23) describes the macro-scale structure at its current configuration. The superscript "0" indicates the variables at the macroscale level. It is assumed that the material is homogeneous at the macro-scale and is characterized by a periodic heterogeneous meso-structure. The macro-scale structure is subjected to prescribed displacements and forces on the Dirichlet boundaries $\partial\Omega^0_u$ and Neumaan boundaries $\partial\Omega^0_\sigma$ respectively. In the absence of body force, the problem can be expressed as:

$$\nabla\overline{\sigma}(\overline{x}) = 0 \tag{4.7}$$

where $\overline{\sigma}(\overline{x})$ is the Cauchy stress tensor associated with a point $\overline{x}$ of the macro-scale structure in the current configuration. The boundary conditions are defined as

$$\overline{u}(\overline{x}) = \hat{u}(\overline{x}) \quad \text{on } \partial\Omega^0_u$$

$$\overline{\sigma}\cdot N = F \quad \text{on } \partial\Omega^0_q \tag{4.8}$$

where $\overline{u}$ denotes the macro-scale displacement field; $\hat{u}$ is the proscribed displacement; N is the outward unit normal vector to $\partial\Omega^0$; and F is a prescribed traction.
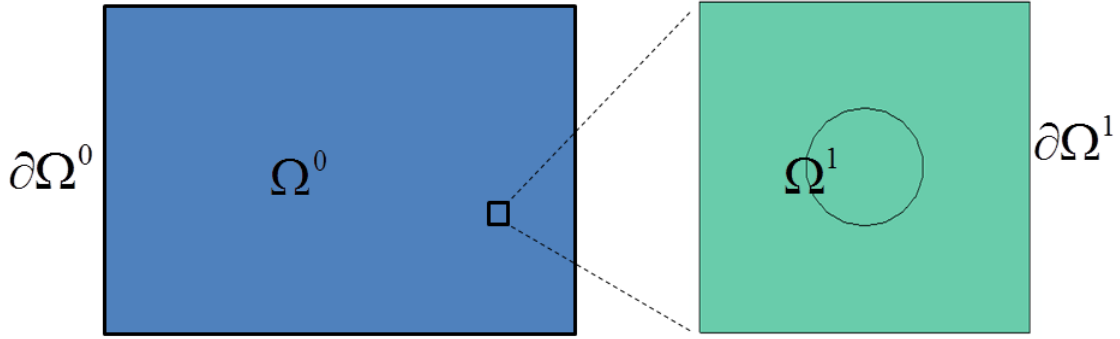
Figure 4.23. Macro-scale and Meso-scale structures for computational multiscale analysis.

However, at the macro-scale level, the constitutive law relating $\bar{\sigma}(\bar{x})$ and $\bar{\varepsilon}(\bar{x})$ is unknown. In the framework of computational multiscale scheme, the macroscale stress $\bar{\sigma}(\bar{x})$ is obtained by solving the represented volume element (RVE) subject to the macro-scale strain $\bar{\varepsilon}(\bar{x})$ at the meso-scale. The homogeneous material at the macro-scale is assumed to have a periodic meso-structure, which is characterized by the RVE occupying the domain Ω^1 with an external boundary $\partial\Omega^1$ in the current configuration. The superscript "1" indicates the variables at the meso-scale. In the absence of body force, the equilibrium equation at meso-scale is given as:

$$\nabla\sigma(x) = 0 \qquad (4.9)$$

where $\sigma(x)$ is the Cauchy stress tensor associated with a macro-scale point $\bar{x}$. The RVE is subject to boundary conditions depending on the macro-scale deformation tensor $\bar{\varepsilon}$. If nonlinear geometry is not considered and periodic boundary conditions are applied for the RVE, the deformation of the RVE will be:

$$u^+ - u^- = \bar{\varepsilon}(x^+ - x^-) \qquad (4.10)$$

where $u^\pm$ are the displacements at the meso-scale. The superscripts "+" and "–" are associated with node indices on opposite sides of the RVE, respectively. For the RVE at meso-scale, mortar

matrix and coarse aggregate are considered with different constitutive laws. The damage and failure of both mortar matrix and coarse aggregate are not considered. Linear elastic behavior is assumed for the coarse aggregate and viscoelastic (creep) behavior is assumed for the mortar matrix. The constitutive laws for coarse aggregate and mortar matrix can be expressed as:

$$\sigma(x) = C_{agg} : \varepsilon(x) \quad \text{for coarse aggregate}$$

$$\sigma(x) = C_{mor} : (\varepsilon(x) - \varepsilon''(x)) \quad \text{for mortar matrix}$$

(4.11)

where C_{agg} and C_{mor} refer to the elastic tensors associated with aggregate and mortar matrix respectively and $\varepsilon''(x)$ is the inelastic strain induced by creep in mortar matrix. The effective stress $\bar{\sigma}$ at a particular point $\bar{x}$ of the macro-scale domain Ω^0 is evaluated based on a Mori-Tanaka type homogenization scheme [97]:

$$\bar{\sigma} = \frac{1}{|\Omega^1|} \int_{\Omega^1} \sigma(x) d\Omega^1$$

(4.12)

where $|\Omega^1|$ denotes the volume of the RVE. The relationship between the macro-scale stress $\bar{\sigma}$ and the macro-scale strain $\bar{\varepsilon}$, in the case of linear constitutive law, can be written as

$$\bar{\sigma} = <\bar{\sigma}(x)> = \bar{C} : \bar{\varepsilon}$$

(4.13)

where $\bar{C}$ is the homogenized macro-scale constitutive tensor depending on constitutive laws of mesoscale constituents. In the case of a nonlinear constitutive law at the meso-scale, this relationship can be written in an incremental form:

$$\Delta\bar{\sigma} = \bar{C}_t : \Delta\bar{\varepsilon}$$

(4.14)

where $\bar{C}_t$ is the homogenized macro-scale tangent modulus depending on the nonlinear behavior of the meso-scale constituents. At each macro-scale load increment, the tangent modulus $\bar{C}_t$ is

computed at each integration point, by solving a finite element problem at the RVE level. The periodic boundary conditions are written in the incremental form:

$$\Delta u^+ - \Delta u^- = \Delta \bar{\varepsilon}_i^n (x^+ - x^-) \tag{4.15}$$

where n and i are the number of macroscale load increments and the number of equilibrium iterations respectively. Then the meso-scale tangent problem can be written as:

$$\int_{\Omega^1} \Delta \sigma : \delta \varepsilon d\Omega^1 = 0 \tag{4.16}$$

Once the increment of macro-scale strain $\Delta \bar{\varepsilon}_i^n$ is applied, the analysis at the meso-level is performed and the macro-scale stress increment $\Delta \bar{\sigma}_i^n$ is obtained by Eq. (4.14). At this point, ABAQUS performs an incremental loading with the time increment Δt, and a new guess of $\Delta \bar{\varepsilon}_i^n$ for the strain increment until convergence is achieved. After that, a new tangent modulus is computed from the meso-scale analysis for the next time step. The multiscale computations in the macro-scale and meso-scale structures are seamlessly integrated by Python script and user-defined FORTRAN subroutines, as shown in Figure 4.24.
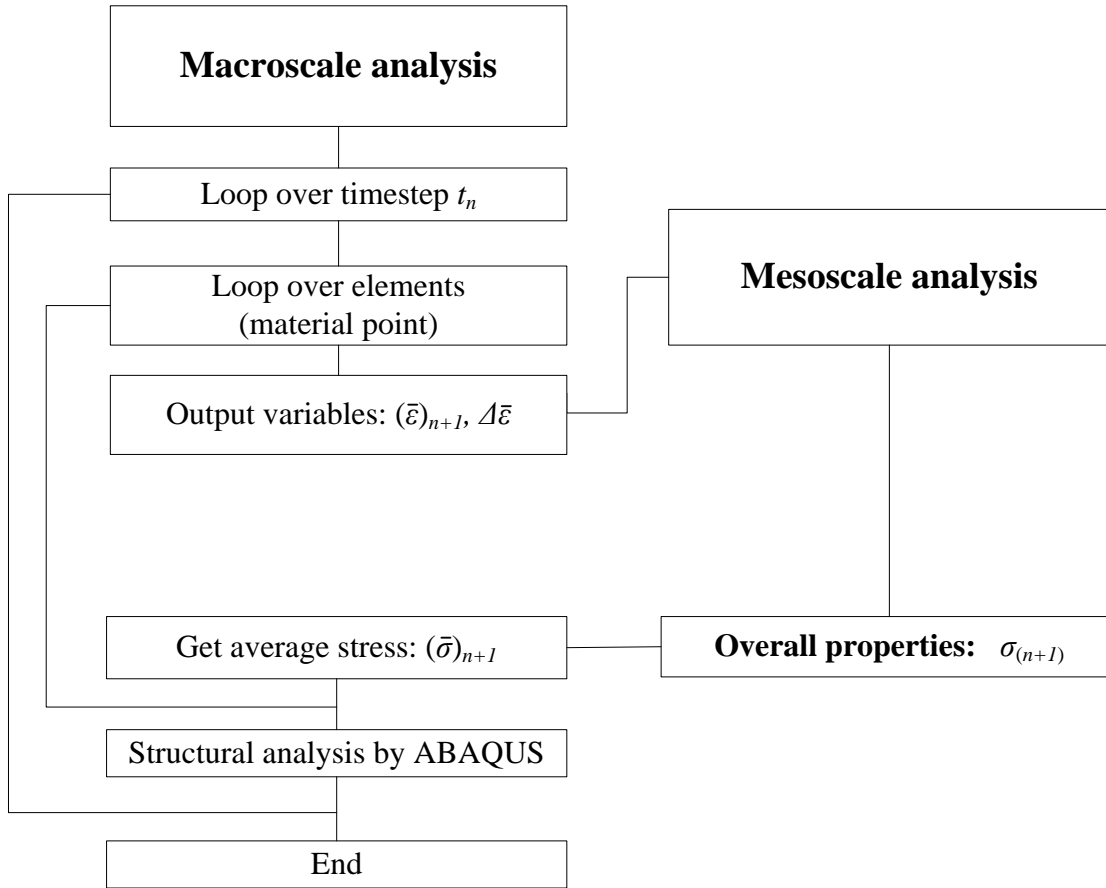
Figure 4.24. Flow chart of implementation of computational multiscale analyis in ABAQUS.

4.7.2 Multiscale material model

The multiscale material model is proposed to ameliorate the computational burden resulting from finer discretization of each phase in the computational multiscale analysis. This model is based on the micromechanical solution of matrix-inclusion problem. The classical Equivalent Inclusion Method (EIM) proposed by Eshelby [98] is utilized for the matrix-inclusion problem. However, the classical EIM is effective for an infinite domain containing an ellipsoidal inhomogeneous inclusion, and fails here due to the fact that uniform equivalent eigenstrain may not exist when the RVE is bounded. Instead, the analytical solution presented in [99], which accurately predicts

the elastic disturbance induced by an inhomogeneous inclusion in a 2D concentric finite RVE, is utilized here for illustration.

For the proposed multiscale model, the macro-scale responses must be calculated for the analysis. Based on the analytical solution for the elastic disturbance induced by an inhomogeneous inclusion in a 2D concentric finite RVE (Figure 4.25(a)), Mori-Tanaka homogenization scheme [97] is used when the average property of interest in a multi-phase domain is needed. If the volume fraction of each phase is known, then the average property can be obtained [67]. Accordingly, effective stress is determined by the stress at the meso-scale based on Eq. (4.12). In practice, different sampling nodes are seeded inside the coarse aggregate and mortar matrix. Therefore, the average stress for the macro-scale structure is expressed as:

$$\overline{\sigma} = \frac{\sum_{i=1}^{N_{agg}} \sigma_i^{agg}}{N_{agg}} P_{agg} + \frac{\sum_{j=1}^{N_j} \sigma_j^{mor}}{N_{mor}} (1 - P_{agg})$$
(4.17)

where N_{agg} and N_{mor} are the numbers of sampling nodes inside the aggregate and mortar matrix, respectively. Based on the stress obtained on the different sampling nodes inside the mortar matrix σ_j^{mor}, the creep strain $(\varepsilon'')_j^{mor}$ is subsequently obtained. The average creep strain of the macro-scale element can be obtained in a way similar to Eq. (4.17).

(a)	(b)
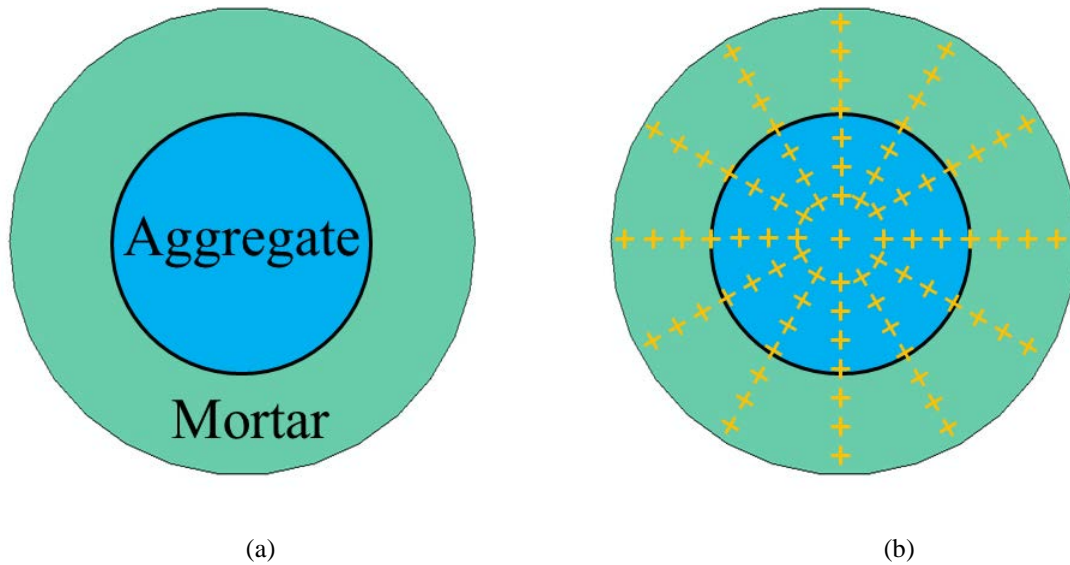
Figure 4.25. Meso-scale structure for multiscale material model: (a) 2D concentric finite RVE, and (b) distribution of sampling nodes.

4.7.3   Numerical example

In order to compare these two schemes for the multi-scale time-dependent analysis, a relatively simple macro-scale structure is adopted for illustration. A 2D column (1m × 2m) is fixed at the bottom boundary in the vertical direction, and a unit external load (1 MPa) is applied to the top boundary after 7-day curing of concrete.

Two different meso-sale RVEs are adopted here, with 10% and 40% volume fractions of coarse aggregates respectively. The 10% volume fraction of coarse aggregate is not realistic for concrete. However, the simulation is to explore the advantages and disadvantages of the two different schemes, rather than to capture the real response of concrete. The 0.05m square mortar matrix with one circular aggregate located at the center of the square is used for the computational multiscale analysis (Figure 4.26). However, for the multiscale material model, the analytical solution is achieved for 2D concentric circular matrix and circular inclusion.

Therefore, the circular mortar matrix with one circular aggregate located at the center is used as the RVE for the multiscale material model (Figure 4.27). Model B4 is considered for the mortar matrix, and linear elasticity is assumed for the coarse aggregate. The model parameters are listed in Table 4.2 and Table 4.3. In order to simplify the analysis, the shrinkage is not considered here.

(a)   (b)
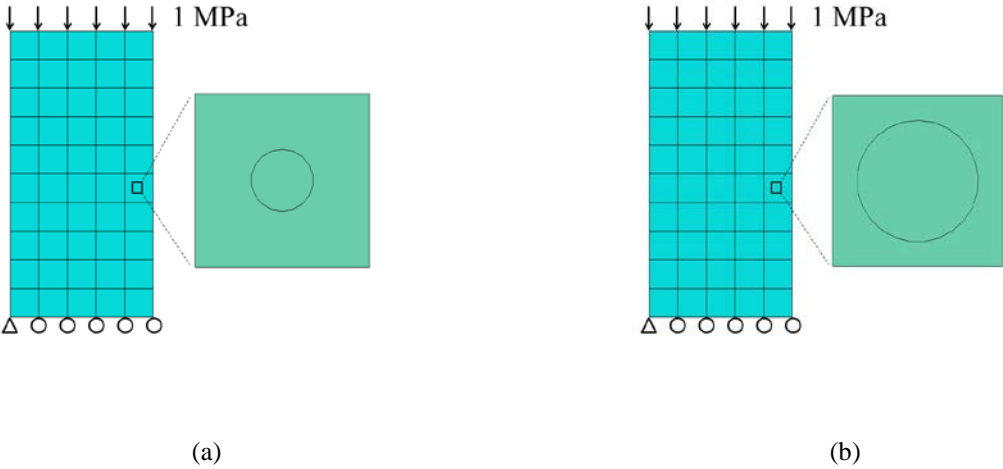
Figure 4.26. RVE structure for computational multiscale analysis: (a) 10% volume fraction of coarse aggregate; and b) 40% volume fraction of coarse aggregate.

(a)   (b)
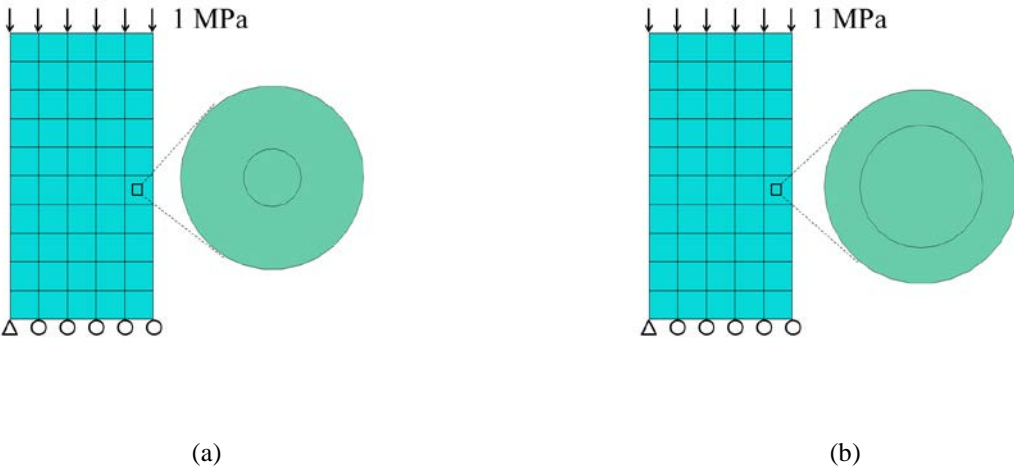
Figure 4.27. RVE structure for multiscale material model: (a) 10% volume fraction of coarse aggregate; and b) 40% volume fraction of coarse aggregate.

The vertical deformations due to creep at the top edge of columns, under two types of RVEs with different volume fractions of coarse aggregates, are shown in Figure 4.28. Clearly, the difference of the two algorithms is negligible (only about 2%), when the volume fraction of coarse aggregate is relatively small (10%). Compared to the classical Eshelby's solution [100], simulation accuracy has been improved. This improvement indicates the effectiveness of the multiscale material model utilizing the analytical solution presented in [99]. When the volume fraction increases to 40%, the difference between the two algorithms increases to 8% but still acceptable. It is supposed that when the coarse aggregate is larger, the stress difference between the two RVEs (Figure 4.26(b) and Figure 4.27 (b)) is more apparent. This is due to the simplification that replaces the rectangular mortar matrix with a circle.

(a)   (b)
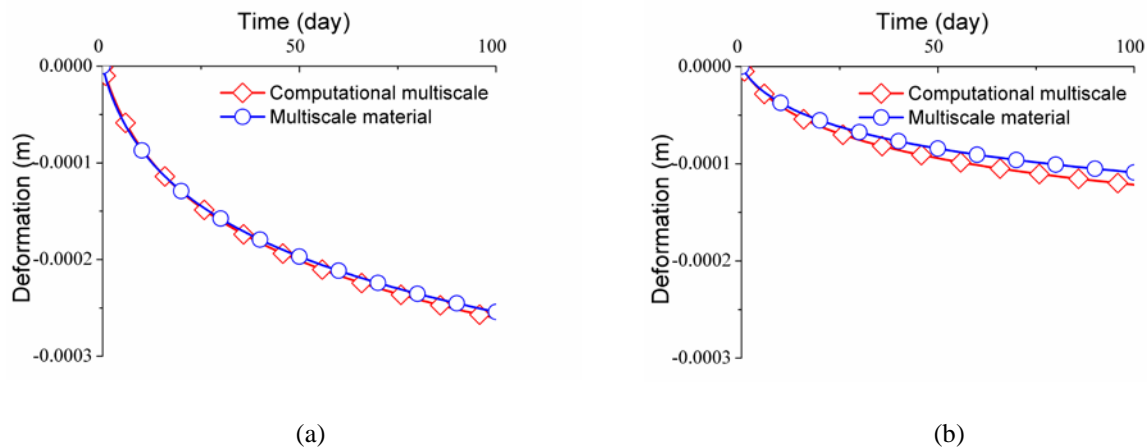
Figure 4.28. Creep deformation for: (a) 10% volume fraction of coarse aggregate; and b) 40% volume fraction of coarse aggregate.

135

4.8   SUMMARY

Numerical specimens representing different shape and spatial distributions of coarse aggregates and air voids are generated by the "taking" and "placing" algorithm in MATLAB in order to simulate and investigate the meso-scale mechanical and time-dependent behaviors of concrete. The evolution of microcracks is captured by the cohesive elements with different tension and shear softening constitutive laws, which are inserted between solid elements. Some conclusions can be obtained as follows:

(1)   If the external loading is high, the damage evolution inside the mortar matrix is responsible for the nonlinear creep deformation at macro-scale.

(2)   Two approaches, the computational multiscale analysis and multiscale material model, are utilized to map the time-dependent response of the meso-scale structure to the macro-scale response. It seems that both algorithms can capture the time-dependent behaviors of meso-scale RVE.

5.0   CONCLUSIONS

Simulations based on a large-span prestressed concrete bridge show that, under different creep models, the asymptotes of long-term deflection and axial shortening are different. The deflection and shortening asymptotes eventually approach an inclined straight-line in logarithmic time scale, if the creep models contain logarithmic time functions. The prestress level in the tendons will substantially affect the deflection asymptote. If high initial prestress is applied, the arrival of the deflection asymptote will be pushed back to over 30 years due to the long transitional period. On the other hand, the axial shortening is not sensitive to the prestress level. For initial prestress ranging from 600 to 1080 MPa, the axial shortening consistently reaches its asymptote in about 3 years or earlier. Therefore, an early establishment of correlation between creep compliance function and shortening asymptote can be achieved and then used to predict the long-term bridge deformation as well as supplement the laboratory tests.

For prestressed concrete bridges sustaining heavy traffic load, a unified constitutive model is proposed, coupling the B4 (or MC) creep and shrinkage model with an elasto-plastic damage model and a fatigue mechanics-based cyclic creep model. The performance of Hunmen Bridge is studied based on the deterministic simulations, coupling the static creep with the cyclic creep, concrete cracking, and other processes. It shows that viscoelastic analysis based on the static creep of concrete alone is not adequate to predict the long-term deflection for bridges sustaining heavy traffic load. The intertwined effects of concrete cyclic creep and concrete

cracking should be considered in the long-term performance prediction. The cyclic creep of concrete is insensitive to the traffic pattern of vehicles less than 10 tons. However, the traffic pattern of heavy trucks cannot be ignored. The percentage of trucks driving in parallel with each other can significantly impact the bridge deflection development and stress redistribution in concrete.

The meso-scale simulations are conducted to investigate the effects of the shape and spatial distribution of aggregates and air voids on the macro-scale mechanical and time-dependent behaviors of cementitious materials. The cohesive elements with different tension and shear softening constitutive laws are inserted between the solid elements to capture the potential microcracks. Compared to circular aggregates, the elliptical and polygonal aggregates will apparently lower both the tensile strength and compressive strength of concrete. The damage evolution of the mortar matrix will lead to macro-scale nonlinear creep deformation when the specimen is subject to relatively high external load. Two approaches, one is computational multiscale analysis and the other is proposed multiscale material based on matrix-inclusion problems, can accurately map the meso-structure response to the macro-scale response.
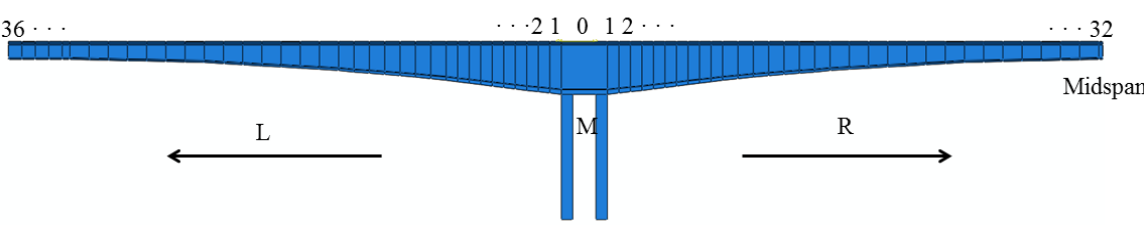
APPENDIX A

RATIO OF AVERAGE STRESS VARIATION TO CONCRETE STRENGTH

In this half model for bridge I of Humen Bridge, there are 36 segments in the side span and 32 segments in the middle span, see Figure 3.6(c) and Table A.1. In this appendix, "Li" refers to the i-th segment in the side span; "Ri" refers to the i-th segment in the middle span; and "M" stands for the segment on the pier.

The ratios of the average stress variation $\overline{\Delta\sigma}$ obtained using Eq. (3.8) to the concrete strength f_c' for different traffic patterns are listed from Table A.1 to Table A.6.

Table A.1. Ratio of average stress variation to concrete strength for traffic Pattern I

	Top slab	Bottom slab	Web		Top slab	Bottom slab	Web
M0	0.013	0.023	0.001	L35	0.002	0.004	0.001
L1	0.010	0.016	0.005	L36	0.001	0.002	0.001
L2	0.009	0.015	0.001	R1	0.013	0.022	0.001
L3	0.008	0.014	0.001	R2	0.012	0.020	0.001
L4	0.007	0.013	0.001	R3	0.011	0.019	0.001
L5	0.007	0.011	0.001	R4	0.010	0.018	0.001
L6	0.006	0.010	0.001	R5	0.010	0.017	0.001
L7	0.005	0.009	0.001	R6	0.009	0.016	0.001
L8	0.005	0.008	0.001	R7	0.008	0.015	0.001
L9	0.004	0.007	0.001	R8	0.008	0.013	0.001
L10	0.003	0.006	0.001	R9	0.007	0.012	0.001
L11	0.003	0.005	0.001	R10	0.007	0.011	0.001
L12	0.003	0.005	0.001	R11	0.006	0.010	0.001
L13	0.003	0.006	0.001	R12	0.005	0.009	0.001
L14	0.004	0.007	0.001	R13	0.004	0.008	0.001
L15	0.004	0.007	0.001	R14	0.004	0.006	0.001
L16	0.005	0.008	0.001	R15	0.004	0.007	0.001
L17	0.005	0.009	0.001	R16	0.004	0.008	0.001
L18	0.006	0.010	0.001	R17	0.005	0.008	0.001
L19	0.006	0.011	0.001	R18	0.005	0.009	0.001

L20	0.007	0.012	0.001	R19	0.006	0.010	0.001
L21	0.007	0.012	0.001	R20	0.006	0.011	0.001
L22	0.008	0.013	0.001	R21	0.007	0.012	0.001
L23	0.008	0.014	0.001	R22	0.007	0.013	0.001
L24	0.008	0.014	0.001	R23	0.008	0.014	0.001
L25	0.008	0.014	0.001	R24	0.008	0.014	0.001
L26	0.008	0.014	0.001	R25	0.009	0.015	0.001
L27	0.008	0.013	0.001	R26	0.009	0.016	0.001
L28	0.007	0.013	0.001	R27	0.009	0.016	0.001
L29	0.007	0.012	0.001	R28	0.010	0.017	0.001
L30	0.006	0.011	0.001	R29	0.010	0.017	0.001
L31	0.005	0.009	0.001	R30	0.010	0.017	0.001
L32	0.004	0.008	0.001	R31	0.010	0.017	0.001
L33	0.004	0.007	0.001	R32	0.010	0.017	0.001
L34	0.003	0.005	0.001				

Table A.2. Ratio of average stress variation to concrete strength for traffic Pattern II

	Top slab	Bottom slab	Web		Top slab	Bottom slab	Web
M0	0.010	0.018	0.001	L35	0.002	0.003	0.001
L1	0.007	0.013	0.004	L36	0.001	0.001	0.001
L2	0.007	0.012	0.001	R1	0.010	0.017	0.001
L3	0.006	0.011	0.001	R2	0.009	0.016	0.001
L4	0.006	0.010	0.001	R3	0.009	0.015	0.001
L5	0.005	0.009	0.001	R4	0.008	0.014	0.001
L6	0.005	0.008	0.001	R5	0.008	0.013	0.001
L7	0.004	0.007	0.001	R6	0.007	0.012	0.001
L8	0.004	0.006	0.001	R7	0.007	0.011	0.001
L9	0.003	0.005	0.001	R8	0.006	0.011	0.001
L10	0.003	0.005	0.001	R9	0.006	0.010	0.001
L11	0.002	0.004	0.001	R10	0.005	0.009	0.001
L12	0.002	0.004	0.001	R11	0.005	0.008	0.001
L13	0.003	0.004	0.001	R12	0.004	0.007	0.001
L14	0.003	0.005	0.001	R13	0.003	0.006	0.001
L15	0.003	0.006	0.001	R14	0.003	0.005	0.001
L16	0.004	0.006	0.001	R15	0.003	0.005	0.001
L17	0.004	0.007	0.001	R16	0.003	0.006	0.001
L18	0.004	0.008	0.001	R17	0.004	0.007	0.001
L19	0.005	0.008	0.001	R18	0.004	0.007	0.001
L20	0.005	0.009	0.001	R19	0.005	0.008	0.001
L21	0.006	0.010	0.001	R20	0.005	0.009	0.001
L22	0.006	0.010	0.001	R21	0.005	0.009	0.001
L23	0.006	0.011	0.001	R22	0.006	0.010	0.001
L24	0.006	0.011	0.001	R23	0.006	0.011	0.001

L25	0.006	0.011	0.001	R24	0.007	0.011	0.001
L26	0.006	0.011	0.001	R25	0.007	0.012	0.001
L27	0.006	0.010	0.001	R26	0.007	0.012	0.001
L28	0.006	0.010	0.001	R27	0.007	0.013	0.001
L29	0.005	0.009	0.001	R28	0.007	0.013	0.001
L30	0.005	0.008	0.001	R29	0.008	0.013	0.001
L31	0.004	0.007	0.001	R30	0.008	0.013	0.001
L32	0.003	0.006	0.001	R31	0.008	0.013	0.001
L33	0.003	0.005	0.001	R32	0.008	0.013	0.001
L34	0.002	0.004	0.001				

Table A.3. Ratio of average stress variation to concrete strength for traffic Pattern III

	Top slab	Bottom slab	Web		Top slab	Bottom slab	Web
M0	0.012	0.021	0.001	L35	0.002	0.003	0.001
L1	0.009	0.015	0.004	L36	0.001	0.002	0.001
L2	0.008	0.014	0.001	R1	0.012	0.020	0.001
L3	0.007	0.013	0.001	R2	0.011	0.019	0.001
L4	0.007	0.012	0.001	R3	0.010	0.018	0.001
L5	0.006	0.010	0.001	R4	0.010	0.016	0.001
L6	0.005	0.009	0.001	R5	0.009	0.015	0.001
L7	0.005	0.008	0.001	R6	0.008	0.014	0.001
L8	0.004	0.007	0.001	R7	0.008	0.013	0.001
L9	0.004	0.006	0.001	R8	0.007	0.012	0.001
L10	0.003	0.005	0.001	R9	0.007	0.011	0.001
L11	0.003	0.004	0.001	R10	0.006	0.010	0.001
L12	0.003	0.004	0.001	R11	0.005	0.009	0.001
L13	0.003	0.005	0.001	R12	0.005	0.008	0.001
L14	0.003	0.006	0.001	R13	0.004	0.007	0.001
L15	0.004	0.007	0.001	R14	0.003	0.006	0.001
L16	0.004	0.008	0.001	R15	0.004	0.006	0.001
L17	0.005	0.008	0.001	R16	0.004	0.007	0.001
L18	0.005	0.009	0.001	R17	0.004	0.008	0.001
L19	0.006	0.010	0.001	R18	0.005	0.009	0.001
L20	0.006	0.011	0.001	R19	0.005	0.009	0.001
L21	0.007	0.011	0.001	R20	0.006	0.010	0.001
L22	0.007	0.012	0.001	R21	0.006	0.011	0.001
L23	0.007	0.012	0.001	R22	0.007	0.012	0.001
L24	0.007	0.013	0.001	R23	0.007	0.013	0.001

L25	0.007	0.013	0.001	R24	0.008	0.013	0.001
L26	0.007	0.013	0.001	R25	0.008	0.014	0.001
L27	0.007	0.012	0.001	R26	0.008	0.014	0.001
L28	0.007	0.012	0.001	R27	0.009	0.015	0.001
L29	0.006	0.011	0.001	R28	0.009	0.015	0.001
L30	0.006	0.010	0.001	R29	0.009	0.015	0.001
L31	0.005	0.008	0.001	R30	0.009	0.015	0.001
L32	0.004	0.007	0.001	R31	0.009	0.016	0.001
L33	0.004	0.006	0.001	R32	0.009	0.016	0.001
L34	0.003	0.005	0.001				

Table A.4. Ratio of average stress variation to concrete strength for traffic Pattern IV

	Top slab	Bottom slab	Web		Top slab	Bottom slab	Web
M0	0.012	0.021	0.001	L35	0.002	0.003	0.001
L1	0.009	0.015	0.004	L36	0.001	0.002	0.001
L2	0.008	0.014	0.001	R1	0.012	0.020	0.001
L3	0.008	0.013	0.001	R2	0.011	0.019	0.001
L4	0.007	0.012	0.001	R3	0.010	0.018	0.001
L5	0.006	0.011	0.001	R4	0.010	0.017	0.001
L6	0.006	0.010	0.001	R5	0.009	0.016	0.001
L7	0.005	0.008	0.001	R6	0.009	0.015	0.001
L8	0.004	0.007	0.001	R7	0.008	0.014	0.001
L9	0.004	0.006	0.001	R8	0.007	0.013	0.001
L10	0.003	0.005	0.001	R9	0.007	0.012	0.001
L11	0.003	0.004	0.001	R10	0.006	0.011	0.001
L12	0.003	0.004	0.001	R11	0.005	0.009	0.001
L13	0.003	0.005	0.001	R12	0.005	0.008	0.001
L14	0.004	0.006	0.001	R13	0.004	0.007	0.001
L15	0.004	0.007	0.001	R14	0.003	0.006	0.001
L16	0.004	0.008	0.001	R15	0.004	0.006	0.001
L17	0.005	0.008	0.001	R16	0.004	0.007	0.001
L18	0.005	0.009	0.001	R17	0.004	0.008	0.001
L19	0.006	0.010	0.001	R18	0.005	0.009	0.001
L20	0.006	0.011	0.001	R19	0.006	0.010	0.001
L21	0.007	0.012	0.001	R20	0.006	0.010	0.001
L22	0.007	0.012	0.001	R21	0.007	0.011	0.001
L23	0.007	0.013	0.001	R22	0.007	0.012	0.001
L24	0.007	0.013	0.001	R23	0.007	0.013	0.001

L25	0.007	0.013	0.001	R24	0.008	0.013	0.001
L26	0.007	0.013	0.001	R25	0.008	0.014	0.001
L27	0.007	0.012	0.001	R26	0.008	0.015	0.001
L28	0.007	0.012	0.001	R27	0.009	0.015	0.001
L29	0.006	0.011	0.001	R28	0.009	0.015	0.001
L30	0.006	0.010	0.001	R29	0.009	0.016	0.001
L31	0.005	0.009	0.001	R30	0.009	0.016	0.001
L32	0.004	0.007	0.001	R31	0.009	0.016	0.001
L33	0.004	0.006	0.001	R32	0.009	0.016	0.001
L34	0.003	0.005	0.001				

Table A.5. Ratio of average stress variation to concrete strength for traffic Pattern V

	Top slab	Bottom slab	Web		Top slab	Bottom slab	Web
M0	0.014	0.024	0.001	L35	0.002	0.004	0.001
L1	0.010	0.017	0.005	L36	0.001	0.002	0.001
L2	0.009	0.016	0.001	R1	0.013	0.023	0.001
L3	0.009	0.015	0.001	R2	0.013	0.022	0.001
L4	0.008	0.013	0.001	R3	0.012	0.020	0.001
L5	0.007	0.012	0.001	R4	0.011	0.019	0.001
L6	0.006	0.011	0.001	R5	0.010	0.018	0.001
L7	0.006	0.010	0.001	R6	0.010	0.017	0.001
L8	0.005	0.008	0.001	R7	0.009	0.015	0.001
L9	0.004	0.007	0.001	R8	0.008	0.014	0.001
L10	0.004	0.006	0.001	R9	0.008	0.013	0.001
L11	0.003	0.005	0.001	R10	0.007	0.012	0.001
L12	0.003	0.005	0.001	R11	0.006	0.011	0.001
L13	0.003	0.006	0.001	R12	0.005	0.009	0.001
L14	0.004	0.007	0.001	R13	0.005	0.008	0.001
L15	0.005	0.008	0.001	R14	0.004	0.007	0.001
L16	0.005	0.009	0.001	R15	0.004	0.007	0.001
L17	0.006	0.010	0.001	R16	0.005	0.008	0.001
L18	0.006	0.011	0.001	R17	0.005	0.009	0.001
L19	0.007	0.012	0.001	R18	0.006	0.010	0.001
L20	0.007	0.012	0.001	R19	0.006	0.011	0.001
L21	0.008	0.013	0.001	R20	0.007	0.012	0.001
L22	0.008	0.014	0.001	R21	0.007	0.013	0.001
L23	0.008	0.014	0.001	R22	0.008	0.014	0.001
L24	0.008	0.015	0.001	R23	0.008	0.015	0.001

L25	0.008	0.015	0.001	R24	0.009	0.015	0.001
L26	0.008	0.014	0.001	R25	0.009	0.016	0.001
L27	0.008	0.014	0.001	R26	0.010	0.017	0.001
L28	0.008	0.013	0.001	R27	0.010	0.017	0.001
L29	0.007	0.012	0.001	R28	0.010	0.017	0.001
L30	0.007	0.011	0.001	R29	0.010	0.018	0.001
L31	0.006	0.010	0.001	R30	0.010	0.018	0.001
L32	0.005	0.008	0.001	R31	0.010	0.018	0.001
L33	0.004	0.007	0.001	R32	0.010	0.018	0.001
L34	0.003	0.006	0.001				

Table A.6. Ratio of average stress variation to concrete strength for traffic Pattern VI

	Top slab	Bottom slab	Web		Top slab	Bottom slab	Web
M0	0.018	0.031	0.002	L35	0.003	0.005	0.002
L1	0.013	0.022	0.006	L36	0.001	0.003	0.002
L2	0.012	0.020	0.002	R1	0.017	0.029	0.002
L3	0.011	0.019	0.002	R2	0.016	0.027	0.002
L4	0.010	0.017	0.002	R3	0.015	0.026	0.002
L5	0.009	0.015	0.002	R4	0.014	0.024	0.002
L6	0.008	0.014	0.002	R5	0.013	0.023	0.002
L7	0.007	0.012	0.002	R6	0.012	0.021	0.002
L8	0.006	0.011	0.002	R7	0.011	0.020	0.002
L9	0.005	0.009	0.002	R8	0.011	0.018	0.002
L10	0.005	0.008	0.002	R9	0.010	0.017	0.002
L11	0.004	0.007	0.002	R10	0.009	0.015	0.002
L12	0.004	0.006	0.002	R11	0.008	0.014	0.002
L13	0.004	0.008	0.002	R12	0.007	0.012	0.002
L14	0.005	0.009	0.002	R13	0.006	0.010	0.002
L15	0.006	0.010	0.002	R14	0.005	0.009	0.002
L16	0.006	0.011	0.002	R15	0.005	0.009	0.002
L17	0.007	0.012	0.002	R16	0.006	0.010	0.002
L18	0.008	0.013	0.001	R17	0.006	0.011	0.002
L19	0.008	0.015	0.001	R18	0.007	0.013	0.002
L20	0.009	0.016	0.001	R19	0.008	0.014	0.002
L21	0.010	0.017	0.001	R20	0.009	0.015	0.001
L22	0.010	0.018	0.001	R21	0.009	0.016	0.001
L23	0.011	0.018	0.001	R22	0.010	0.017	0.001
L24	0.011	0.019	0.001	R23	0.011	0.019	0.001

L25	0.011	0.019	0.001	R24	0.011	0.019	0.001
L26	0.011	0.018	0.001	R25	0.012	0.020	0.001
L27	0.010	0.018	0.001	R26	0.012	0.021	0.001
L28	0.010	0.017	0.001	R27	0.013	0.022	0.001
L29	0.009	0.016	0.001	R28	0.013	0.022	0.001
L30	0.008	0.014	0.001	R29	0.013	0.023	0.001
L31	0.007	0.012	0.001	R30	0.013	0.023	0.001
L32	0.006	0.010	0.001	R31	0.013	0.023	0.001
L33	0.005	0.009	0.002	R32	0.013	0.023	0.001
L34	0.004	0.007	0.002				

BIBLIOGRAPHY

[1]   Strauss A, Wendner R, Bergmeister K, and Costa C. Numerically and Experimentally Based Reliability Assessment of a Concrete Bridge Subjected to Chloride Induced Deterioration. *Journal of Infrastructure Systems*, 19(2): 166-175, 2013.

[2]   Wendner R, Strauss A, Guggenberger T, Bergmeister K, and Teply B. Approach for the Assessment of Concrete Structures Subjected to Chloride Induced Deterioration. *BETON-STAHLBETONBAU*, 105(12): 778-786, 2010.

[3]   Bažant Z P, Hubler M H, and Yu Q. Pervasiveness of Excessive Segmental Bridge Deflections: Wake-Up Call for Creep. *ACI Structural Journal*, 108(6): 766-774, 2011.

[4]   Bažant Z P, Yu Q, Li G H, Klein G J, and Krístek V. Excessive Deflections of Record-Span Prestressed Box Girder-Lessons learned from the collapse of the Koror-Babeldaob Bridge in Palau. *Concrete International*, 32(6): 44-52, 2010.

[5]   Bažant Z P, Hubler M H, and Yu, Q. Excessive creep deflections: An awakening. *Concrete International*, 33(8): 44-46, 2011.

[6]   Bažant Z P, Yu Q, and Li G H. Excessive long-time deflections of prestressed box girders. I: Record-span Bridge in Palau and other paradigms. *Journal of Structural Engineering*, 138(6): 676-686, 2012.

[7]   Bažant Z K P, Yu Q, and Li G H. Excessive long-time deflections of prestressed box girders. II: Numerical analysis and lessons learned. *Journal of Structural Engineering*, 138(6): 687-696, 2012.

[8]   Burgoyne C J and Scantlebury R. Why did Palau bridge collapse? *The Structural Engineer*, 84: 30-37, 2006.

[9]   Maekawa K, Chijiwa N, and Ishida T. Long-term deformational simulation of PC bridges based on the thermo-hygro model of micro-pores in cementitious composites. *Cement and Concrete Research*, 41(12): 1310-1319, 2011.

[10]   Chen W F and Lian D. Bridge Engineering Handbook: Construction and Maintenance. *CRC press*, 2014.

[11]   Hubler M H, Wendner R, and Bažant Z P. Statistical justification of model B4 for drying and autogenous shrinkage of concrete and comparisons to other models. *Materials and Structures*, 48(4): 797-814, 2015.

[12]   Wendner R, Hubler M H, and Bažant Z P. Statistical justification of Model B4 for multi-decade concrete creep and comparisons to other models using laboratory and bridge databases. *RILEM – Materials and Structures*, 2014.

[13]   Yu Q, Bažant Z P, and Wendner R. Improved Algorithm for Efficient and Realistic Creep Analysis of Large Creep-Sensitive Concrete Structures. *ACI Structural Journal*, 109(5): 665-675, 2012.

[14]   Bažant Z P and Baweja S. Creep and shrinkage prediction model for analysis and design of concrete structures: Model B3. *ACI SPECIAL PUBLICATIONS*, 194: 1-84, 2000.

[15]   Bažant Z P and Baweja S. Justification and refinements of model B3 for concrete creep and shrinkage I. statistics and sensitivity. *Materials and Structures*, 28(7): 415-430, 1995.

[16]   Bažant Z P and Prasannan S. Solidification theory for concrete creep II: verification and application. *Journal of Engineering Mechanics*, 115(8): 1704-1725, 1989.

[17]   Bažant Z P and Prasannan S. Solidification theory for concrete creep I: formulation. *Journal of Engineering Mechanics*, 115(8): 1691-1703, 1989.

[18]   Bažant Z P, Wendner R, and Hubler M H. Model B4 for Concrete Creep including Multi-Decade Prediction: Description and Application. *RILEM – Materials and Structures*, 2014.

[19]   Fédération Internationale du Béton. International Federation for Structural Concrete Special Activity Group New Model Code. *Lausanne: International Federation for Structural Concrete*, 2012.

[20]   Bažant Z P and Yu Q. Relaxation of Prestressing Steel at Varying Strain and Temperature: Viscoplastic Constitutive Relation. *Journal of Engineering Mechanics*, 139(7): 814-823, 2012.

[21]   Tong T, Fan Z, Liu Q, Wang S, Tan S, and Yu Q. Investigation of the effects of graphene and graphene oxide on the micro-and macro-properties of cementitious materials. *Construction and Building Materials*, 106: 102-114, 2016.

[22]   Pellenq R J M, Kushima A, Shahsavari R, Van Vliet K J, Buehler M J, Yip S, and Ulm F J. A realistic molecular model of cement hydrates. P*roceedings of the National Academy of Sciences*, 106(38): 16102-16107, 2009.

[23]   Tu Z and Lu Y. Mesoscale modelling of concrete for static and dynamic response analysis-Part I: model development and implementation. *Structural Engineering and Mechanics*, 37(2): 197-213, 2011.

[24] Yang Z J, Su X T, Chen J F, and Liu G H. Monte Carlo simulation of complex cohesive fracture in random heterogeneous quasi-brittle materials. *International Journal of Solids and Structures*, 46(17): 3222-3234, 2009.

[25] Yang Z and Xu X F. A heterogeneous cohesive model for quasi-brittle materials considering spatially varying random fracture properties. *Computer methods in applied mechanics and engineering*, 197(45): 4027-4039, 2008.

[26] Wang X F, Yang Z J, Yates J R, Jivkov A P, and Zhang C. Monte Carlo simulations of mesoscale fracture modelling of concrete with random aggregates and pores. *Construction and Building Materials*, 75: 35-45, 2015.

[27] ACI Committee. Building Code Requirements for Structural Concrete (ACI 318-08) and Commentary. *Farmington Hills: American Concrete Institute*, 2008.

[28] CEB-FIP M C. Design of concrete structures: CEB-FIP-Model-Code 1990. *London: British Standard Institution*, 1993.

[29] Jirásek M and Bažant Z P. Inelastic analysis of structures. *NewYork: John Wiley & Sons*, 2002.

[30] Bažant Z P and Xi Y. Continuous retardation spectrum for solidification theory of concrete creep. *Journal of Engineering Mechanics*, 121(2): 281-288, 1995.

[31] Widder D V. An introduction to transform theory. *NewYork: Academic Press*, 1971.

[32] Bažant Z P, Hubler M H, and Jirásek M. Improved estimation of long-term relaxation function from compliance function of aging concrete. *Journal of Engineering Mechanics*, 139(2): 146–152, 2012.

[33] Brooks J J. 30-year creep and shrinkage of concrete. *Magazine of concrete research*, 57(9): 545-556, 2005.

[34] Bažant Z P and Li G H. Unbiased statistical comparison of creep and shrinkage prediction models. *ACI Materials Journal*, 106 (6): 610–621, 2008.

[35] Bažant Z P and Li G H. Comprehensive database on concrete creep and shrinkage. *ACI Materials Journal*, 106 (6): 635–638, 2008.

[36] Iman R C and Conover W J. Small Sample Sensitivity Analysis Techniques for Computer Models with an Application to Risk Assessment. *Communications in Statistics Theory and Methods*, 9(17): 1749-1842, 1980.

[37] Strauss A, Hoffmann S, Wendner R, and Bergmeister K. Structural assessment and reliability analysis for existing engineering structures, applications for real structures. *Structure and Infrastructure Engineering*, 5(4): 277-286, 2009.

[38]   Brooks J J. Accuracy of estimating long-term strains in concrete. *Magazine of Concrete Research*, 36(128): 131-145, 1984.

[39]   Mamlouk M S and Zaniewski J P. Materials for civil and construction engineers. *Boston: Addison-Wesley*, 1999.

[40]   Wender R, Tong T, Strauss A, and Yu Q. A case study on correlations of axial shortening and deflection with concrete creep asymptotes in segmentally-erected prestressed box girders. *Structure and Infrastructure Engineering*, 11(12): 1672-1687, 2015.

[41]   Pearson K. Notes on regression and inheritance in the case of two parents. *Proceedings of the Royal Society of London*, 58: 240–242, 1895.

[42]   Stigler S M. Francis Galton's Account of the Invention of Correlation. *Statistical Science*, 4(2): 73–79, 1989.

[43]   Kirkpatrick S and Vecchi M P. Optimization by simulated annealing. *Science*, 220(4598): 671-680, 1983.

[44]   Vořechovský M and Novák D. Correlation control in small sample Monte Carlo type simulations I: A Simulated Annealing approach. *Probabilistic Engineering Mechanics*, 24(3): 452-462, 2009.

[45]   Novák D, Teplý B, and Keršner Z. The role of Latin Hypercube Sampling method in reliability engineering. *In Proc. of ICOSSAR, Kyoto, Japan*, 1998.

[46]   Monahan J F. Numerical methods of statistics. Cambridge: *Cambridge University Press*, 2011.

[47]   Bažant Z P and Hubler M H. Theory of cyclic creep of concrete based on Paris law for fatigue growth of subcritical microcracks. *Journal of Mechanics and Physics of Solids*, 63: 187-200, 2014.

[48]   Pandolfi A and Taliercio A. Bounding surface models applied to fatigue of plain concrete. *Journal of Engineering Mechanics*, 124(5): 556–564, 1998.

[49]   Brooks J J and Forsyth P. Influence of frequency of cyclic load on creep of concrete. *Magazine of Concrete Research*, 38 (136): 139–150, 1986.

[50]   Mekawa K and El-Kashif KF. Cyclic cumulative damaging of reinforced concrete in post-peak regions. *Journal of Advanced Concrete Technology*, 2(2): 257–271, 2004.

[51]   Gao L and Hsu C T T. Fatigue of concrete under compression cyclic loading. ACI Materials Journal, 95(5): 575–579, 1998.

[52]   Neville A M and Hirst G A. Mechanism of cyclic creep of concrete. *In: Douglas McHenry International Symposium on Concrete and Concrete Structures*, 1978.

[53]   Garrett G G, Jennings H M and Tait R B. The fatigue hardening behavior of cement-based materials. *Journal of Materials Science*, 14: 296–306, 1979.

[54]   Gaede K. Versuche über die Festigkeit und die Verformung von Beton bei Druck-Schwellbeanspruchung: und über den Einfluß der Größe der Proben auf die Würfeldruckfestigkeit von Beton. Ernst., 1962.

[55]   Bažant Z P. On causes of excessive long-time deflections of prestressed concrete bridges. Creep under repeated live load. *In: Czech Inženýrské*, 1968.

[56]   Bažant Z P, Kim J K, and Panula L. Improved prediction model for time-dependent deformations of concrete: Part 5–Cyclic load and cyclic humidity. *Materials and Structures (RILEM, Paris)*, 25 (147): 163–169, 1992.

[57]   Bažant Z P and Panula L. Practical prediction of time-dependent deformations of concrete. Matériaux et Construction, 12(3): 169-174, 1979.

[58]   Hellesland J and Green R. Sustained and cyclic loading of concrete columns. *Journal of the Structure Division*, 1971.

[59]   Bažant Z P and Le J L. Nano-mechanics based modelling of lifetime distribution of quasi-brittle structures. *Engineering Failure Analysis*, 16: 2521–2529, 2009.

[60]   Le J L and Bazant Z P. Unified nano-mechanics based probabilistic theory of quasibrittle and brittle structures: II. fatigue crack growth, lifetime and scaling. *Journal of Mechanics and Physics of Solids*, 59: 1322-1337, 2011.

[61]   Suresh S. Fatigue of materials. *Cambridge university press*, 1998.

[62]   Cicekli U, Voyiadjis G Z, and Al-Rub R K A. A plasticity and anisotropic damage model for plain concrete. *International Journal of plasticity*, 23(10): 1874-1900, 2007.

[63]   Al-Rub R K A and Voyiadjis G Z. On the coupling of anisotropic damage and plasticity models for ductile materials. *Journal of Mechanics and Physics of Solids*, 40(11): 2611-2643, 2003.

[64]   Voyiadjis G Z, Al-Rub R K A, and Palazotto A N. Thermodynamic framework for coupling of non-local viscoplasticity and non-local anisotropic viscodamage for dynamic localization problems using gradient theory. *International Journal of Plasticity*, 20(6): 981-1038, 2004.

[65]   Voyiadjis G Z and Kattan P I. Advances in Damage Mechanics: Metals and Metal Matrix Composites, with an Introduction to Fabric Tensors (Second Edition), *Elsevier*, 2006.

[66]   Lubliner J, Oliver J, Oller S, and Onate E. A plastic-damage model for concrete. *International Journal of Solids and Structures*, 25(3): 299-326, 1989.

[67]   Tao X and Phillips D V. A simplified isotropic damage model for concrete under bi-axial stress states. *Cement and Concrete Composites*, 27(6): 716-726, 2005.

[68]   La Borderie C, Mazars J, and Pijaudier-Cabot G. Response of plain and reinforced concrete structures under cyclic loadings. *ACI Special Publication*, 1992.

[69]   Bažant Z P, Caner F C, Cedolin L, Cusatis G, and Di LG. Fracturing material models based on micromechanical concepts: recent advances. *Proceedings of the Fracture Mechanics of Concrete and Concrete Structures–FraMCoS-5*, 83-89, 2004.

[70]   Bažant Z P, Cusatis G, and Cedolin L. Temperature effect on concrete creep modeled by microprestress-solidification theory. *Journal of Engineering Mechanics*, 130(6): 691-699, 2004.

[71]   Di Luzio G and Cedolin L. Numerical model for time-dependent fracturing of concrete structures and its application. *In New Trends in Fracture Mechanics of Concrete, Proceedings of International Conference on Fracture Mechanics of Concrete and Concrete Structures*, 175-180, 2007.

[72]   Simo J C. Numerical analysis and simulation of plasticity. *Handbook of numerical analysis*, 6: 183-499, 1998.

[73]   Guangzhou Humen Bridge Co., Ltd. Special investigation of Humen Bridge Auxiliary Channel Bridge. 2011. (in Chinese)

[74]   Zhou F P. Time-dependent crack growth and fracture in concrete. PhD thesis, *Lund University, Sweden*, 1992.

[75]   Grassl P and Jirasek M. Nonlocal damage-plasticity model for failure of plain concrete. *International Journal of Solids and Structures*, 43: 7166-7196, 2006.

[76]   Pijaudier-Cabot G and Bažant Z P. Nonlocal damage theory. *Journal of Engineering Mechanics*, 113(10): 1512-1533, 1987.

[77]   Bažant Z P and Pijaudier-Cabot G. Nonlocal continuum damage, localization instability and convergence. *Journal of Applied Mechanics*, 55(2): 287-293, 1988.

[78]   Bažant Z P and Oh B H. Crack band theory for fracture of concrete. *Matériaux et construction*, 16(3): 155-177, 1983.

[79]   Červenka J, Bažant Z P, and Wierer M. Equivalent localization element for crack band approach to mesh-sensitivity in microplane model. *International Journal for Numerical Methods in Engineering*, 62(5): 700-726, 2005.

[80]   American Society for Testing and Materials (ASTM). Standard specification for steel strand, uncoated seven-wired for prestressed concrete. *ASTM Designation No. A416-94, Philadelphia*, 1997.

[81]   Whaley C P and Neville A M. Non-elastic deformation of concrete under cyclic compression. *Magazine of Concrete Research*, 25 (84): 145–154, 1973.

[82]   Kern E and Mehmel A. Elastische und plastische Stauchungen von Beton infolge Druckschwell- und Standbelastung. *Vertrieb durch Verlag von W. Ernst.*, 1962.

[83]   Mostafavi M, Baimpas N, Tarleton E, Atwood R C, McDonald S A, Korsunsky A M, and Marrow T J. Three-dimensional crack observation, quantification and simulation in a quasi-brittle material. *Acta Materialia*, 61(16): 6276-6289, 2013.

[84]   You Z, Adhikari S, and Kutay M E. Dynamic modulus simulation of the asphalt concrete using the X-ray computed tomography images. *Materials and Structures*, 42(5): 617-630, 2009.

[85]   Jivkov A P, Engelberg D L, Stein R, and Petkovski M. Pore space and brittle damage evolution in concrete. *Engineering Fracture Mechanics*, 110: 378-395, 2013.

[86]   Leite J P B, Slowik V, and Mihashi H. Computer simulation of fracture processes of concrete using mesolevel models of lattice structures. *Cement and concrete research*, 34(6): 1025-1033, 2004.

[87]   Wang Z M, Kwan A K H, and Chan H C. Mesoscopic study of concrete I: generation of random aggregate structure and finite element mesh. *Computers & Structures*, 70(5): 533-544, 1999.

[88]   Hirsch T J. Modulus of elasticity of concrete affected by elastic moduli of cement paste matrix and aggregate. *In Journal Proceedings*, 59(3): 427-452, 1962.

[89]   Lagerblad B and Trägårdh J. Conceptual model for concrete long time degradation in a deep nuclear waste repository. *Swedish Cement and Concrete Research Institute*, 1996.

[90]   Hordijk D A. Local approach to fatigue of concrete. *Delft University of Technology*, 1991.

[91]   Schlangen E and Van Mier J G M. Simple lattice model for numerical simulation of fracture of concrete materials and structures. *Materials and Structures*, 25(9): 534-542, 1992.

[92]   Idiart A, Bisschop J, Caballero A, and Lura P. A numerical and experimental study of aggregate-induced shrinkage cracking in cementitious composites. *Cement and Concrete Research*, 42(2): 272-281, 2012.

[93]   Barenblatt G I. The formation of equilibrium cracks during brittle fracture. General ideas and hypotheses. Axially-symmetric cracks. *Journal of Applied Mathematics and Mechanics*, 23(3): 622-636, 1959.

[94]   Dugdale D S. Yielding of steel sheets containing slits. *Journal of the Mechanics and Physics of Solids*, 8(2): 100-104, 1960.

[95]   Havlásek P and Jirásek M. Multiscale modeling of drying shrinkage and creep of concrete. *Cement and Concrete Research*, 85: 55-74, 2016.

[96]   Tchalla A, Belouettar S, Makradi A, and Zahrouni H. An ABAQUS toolbox for multiscale finite element computation. *Composites Part B: Engineering*, 52: 323-333, 2013.

[97]   Mori T and Tanaka K. Average stress in matrix and average elastic energy of materials with misfitting inclusions. *Acta Metallurgica*, 21(5): 571-574, 1973.

[98]   Eshelby J D. The determinati on of the elastic field of an ellipsoidal inclusion, and related problems. *Proc. R. Soc. Lond. A*, 241: 376-396, 1957.

[99]   Pan C and Yu Q. Disturbed elastic fields in a circular 2D finite domain containing a circular inhomogeneity and a finite interfacial zone. *Acta Mechanica*, 226(5): 1457-1470, 2015.

[100] Yu Q, Pan C, and Tong T. A multi-scale material model for predicting the multi-decade behavior of concrete structures. *In Structures Congress 2013: Bridging Your Passion with Your Profession (ASCE)*, 1891-1902, 2013.